

UNIVERSITY OF TWENTE.

Faculty of Engineering Technology
Engineering Fluid Dynamics

Determination of the source term disturbing bounded flow performing practical Large Eddy Simulations

Master Thesis

I.G.W. Krabben

Graduation Committee:

dr. ir. N.P. Kruyt
dr. ir. A.K. Pozarlik
dr. ir. N.P. Waterson
dr. ir. E.T.A. van der Weide

Enschede, March 2020

Abstract

Single-hole orifices are often applied noise sources in cooling water pipes. These components disturb internal fluid locally which subsequently results in pipe wall vibrations elsewhere in the system. In the extreme ultraviolet machines ASML produces, these vibrations lead to end-product inaccuracies. To model the expected flow-induced vibrations with the tool PlaNet3D, an accurate description of the source term is required. This study determines this hard-to-measure source term using practical Large Eddy Simulations (LES).

Previous studies have shown that acoustic noise is generated via the action of vortex stretching relative to the body, wall separation and vortex shedding. For low Mach number flows, these noise generating mechanisms are represented as an in time fluctuating force acting from the orifice to the fluid. Incompressible LES are performed using a recycling plane method at the inlet. This proposed method is easy to implement and is applicable to different geometries. Results of LES on computational grids with different grid sizes are compared with experiments and Direct Numerical Simulations (DNS). Refining the grid till sizes equal to the Taylor microscales, a good match with DNS pipe flow profiles is obtained for the first and second order flow statistics. Additionally, the power spectral density (PSD) of wall pressure fluctuations in a straight pipe agrees with experimental data.

After the straight pipe flow is properly resolved, an orifice is added to the straight pipes. The simulated pressure drops generated by the orifice are according to values found in literature. Besides, the pressure drop fluctuations are found to match with force fluctuations divided by the pipe area indicating a conservation of momentum. A comparison of a DNS one-dimensional energy spectrum with LES on the finest grid shows a good match in the inertial subrange. This indicates properly resolved turbulent scales. Additionally, the resolution in the jet-wake region is found acceptable based on the turbulent viscosity ratio. The PSD slope of wall pressure fluctuation in the jet-wake region matches with theoretical power laws and experimental data. However, the pressure fluctuations in that region are overpredicted by LES. The PSD of wall pressure fluctuations in the orifice and upstream of the orifice show a similar shape compared to the simulated force spectra acting on the fluid. The spectra consist of distinct peaks at frequencies which are different for each used computational grid. A peak might be due to vortex shedding, which is found to occur at a Strouhal number of roughly 0.4. But, possibly this peak is nonphysical arising from numerical inaccuracies and thus requires further investigation. Nonetheless, the slope of the force spectrum obtained with LES on the finest considered grid is the same as found in literature and is therefore found accurate. The simulations are performed within a week so a practical LES setup is proposed to accurately determine the source term. In following studies it is recommended to simulate different geometries and flow conditions.

Contents

Contents	v
List of Figures	ix
List of Tables	xiii
1 Introduction	1
1.1 Research questions	3
1.2 Research approach	4
2 Review of Literature	5
2.1 Governing equations	5
2.2 Pipe excitation prediction tools	5
2.3 Turbulence	6
2.4 Orifice flow	8
2.5 Flow noise	9
2.6 Noise generation	10
2.6.1 Quadrupole noise	10
2.6.2 Dipole noise	11
2.6.3 Dominant source term	12
2.7 Exact solution to Curle’s analogy	13
2.8 Experimental research	13
2.9 Computational Fluid Dynamics studies	14
2.10 Conclusions	14
3 Review of Experimental Data	17
3.1 Experimental setup	17
3.2 Post processing	18
3.3 Straight pipe measurement data	18
3.4 Hydrodynamic pressure fluctuation measurement data	19
3.5 Acoustic pressure fluctuation measurement data	19
3.6 Turbulent pipe LDV measurement data	21
4 Numerical Approach	23
4.1 Large Eddy Simulation	23
4.1.1 SGS model	24
4.1.2 Implicit LES	25
4.2 Solver	25
4.2.1 Segregated flow solver	25
4.2.2 Convection discretization scheme	25
4.2.3 Temporal discretization	26
4.2.4 Accuracy LES	27
4.3 Computational domain	28
4.4 Mesh	28
4.4.1 Near-wall treatment	29

4.4.2	Meshing the pipe region	30
4.4.3	Meshing the orifice region	31
4.5	Setup conditions	32
4.5.1	Time stepping	32
4.5.2	Boundary conditions	33
4.5.3	Initialization	35
4.5.4	Data extraction	35
4.6	Analysis of scalability	36
4.7	Residuals	36
4.8	Summary of simulation details	37
5	Results of Straight Pipe	39
5.1	Applied boundary conditions	39
5.2	Computational grid refinement	41
5.3	Wall shear stress	43
5.4	Conclusions	44
6	Results of Orifice	47
6.1	Velocity fluctuations	47
6.2	Pressure drop	49
6.3	Pressure fluctuations	49
6.4	Source term	54
6.5	Orifice resolution	56
6.6	Conclusions	59
7	Conclusions & Recommendations	61
7.1	Conclusions	61
7.2	Recommendations	62
	References	63
	Appendix	67
A	Coupling with Theory	67
A.1	Discretization	69
B	Simulation Setup Steps STAR-CCM+	71
B.1	Geometry/Continuum/Region	71
B.2	Initialization/Boundary conditions	72
B.3	Data mapping	72
B.4	Solver	73
B.5	Derived parts/Report/Monitor	73
B.6	Field functions	74
B.7	Other	74
B.7.1	How to determine average cell size in bulk region	74
C	Reynolds-Averaged Navier-Stokes	75
C.1	Precursor steady-state simulation	75
C.2	Closure problem	75
C.3	Turbulence models	76
C.3.1	Exploratory meshes	76
C.3.2	Boundary conditions	76
C.4	Precursor RANS results	77
D	Computational Grids for LES	79
E	Results of Straight Pipe	83

List of Figures

1.1	EUV deployed to write structures on a wafer. The source emits light on a reticle containing a blue print. This image is then reflected via mirrors to the wafer where the structure is printed on a silicon plate.	1
1.2	Water cooling system containing a sensitive and nonsensitive region. The brown parts are disturbing components generating a flow disturbance indicated by a green arrow. Resulting excitations of the piping system are indicated by a red arrow.	2
1.3	The outline of the thesis.	4
2.1	Lumped mass-spring system used in PlaNet3D to represent acoustic pressure waves in fluid flow.	6
2.2	a: Characteristic eddy sizes in turbulent flow (Pope (2001)). b: Energy cascade.	7
2.3	Pipe flow through a single-hole orifice, generating a pressure drop.	8
2.4	Mechanisms dissipating mechanical energy responsible for the permanent total pressure loss.	9
2.5	The sound fields produced by the different source terms.	11
2.6	Eddy radiating sound in a turbulent region as a quadrupole (Howe (2003)).	12
3.1	a: PSD of hydrodynamic wall pressure fluctuations in a straight pipe for different Reynolds number. b: Comparison of hydrodynamic wall pressure fluctuations measured at ASML normalized with the hydrodynamic pressure q . The orifice is located at $z/D = 0$	19
3.2	PSD of wall pressure fluctuations far up- and downstream of the orifice. a: Supplemented with a PSD of subtracted time signals. b: Supplemented with a PSD of added time signals.	20
3.3	a: PSD of the force resulting from the exact solution to Curle's analogy. b: Root mean square of the force required to generate subtraction graphs in Figure 3.2a as a function of the distance between source and observer.	20
3.4	Comparison of the flow statistics of DNS data by El Khoury et al. (2013) ($Re = 11700$) and experimental data by Den Toonder and Nieuwstadt (1997) ($Re = 10000$). The experimental measurement error is included. a: The axial velocity normalized with the friction velocity. b: The turbulent stress components in fluid normalized with the friction velocity squared.	21
4.1	FVM convection discretization a: Stencil for interpolating cell face values from known cell-center values.	26
4.2	Turbulent statistic Q as a function of the filter width Δ (Pope (2004)).	27
4.3	Schematic of computational domain used in LES with dimensions.	28
4.4	Visualization of good computational cells STAR-CCM+ (2018). a: Skewness angle. b: Volume change. c: Face validity.	29
4.5	Modelling of the wall layer (STAR-CCM+, 2018, p. 3733).	30
4.6	Mesh grid around orifice using different near wall layer meshing methods. a: Prism layer mesher. b: Advancing layer mesher.	32
4.7	a: Boundary conditions using the synthetic eddy method. b: Boundary conditions applying periodic boundary conditions.	33
4.8	a: Boundary conditions using the recycling plane method. b: Cross correlation of the axial velocity in the periodic pipe.	34
4.9	a: The mean of the axial velocity as a function of time. b: The TKE as a function of time. c: The mean pressure as a function of time.	35

4.10	Scalability analysis on a computational grid consisting of 262k cells. a: The speed up as a function of the number of processors. b: The efficiency as a function of the number of processors.	36
4.11	a: Residuals of LES on computational grid 1. b: Residuals of LES on computational grid 8.	37
5.1	Flow statistic profiles for the different boundary conditions applied as a function of radial distance to the wall at $z/D = -2$ compared with DNS. a: The axial velocity normalized with the bulk velocity. b: The TKE normalized with the bulk velocity squared.	40
5.2	The development of quantities as a function of upstream distance to the inlet. a: The centerline velocity in axial direction normalized with the bulk velocity. b: The bulk TKE normalized with bulk velocity squared.	40
5.3	a: Wall pressure fluctuations normalized with the hydrodynamic pressure. b: The PSD of wall pressure fluctuations in a straight pipe.	41
5.4	Velocity profiles in the axial direction at $z/D = -2$ for LES on different grids. a: Normalized with the bulk velocity. b: Normalized with the friction velocity.	42
5.5	TKE profiles at $z/D = -2$ for LES on different grids, see Table 4.3. Results are compared with DNS of El Khoury et al. (2013). a: Normalized with the bulk velocity squared. b: Normalized with the friction velocity squared (see legend of others).	42
5.6	Turbulent shear stress profiles at $z/D = -2$ for LES on different grids. a: Normalized with the friction velocity squared. b: Normalized with the friction velocity squared on logarithmic x-axis (see legend of others).	43
5.7	a: The wall shear stress as function of different computational grid properties. b: The wall shear stress development as a function of upstream distance to the inlet.	44
6.1	The normalized one-dimensional velocity spectra in flow direction obtained with LES on different grids compared with DNS (Lee and Moser (2015)). Data is probed at the centerline at different axial locations; a: $z/D = -5$, b: , c: , and d:	48
6.2	Mean wall pressure as a function of normalized distance to the orifice for LES on different computational grids. A schematic of distribution of wall point probes is included.	49
6.3	Normalized wall pressure fluctuations obtained with LES on different computational grids as a function of normalized distance to the orifice. A frequency range from 10 Hz to 800 Hz is considered. A schematic of the distribution of wall point probes is included.	50
6.4	The wall pressure spectra obtained with LES on all computational grids. The slope of the experimental data obtained by Kottapalli is included. Data is probed at different axial locations.	51
6.5	Wall pressure spectra obtained with LES at locations $z/D = 1$ till $z/D = 6$. Power laws $\Phi_s(f)$ and $\Phi_t(f)$ are included.	52
6.6	Wall pressure spectra obtained with LES on all computational grids.	53
6.7	Snapshots of the velocity magnitude field at different time instants obtained with LES on the finest computational grid.	54
6.8	a: Force spectra on the different geometry surfaces simulated on the coarsest and finest grid using LES. b: Net force spectra on the orifice plate for different LES.	55
6.9	Control volume of the fluid in the domain.	56
6.10	Results of LES performed on grid 8. a: The mean of the turbulent viscosity ratio, TVR . b: The TKE by the sugrid scale model to the resolved TKE, M_{TKE} . 6.10c: The mean of the turbulent length scale, $\bar{\ell}_0$. d: The instantaneous turbulent time scale, t_ℓ	57
6.11	The field visualization of the mean velocity and the cross stream and axial fluid stresses normalized with respectively the friction velocity and friction velocity squared, and the static pressure gradient. a: LES on the finest grid ($Re = 10000$). b: PIV by Anantharaman (2014) ($Re \approx 10500$).	58
C.1	Computational meshes used for getting the RANS results. a: Coarse mesh; 10 prism layer cells and a cell base size of 0.7 mm. b: Finer mesh; 20 prism layer cells and a cell base size of 0.4 mm. c: Finest mesh; 30 prism layer cells and a cell base size of 0.2 mm.	76
C.2	Fully developed turbulent profiles obtained with RANS using the $k-\epsilon$ and $k-\omega$ model for two exploratory meshes. a: Normalized axial velocity component. b: Normalized TKE.	77

C.3	Fully developed turbulent scales obtained with RANS using the $k-\epsilon$ and $k-\omega$ model for different meshes. a: TLS, TMS, and KLS at $z/D = -2$ (fully developed pipe flow) and $z/D = 2$ (recirculation zone) from orifice. b: Turbulent length scale at $z/D = -2$ (fully developed pipe flow) and $z/D = 2$ (recirculation zone) from orifice.	78
D.1	Used computational meshes with settings tabulated in Table 4.1. a: Cross section of Grid 1 (cell base size is 0.7mm, 10 prism layer cells). b: Orifice region of Grid 1 (cell base size is 0.7mm, 10 prism layer cells). c: Cross section of Grid 2 (cell base size is 0.5mm, 12 prism layer cells). d: Orifice region of Grid 2 (cell base size is 0.5mm, 12 prism layer cells). e: Cross section of Grid 3 (cell base size is 0.5mm, 25 prism layer cells). f: Orifice region of Grid 3 (cell base size is 0.5mm, 25 prism layer cells). g: Cross section of Grid 4 (cell base size is 0.35mm, 25 prism layer cells). h: Orifice region of Grid 4 (cell base size is 0.35mm, 25 prism layer cells). i: Cross section of Grid 5 (cell base size is 0.35mm, 5 prism layer cells). j: Orifice region of Grid 5 (cell base size is 0.35mm, 5 prism layer cells). k: Cross section of Grid 6 (cell base size is 0.35mm, 12 prism layer cells). l: Orifice region of Grid 6 (cell base size is 0.35mm, 12 prism layer cells). m: Cross section of Grid 7 (cell base size is 0.35mm, 8 prism layer cells). n: Orifice region of Grid 7 (cell base size is 0.35mm, 8 prism layer cells). o: Cross section of Grid 8 (cell base size is 0.2mm, 10 prism layer cells). p: Orifice region of Grid 8 (cell base size is 0.2mm, 10 prism layer cells).	82
E.1	The development of quantities as a function of the upstream distance to the inlet. a: The wall shear stress. b: The bulk TKE normalized with the bulk velocity squared.	83
E.2	Development of quantities as a function of the upstream distance to the inlet. a: Bulk velocity. b: Centerline axial velocity component normalized with the bulk velocity.	83
E.3	Development of the TKE as a function of the upstream distance to the inlet. a: Bulk TKE normalized with the bulk velocity squared. b: Maximal TKE normalized with the bulk velocity squared.	84
E.4	Wall shear stress as a function of the computational grid properties. a: As a function of the cell size in bulk region. b: As a function of the cell size of last prism layer. c: As a function of fraction of the cell size of the layer prism layer and the cell size in bulk region. d: As a function of the stretching factor.	84

List of Tables

3.1	Specifications of the experiments performed at ASML and TU/e.	18
4.1	Properties of the proposed computational grids for LES.	31
4.2	The CPU speed up and the efficiency on a computational grid consisting of 262k cells.	36
4.3	Details of the performed simulations.	38
5.1	The simulated wall shear stress and the computational grid properties.	43
6.1	Pressure and force data by LES on different computational grids.	49
6.2	Values for the turbulent viscosity ratio ($TVR = \mu_T/\mu$) and the subgrid kinetic energy to TKE ratio ($M_{TKE} = k_{SGS}/(k_{SGS} + k_{res})$) simulated with LES on different computational grids.	57

List of Symbols & Abbreviations

Abbreviations

CD	Central Difference
CFD	Computational Fluid Dynamics
CFL	Courant–Friedrichs–Lewy
DNS	Direct Numerical Simulation
EXP	Experiment
FIV	Flow-Induced Vibrations
FOU	First-Order Upwind
FVM	Finite Volume Method
ILES	Implicit Large Eddy Simulation
KLS	Kolmogorov Length Scale
LES	Large Eddy Simulation
NVD	Normalized Variable Diagram
PIV	Particle Image Velocimetry
PL	Prism Layer
PSD	Power Spectral Density
RANS	Reynolds-Averaged Navier–Stokes
RPM	Recycling Plane Method
SEM	Synthetic Eddy Method
SGS	SubGrid-Scale
SOU	Second-Order Upwind
TDR	Turbulent Dissipation Rate
TI	Turbulent Intensity
TKE	Turbulent Kinetic Energy
TLS	Turbulent Length Scale
TMS	Taylor MicroScale
UBF	Upwind Blending Factor
URANS	Unsteady RANS

URF	UnderRelaxation Factor
WALE	Wall-Adapting Local-Eddy Viscosity
WMLES	Wall Modelling Large Eddy Simulation
WRLES	Wall Resolved Large Eddy Simulation

Roman symbols

ℓ	Turbulent length scale	[m]
ℓ_0	Length scale of a large energy-containing eddy	[m]
\mathcal{L}	Largest flow scale	[m]
A_h	Cross sectional orifice hole area	[m ²]
A_p	Cross sectional pipe area	[m ²]
C_d	Discharge coefficient	[-]
C_f	Skin friction coefficient	[-]
C_w	WALE model constant	[-]
CS	Cell size	[m]
D_p	Pipe diameter	[m]
E	Kinetic energy of the flow	[J]
e	Internal energy	[J]
E'	Wall function coefficient	[-]
E_r	Wall function	[-]
E_{zz}	One-dimensional energy spectrum in axial direction	[m ² /(s ² Hz)]
f	Frequency	[Hz]
f_f	Friction factor	[-]
f_r	Roughness function	[-]
K	Von Kármán constant	[-]
k_{res}	Resolved turbulent kinetic energy	[m ² /s ²]
k_{SGS}	Modelled turbulent kinetic energy	[m ² /s ²]
M	Mach number	[-]
M_{TKE}	Subgrid kinetic energy to TKE	[-]
Q	Volume flow rate	[m ³ /s]
q	Hydrodynamic pressure	[Pa]
Re	Reynolds number based on pipe diameter	[-]
$Re_{\mathcal{L}}$	Reynolds number based on the largest flow scale	[-]
s	Strain rate tensor	[1/s]
S_w	WALE model constant	[1/s]
SF	Stretching factor	[-]
St	Strouhal number	[-]

T	Lighthill's turbulent stress tensor	[Pa]
t_ℓ	Turbulent time scale	[s]
t_η	Kolmogorov time scale	[s]
TVR	Turbulent viscosity ratio	[-]
U_b	Bulk velocity	[m/s]
u_h	Hole velocity	[m/s]
V_c	Computational cell volume	[m ³]
y	Distance to the wall	[m]
y^+	Distance to the wall in wall units	[-]
c	Speed of sound in water	[m/s]
F	Force acting on fluid volume	[N]
I	Turbulent intensity	[-]
k	Turbulent kinetic energy	[m ² /s ²]
m	Mass	[kg]
p	Pressure	[Pa]
t	Time	[s]
u	Velocity	[m/s]
x	Distance	[m]

Greek symbols

β	Orifice hole to pipe diameter	[-]
Δ	Filter width in LES	[m]
δ_p	Total prism layer thickness	[m]
δ_{ij}	Dirac delta function	[-]
ϵ	Energy dissipation rate	[m ² /s ³]
η	Kolmogorov length scale	[m]
γ	Normalized two-point cross correlation	[-]
κ	Wave number	[1/m]
λ	Taylor miscoscale	[m]
μ	Dynamic viscosity	[Pa s]
μ_T	Dynamic eddy viscosity	[Pa s]
ν	Kinematic viscosity	[m ² /s]
ν_T	Kinematic eddy viscosity	[m ² /s]
ϕ	Arbitrary variable	[multiple]
$\Phi_{\phi\phi}^*$	Non-dimensionalized power spectral density of an arbitrary variable	[multiple]
$\Phi_{\phi\phi}$	Power spectral density of an arbitrary variable	[multiple]
ρ	Fluid density	[kg/m ³]

τ_T	Turbulent shear stress	[Pa]
τ_w	Wall shear stress	[Pa]
τ_v	Viscous shear stress	[Pa]
θ	Angle between radial and tangential component	[rad]
ξ	Normalized variable in numerical scheme	[-]

Symbols

$\check{\phi}$	Sub-filtered arbitrary variable in LES	[multiple]
$\Delta\phi$	Difference of arbitrary variable	[multiple]
$\tilde{\phi}$	Filtered arbitrary variable in LES	[multiple]
$\bar{\phi}$	Mean of an arbitrary variable in LES	[multiple]
ϕ'	Fluctuations in time of arbitrary variable signal	[multiple]
ϕ_{rms}	Root mean square of an arbitrary variable	[multiple]

Chapter 1

Introduction

ASML is currently developing and improving her new Extreme UltraViolet (EUV) lithography machines. These machines are able to manufacture computer chips with structures as small as 13 nm. A general goal of ASML is to decrease the structure size. A smaller structure size decreases the travelling distance of an electrical signal. If this distance decreases, the performance of the computer chip increases. The heart of a EUV machine in which these chips are manufacture is depicted in Figure 1.1. Ultraviolet light is emitted by a source and is afterwards going through an illuminator to the reticle. The reticle contains the blue print of the structure and adds that to the light. Light is then entering the Projection Object Box (POB). In the POB mirrors reflect light to the wafer where the printing process starts.

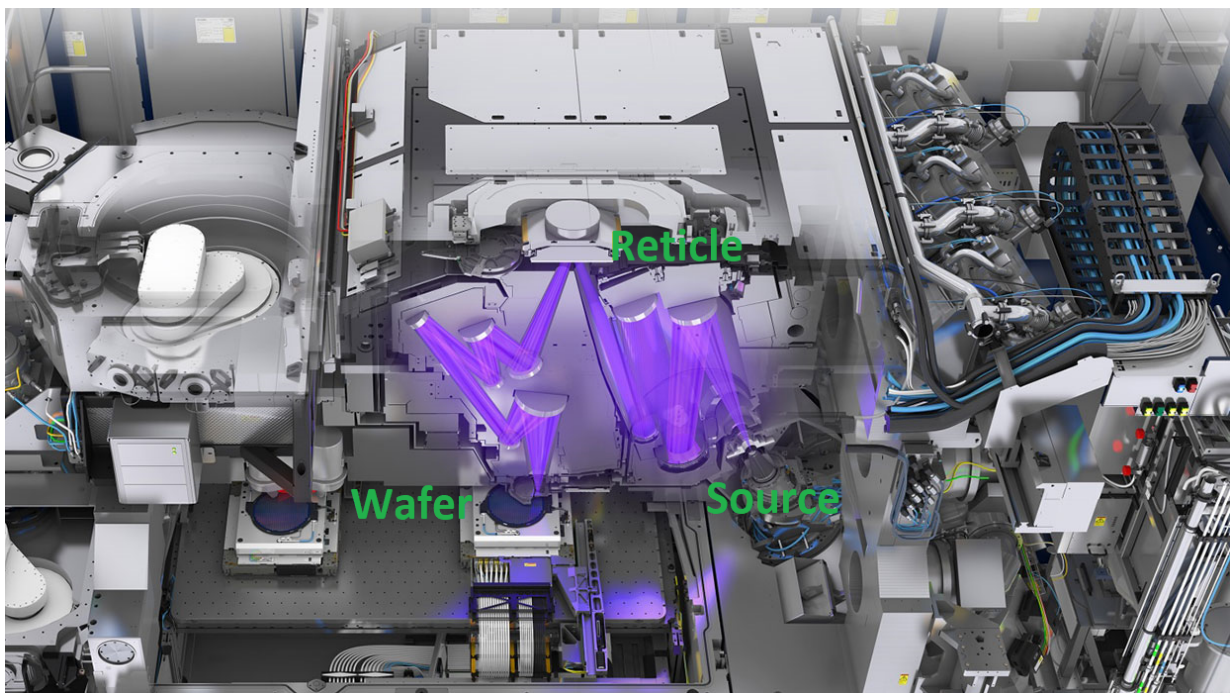


Figure 1.1: EUV deployed to write structures on a wafer. The source emits light on a reticle containing a blue print. This image is then reflected via mirrors to the wafer where the structure is printed on a silicon plate.

Mirrors in the POB are hanging in a force frame. The location of the force frame is measured with a sensor frame which surrounds the force frame. Additionally, the location of the wafer stage is measured. This wafer stage carries and moves the wafer. To obtain small structure sizes on the computer chip, all frames should be perfectly aligned. However, this is a very difficult task as the frames are in the vicinity of vast heat sources. To guarantee alignment of the frames, thermal expansion of components should be

avoided. Therefore the temperature of the frames are controlled up to a millikelvin-level. This temperature control is achieved using a cooling water system. However, the usage of a cooling water system comes with additional vibrations due to water disturbance in the cooling pipes. This problem is the topic of this thesis.

These vibrations of the cooling system, referred to as Flow-Induced Vibrations (FIV), are caused by a disturbance of internal fluid (R. D. Blevins (2001)). In a wide range of industries this phenomenon causes severe problems. Examples are found in nuclear industries in which this leads to failure of structures (R. Blevins (1979); Bush (1992)). In the high precision machines of ASML, however, flow-induced vibrations simply affect the intended tight tolerances negatively. The inaccuracies by FIV will shift of the line of sight in the order of picometers, which should be avoided. Whereas FIV was relatively unimportant a decade ago, it is now a hot topic adhering ASML's slogan: 'Changing the world, one nanometer at a time'.

Fluid disturbances, in the form of acoustic noise, cause water cooling pipe wall excitations. Acoustic noise is propagating as pressure waves with the speed of sound in the form of one-dimensional plane modes and higher order modes. These modes are able to travel long distances and interfere with pipe corners which in turn excite a motion of the system (R. D. Blevins (2001)), indicated by red arrows in Figure 1.2. This fluid-structure interaction phenomenon is initiated by components that disturb the flow, depicted in Figure 1.2 as the brown blocks with green arrows. Water is provided by a cabinet and is distributed through the system by Liquid Cooling Water (LCW) lines. As pressure waves tend to propagate far up- and downstream, a coupling exists between the noisy ambient and the vacuum environment in the machine, see Figure 1.2. This raises the problem that generated acoustic noise in the ambient region also affects the sensitive vacuum region, as well as directly generated disturbances in that region.

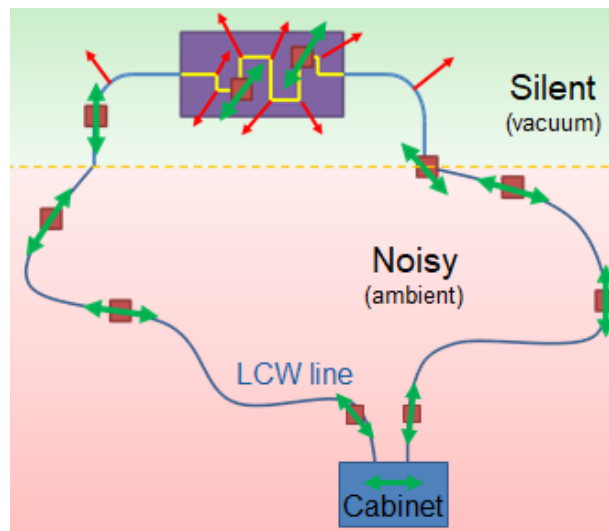


Figure 1.2: Water cooling system containing a sensitive and nonsensitive region. The brown parts are disturbing components generating a flow disturbance indicated by a green arrow. Resulting excitations of the piping system are indicated by a red arrow.

Water cooling circuits in ASML's machines consist various types of these flow disturbing components which cause flow disturbances (green arrows), illustrated as brown blocks in Figure 1.2. An example of a FIV-active applied component is a single-hole orifice (Agarwal (1994b)). Orifices are deployed to generate a significant pressure drop (Cairns, Whitson, Strachan and Wheel (1970)) and are specifically used for flow balancing, i.e. to control mass flow rates. As every cooling branch in the cooling system has its own resistance, the orifices are essential to guarantee the prescribed mass flow rate and can therefore not be removed. Other examples of FIV-active components are changes in flow area and sharp bends as mentioned by Bull and Norton (1981), which are equally important.

These disturbing components are known to generate significant noise locally, referred to as turbulence or pseudo noise (Moussou (2006)). Generally, direct effects of these hydrodynamic pressure fluctuations

damp out after about six diameters (Anantharaman (2014); Anantharaman, Waterson, Nakiboglu, Persin and van Oudheusden (2016); Moussou (2006); Qing, Jinghui, Yushan, Haijun and Quan (2006); Tao et al. (2017)), and are therefore of no problem in non-sensitive parts of the machine. In sensitive parts the cooling pipe is designed smooth such that no strong hydrodynamic fluctuations cause pipe wall vibrations. However, besides local hydrodynamic pressure fluctuations, other types of noise exist (Hirschberg (2007)). A phenomenon possibly playing a large role in total noise generation is cavitation (Ebrahimi et al. (2017); Testud, Moussou, Hirschberg and Aurégan (2007)). It is assumed that ASML machines are designed such that cavitation does not occur and is therefore left out of the analysis in this thesis. Additionally, acoustic noise contributes to the total noise level which is dominant in low Mach number regimes far from sources according to Michalke (1989) and Rienstra and Hirschberg (2001). Thus, despite designing for smooth non-disturbing water cooling pipes in sensitive regions, noise should be expected from the noisy machine part. Certain levels of noise from a cooling water system is inevitable. In line with this, Moussou (2006) mentioned that a far field coupling exists between the generated pressure and a structure.

At ASML every part of the machines has a budget to which level it may add an inaccuracy to the system. The budget of FIV is measured via pipe wall vibrations. These pipe wall vibrations are computed with PlaNet3D. This tool translates the disturbance by a FIV-active component to pipe wall accelerations. The principles of these tools are described later, but it should be mentioned that the input is a description of the source term generating the noise. First of all this requires a proper understanding of the mechanism generating the noise. Secondly, this source term should be provided. However, as the equations governing flow are non-linear, it is difficult to accurately predict the source term under conditions they do produce sound according to Hirschberg (2007). Additionally, only the resulting acoustic noise can be measured rather than the source term itself. Despite this, a determination of source term characteristics is possible using a scaling law based on mean flow parameters (Moussou (2006)), but is rather general.

As of the above, it is not within the possibilities of ASML to come up with an accurate description of the source term. At the moment this is done by simply measuring one-sided pressure fluctuations. But, this method is assumed inaccurate. Because of that there is a need to have a proper understanding and description of the source term that disturbs fluid in the water cooling system of ASML machines. The work in this thesis is to fulfill this need. An encouraging method do so is using Computational Fluid Dynamics (CFD) software. Using a transient solver like Large Eddy Simulation (LES) should give the option to extract this fluctuating source term. A commercial CFD package STAR-CCM+ is available to carry this out. This method, however, can be very costly in terms of computational time and therefore a practical approach is adopted to obtain quick answers. The title of the thesis is therefore: ‘Determination of the source term disturbing bounded flow using practical Large Eddy Simulations’.

1.1 Research questions

Summarizing; in the current approach of ASML, the modelling tool PlaNet3D is used to generate pressure fluctuations with which it models forces on structures. With these forces, pipe wall accelerations are calculated to subsequently come up with an estimate of the error of the line of sight of the printing process onto the wafer. Accurate and real pressure signals, though, require an accurately described source terms. In order to provide this, the following questions raise

- What mechanisms generate acoustic noise in the presence of an orifice in turbulent water pipe flow?
- Is there a significant single source term accountable for generating the acoustic noise? If so, what is the nature of the source term that induces acoustic noise? Additionally, if this is the case, why are measurements not suitable for determining this disturbing source?

Answers to these questions are crucial before starting analyzing the flow behavior with a commercial CFD package. Concerning the simulations specifically, the following research questions are to be answered

- Is LES a promising simulation tool for determining the full behavior of the source term?
- Is it possible to create a general setup to determine the disturbing source term in different bounded flow geometries?
- Can accurate simulation results be obtained for engineering purposes within a week using practical LES?

These questions need to be answered to get insight in the usability of LES in future design processes. All in all, the above itemized research questions are to be answered in order to solve the problem ASML faces concerning flow-induced vibrations in the process of machine design improvement.

1.2 Research approach

With the research questions in mind, a research approach is proposed to solve the described problem. The research questions give direction in this and partly determine the approach. The outline of the thesis is illustrated in Figure 1.3. In Chapter 2 the relevant literature will be reviewed. Topics are treated which are related to the research questions. Answers to the first research questions are already given in the conclusion of this chapter. Chapter 3 will consist of a summary of experimental results obtained mainly at ASML and the TU/e. This will provide a better understanding of the problem and later on this data will be used for comparison with simulation results.

Chapter 4 describes the numerical approach to determine the source term. The simulation setup choices and a description of the theory behind the simulations will be elaborated on. In chapter 5 and 6 simulation results will be given. Chapter 5 is focusing on the flow through a straight pipe, mainly to distinguish between and understand different simulations setup results. In chapter 6 LES results of a straight pipe including an orifice will be discussed. To obtain these results, design choices are based on the results of the straight pipe analysis. In the last two chapters, conclusions are drawn and the scope for future work is proposed.

In the appendices different topics are described: the first appendix gives a detailed step approach to derive an analytical solution for the coupling of pressure and source fluctuations, the second appendix gives a summary to setup a simulation as used in this thesis, the third appendix summarizes RANS simulations performed to serve as background for the numerical approach for transient simulations, the fourth appendix gives illustrations of the used computational grids, and the fifth appendix provides additional results of the straight pipe analysis.

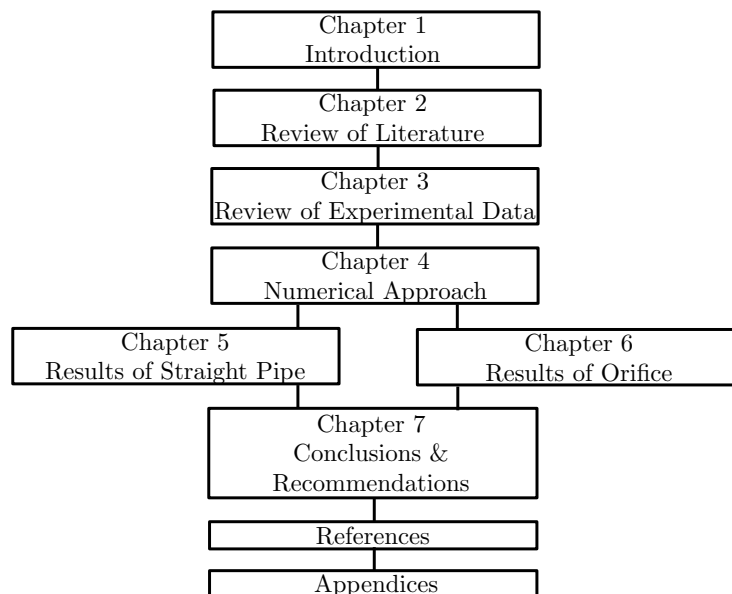


Figure 1.3: The outline of the thesis.

Chapter 2

Review of Literature

In this chapter a review of the literature is given. This information is required to answer the first two research questions. First the governing equations are given. Then a description of the tool PlaNet3D is provided. This clarifies the need for a source term description. Afterwards all the information concerning flow induced noise is treated. Then the flow through orifices is elaborated on investigating the possible mechanisms generating noise. Thereafter, the nature of possible sources are studied and it is determined which source is dominant in this problem. A possible exact solution to couple pressure and source fluctuations is investigated next. Afterwards, a review of experimental work done outside of ASML regarding measuring flow noise is provided. Finally, a list of CFD studies on orifice flow is given.

2.1 Governing equations

In this work flow is assumed incompressible. The Navier-Stokes equations describe the motion of this flow. For incompressible flow, these governing equations are given in conservative form as (J. Anderson (2016))

$$\frac{\partial u_i}{\partial x_i} = 0 \quad (2.1)$$

$$\rho \frac{\partial u_i}{\partial t} + \rho \frac{\partial (u_i u_j)}{\partial x_j} = -\frac{\partial p}{\partial x_i} + \mu \frac{\partial^2 u_i}{\partial x_j \partial x_j} + F_i \quad (2.2)$$

These are respectively the conservation equations of mass and momentum. Here ρ is the density, u_i is the velocity component in i -direction, p is the static pressure and μ is the dynamic viscosity. The index notation is such that $i = [1, 2, 3]$ representing the radial, tangential and axial component respectively. In the momentum equation, see Equation 2.2, F_i represents internal/external forces acting on fluid per unit volume. Dividing the momentum equation by the density and rewriting the viscous term results in

$$\frac{\partial u_i}{\partial t} + \frac{\partial (u_i u_j)}{\partial x_j} = -\frac{1}{\rho} \frac{\partial p}{\partial x_i} + \frac{\partial}{\partial x_j} \left[\nu \left(\frac{\partial u_i}{\partial x_j} + \frac{\partial u_j}{\partial x_i} \right) \right] + \frac{F_i}{\rho} \quad (2.3)$$

Here, ν , is the kinematic viscosity. In square brackets now the viscous stress tensor for incompressible fluids, τ_{ij} , arises. Note that these viscous stresses are typically low for highly turbulent flows. In this momentum equation, the left hand side represents the temporal and spatial change in fluid momentum. When averaging the convective term $\rho u_i u_j$ in time the turbulent stresses appear.

2.2 Pipe excitation prediction tools

An often used tool to predict pipe wall acceleration is the inhouse tool PlaNet3D (Kemper (2014)). It is based on a lumped-mass representation of a fluid network. It enables to model fluid-structure interactions because the geometry and fluid hydraulics are coupled. Using this tool, it is assumed that pressure waves

can be described by the one-dimensional acoustic wave equation. Under some assumptions this is true (Kao, Graham, Knight and Pericleous (2007)). The one-dimensional wave equation is given by

$$\frac{1}{c^2} \frac{\partial^2 p'}{\partial t^2} - \frac{\partial^2 p'}{\partial x^2} = \frac{\partial F'}{\partial x} \quad (2.4)$$

Here, p' is the fluctuating static pressure and c is the speed of sound in water. Comparing the mass and momentum conservation equations with those for a mass-spring system, these are analogous and therefore the fluid can be regarded as a lumped mass-spring system. Such a system is depicted in Figure 2.1 and is governed by

$$m\ddot{x} + (C_1 + C_2)x = F_{w \rightarrow f} \quad (2.5)$$

The force $F_{w \rightarrow f}$, here presented as a force from wall to fluid, is internally induced by the flow. The mechanisms that bring about this force will be studied later on. In Equation 2.5 the stiffness C is analogous to KA_p/L for flow. L is the duct element length, K is the fluid bulk modulus, and A_p is the cross sectional pipe area. The input parameter required is the force of the disturbance part on the fluid. With that the pressure waves are initiated and the resultant forces on parts of the network are modelled.

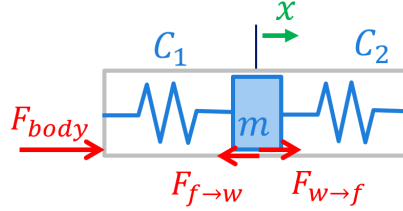


Figure 2.1: Lumped mass-spring system used in PlaNet3D to represent acoustic pressure waves in fluid flow.

2.3 Turbulence

To understand the phenomenon generating noise, and to understand length and time scales in upcoming simulations, a firm understanding of turbulence is needed. Turbulence is a phenomenon in which chaotic motions with excessive kinetic energy overcome the damping effect of the viscosity. It is characterized by changes in pressure and velocity and plays a key role in the generation of noise and pressure drops. Turbulent flows consist of eddies, or vortices, with a spectrum of length and time scales. In such flows larger eddies are unstable and break up and with that transfer their energy to smaller eddies driven by vortex stretching (Richardson (1922)). This is summarized in the energy cascade (Richardson-Kolmogorov cascade) and continues until Reynolds numbers are small enough so that the turbulent kinetic energy (TKE), k , is dissipated into heat through the action of molecular viscosity. TKE consists of the fluid shear stresses for $i = j$, which are the variances of the velocity components in axial, radial and tangential direction, defined as

$$k = \frac{1}{2} \sum \left(\overline{u_i'^2} \right) \quad (2.6)$$

The axial direction is defined in thesis as the z-direction. The components are determined by calculating the mean fluctuation of a time signal squared. Note that this is only legit in the directions $i = j$. To determine the turbulent shear stresses ($i \neq j$), $\overline{u_i' u_j'}$, Reynolds' decomposition is used which is $\phi = \bar{\phi} + \phi'$. $\bar{\phi}$ indicates the mean of a variable, and ϕ' indicates the fluctuations of a variable. With this, all turbulent stresses are calculated as

$$\overline{u_i' u_j'} = \overline{u_i u_j} - \bar{u}_i \bar{u}_j \quad (2.7)$$

From Cartesian coordinates, the radial and tangential velocity components are defined as

$$u_r = u_x \cos(\theta) + u_y \sin(\theta), \quad u_t = -u_x \sin(\theta) + u_y \cos(\theta) \quad (2.8)$$

Here, θ is the angle between the radial and tangential component in radian. In the energy spectrum, scales containing most turbulence kinetic energy are characterized by the large energy-containing eddies,

ℓ_0 , given as

$$\ell_0 = \frac{k^{\frac{3}{2}}}{\epsilon} \quad (2.9)$$

Here, ϵ is the turbulence dissipation rate (TDR) which is the rate at which TKE is dissipated into thermal energy. Most of the energy is present in a turbulent length scale (TLS) range of $\frac{1}{6}\ell_0 < \ell < 6\ell_0$. This range is referred to as the energy-containing range, depicted in Figure 2.2a. In this range typically energy is injected to the flow. Note that in Figure 2.2a, \mathcal{L} is the largest flow scale.

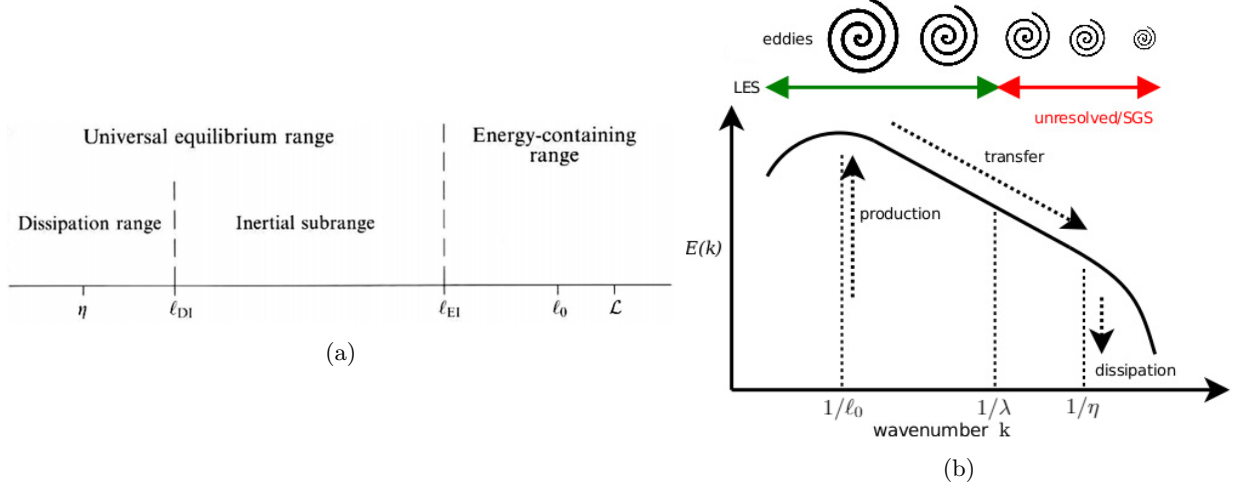


Figure 2.2: a: Characteristic eddy sizes in turbulent flow (Pope (2001)). b: Energy cascade.

The smallest scales in turbulent flows are characterized by Kolmogorov (1941)

$$\eta = \left(\frac{\nu^3}{\epsilon} \right)^{1/4} \quad (2.10)$$

At this smallest scale, the Kolmogorov length scale, η , TKE of fluid flow is dissipated into heat. Only these dissipative eddies experience significant effect of molecular viscosity. Eddies with a length scale of $\ell < 60\eta$ do cover the dissipation range, also illustrated in Figure 2.2. Last, a range exists in between the range at which most of the energy is present and the range at which most energy is dissipated. Motions of these turbulent structures are typically dominated by inertial effects. In this range, there is a continuous cascade of energy from larger to smaller turbulent scales. Energy is only transferred in this range as no energy is produced nor dissipated. In this range, a length scale exists at which turbulent structures get affected by viscous effects defined by Taylor. These Taylor microscales, λ , are given as (Pope (2001))

$$\lambda = \sqrt{15 \frac{\nu}{\epsilon} u'_i} \approx \sqrt{10 \nu \frac{k}{\epsilon}} \quad (2.11)$$

As already visible in Figure 2.2b, this length scale is important in CFD simulations. Along with all described length scales, time scales are important characterizing turbulent flow. Kolmogorov's time scale represents the eddy-turnover time of the very smallest scales as

$$t_\eta = \frac{\nu^{\frac{1}{2}}}{\epsilon} \quad (2.12)$$

For larger eddies, the eddy-turnover time is defined as

$$t_\ell = \frac{k}{\epsilon} \quad (2.13)$$

t_ℓ is a time scale for an eddy to traverse the inertial range. It is important to note that the magnitude of separation between both length and time scales increases as the Reynolds number increases respectively as

$$\frac{\eta}{\ell_0} \sim Re_{\mathcal{L}}^{-3/4}, \quad \frac{t_\eta}{t_\ell} \sim Re_{\mathcal{L}}^{-1/2} \quad (2.14)$$

$Re_{\mathcal{L}}$ is based on the bulk velocity, U_b , and largest flow scale.

2.4 Orifice flow

Often applied FIV-active components are orifices. In Figure 2.3, the mean flow through a single-hole orifice plate is depicted. By conservation of mass, water flowing through the orifice accelerates to compensate for the decrease in area resulting in the formation of a high velocity jet downstream of the orifice. Whereas the static pressure upstream of the orifice is high, it decreases just downstream of the orifice. According to Bernoulli's principle, the static pressure reaches its minimum at the vena-contracta which is where the jet velocity is highest. Further downstream, the static pressure increases again as a result of a decrease in flow velocity. However, a permanent total pressure loss over the orifice is achieved being a function of geometry and flow specifications as studied by Anantharaman (2014).

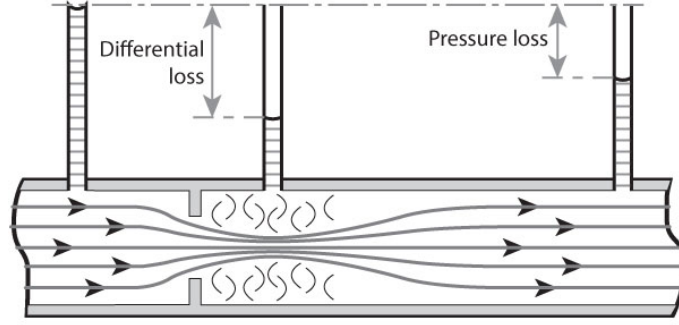


Figure 2.3: Pipe flow through a single-hole orifice, generating a pressure drop.

The maximum pressure drop over an orifice is given by (Bird, Stewart, Lightfoot & Klingenberg, 2015)

$$\Delta p_{\max} = \frac{1}{C_d^2} \frac{1}{2} \rho U_b^2 (\beta^{-4} - 1) \quad (2.15)$$

Here, C_d is the discharge coefficient and β is the orifice hole to pipe diameter ratio. The permanent pressure drop and maximal pressure drop can be related with the empirical relation

$$\frac{\Delta p_{perm}}{\Delta p_{\max}} = 1 - \beta^2 \quad (2.16)$$

Note that when the discharge coefficient is unity, Bernoulli's relation for static and dynamic pressure holds. The discharge coefficient, however, includes the effect of a direct pressure loss arising from zones of turbulent separated flow. To understand why a pressure drop is generated, conservation of energy has to be studied as done by Pope (2001) for jets. For incompressible flow through orifices at low Mach numbers, the decrease in mechanical power dissipation, or energy dissipation rate is given as

$$\epsilon = Q \Delta p_{perm} = Q \Delta \left(p + \frac{1}{2} \rho u^2 \right) = \bar{\epsilon} + \epsilon_k \quad (2.17)$$

where Q is the volume flow rate. The total decrease in mechanical energy should be equal to the increase of internal energy and turbulent kinetic energy according to Kundu, Dowling, Tryggvason and Cohen (2015). For a fixed control volume it should therefore hold that

$$- \iint_{\partial V} \rho u_i \left(\frac{p}{\rho} + \frac{u^2}{2} \right) dS = \iint_{\partial V} \rho u_i (e + k) dS \quad (2.18)$$

In here, e , is the internal energy. Both mechanisms at the right-hand side of Equation 2.18 are contributing to the resulting total pressure loss. The mechanisms of increase in TKE and internal energy are depicted in Figure 2.4. Here, D denotes the energy dissipation rate. Note that TKE is first produced and afterwards dissipated as already seen in Figure 2.2b. Production and dissipation of turbulence kinetic energy is producing the FIV disturbances.

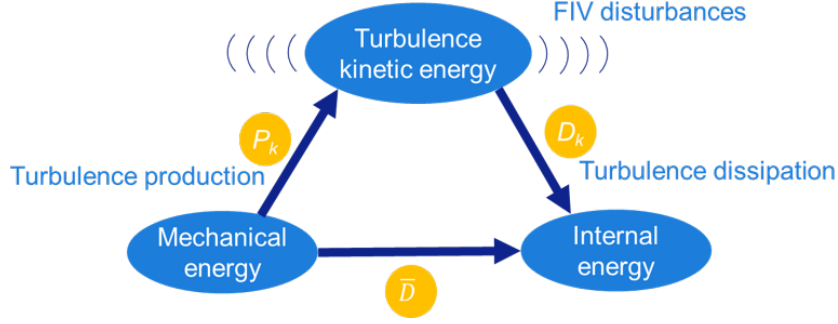


Figure 2.4: Mechanisms dissipating mechanical energy responsible for the permanent total pressure loss.

Considering the kinetic energy E of a fluid flow. According to Pope (2001), its mean can be decomposed into two parts as

$$\bar{E}(x_i, t) = \frac{1}{2} \bar{u}_i \bar{u}_i + \frac{1}{2} \overline{u_i' u_i'} \quad (2.19)$$

The first term is the kinetic energy of the mean flow whereas the second is the turbulence kinetic energy which followed from the Reynolds decomposition. Evolution of E based on the Navier-Stokes equations helps rewriting the components of Equation 2.19 respectively as (see Pope (2001))

$$\frac{\bar{D}\bar{E}}{\bar{D}t} + \frac{\partial \bar{T}_i}{\partial x_j} = -\mathcal{P} - \bar{\varepsilon} \quad (2.20)$$

$$\frac{\bar{D}k}{\bar{D}t} + \frac{\partial T_i'}{\partial x_j} = \mathcal{P} - \varepsilon_k \quad (2.21)$$

Here, T is the flux of energy, see Pope (2001). \mathcal{P} is the source producing turbulent kinetic energy and is called production and is defined as

$$\mathcal{P} \equiv -\overline{u_i' u_j'} \frac{\partial \bar{u}_i}{\partial x_j} \quad (2.22)$$

Sink ε dissipates kinetic energy as $\bar{\varepsilon} \equiv 2\nu \bar{S}_{ij} \bar{S}_{ij}$ and turbulence kinetic energy as $\varepsilon_k \equiv 2\nu \overline{s_{ij} s_{ij}}$ with mean and fluctuating rates of strain \bar{S}_{ij} and s_{ij} defined in general as

$$S_{ij} = \frac{1}{2} \left(\frac{\partial u_i}{\partial x_j} + \frac{\partial u_j}{\partial x_i} \right) \quad (2.23)$$

So the first mechanism transfers kinetic energy directly into internal energy by $\bar{\varepsilon}$ in Equation 2.20, indicated by \bar{D} in Figure 2.4. The second mechanism removes kinetic energy from the mean flow which by mean velocity gradients, see Equation 2.20, is transferred to the fluctuating velocity field in Equation 2.21 by production, indicated by P_k in Figure 2.4. Consequently, this formed turbulent kinetic energy working against fluctuating stresses results its transformation into internal energy, indicated by D_k in Figure 2.4. Generally, a permanent total pressure loss in static pressure arises from the large mean and fluctuating velocity gradient between the jet and recirculation zones causing dissipation of energy (Van der Zande (2000)). Both are contributing to the total shear stress in fluid flow defined as

$$\tau_{total} = \tau_v + \tau_T = \mu \left(\frac{\partial u_i}{\partial x_j} + \frac{\partial u_j}{\partial x_i} \right) - \overline{\rho u_i' u_j'} \quad (2.24)$$

As for the viscous shear stress affected by molecular viscosity, an eddy viscosity exists relating the turbulent shear stress to the velocity gradient, as will be seen later.

2.5 Flow noise

Flow noise can be described as deviations from a mean fluid state: $\phi' = \phi - \bar{\phi}$. An example is given by hydrodynamic fluctuations, occurring in the jet-wake region (Anantharaman (2014)). This is also referred

to as pseudo noise as this type of noise does not radiate in fluids in the form of acoustic waves. This type of noise arises from turbulent separation followed by flow reattachment to the wall. This type is not considered as this cannot generate pipe accelerations elsewhere in the system. The sound focused on in this thesis is able to radiate and propagates in the form of acoustic waves through fluids with the speed of sound. These waves propagate linearly in stationary and homogeneous fluids. The momentum equation can be linearized, neglecting second order terms, as

$$\frac{\partial(\rho u_i)}{\partial t} = -\frac{\partial p}{\partial x_i} \quad (2.25)$$

For flow speeds much smaller than the speed of sound in water, flow can be assumed to be incompressible (Wagner, Hüttl and Sagaut (2007)). The speed of sound for fluid is given (via the bulk modulus) as

$$c = \sqrt{\frac{dp}{d\rho}} \quad (2.26)$$

Using this, and combining the mass conservation equation (Equation 2.1) and the linearized momentum equation (Equation 2.25) results in the homogeneous wave equation

$$\frac{\partial^2 \rho'}{\partial t^2} - c^2 \frac{\partial^2 \rho'}{\partial x_i^2} = 0 \quad (2.27)$$

In Equation 2.27, the density can be interchanged with the acoustic pressure fluctuations p' . Note that combining the mass and momentum equation is required to couple the source term with the pressure fluctuations. The one-dimensional solution to this homogeneous wave equation reads

$$p'(z, t) = g(z - ct) + h(z + ct) \quad (2.28)$$

Here, g and h represent waves propagating in the positive and negative axial direction. In those plane waves, the pressure is typically constant. One-dimensional travelling waves exist when the wavelength of the waves is much larger than the characteristic length according to Rienstra and Hirschberg (2001)

$$f < \frac{c}{2D_p} \quad (2.29)$$

In a frequency range up until almost $f = 10^5$ Hz this is the case, which is in the range of interest for ASML. This, however, introduces the problem that energy content can be transported for long distances without decreasing in level significantly. This means that flow disturbances at non-sensitive locations can lead to FIV at sensitive locations.

2.6 Noise generation

In orifices plates, acoustics can be divided into two parts. On the one hand orifices scatter sound passively. On the other hand orifices generate sound actively, for example generating a standing wave. In this thesis only the active property is studied. This active generation of sound can arise from several different mechanisms. These mechanisms can be categorized in three noise types; monopole noise, dipole noise, and quadrupole noise, see Figure 2.5. In confined flow with impermeable walls, however, monopole noise, see Figure 2.5a, is not generated directly or indirectly by orifices and is left out of scope in this thesis. This type of noise namely arises from fluctuating volume flow which is not the case without mass injection or leakage. Note that this type of noise may be introduced by e.g. pump behavior in experimental setups (Moussou, Lafon, Potapov, Paulhiac and Tijsseling (2004)).

2.6.1 Quadrupole noise

Quadrupole noise is generated by turbulent fluctuations in free fields or by varying tangential shear stresses at surfaces (Alenius (2012)). In the separation zone downstream of the orifice, an adverse pressure gradient forms whenever the static pressure increases in downstream direction. This results in fluid reversal close to the wall (Anantharaman et al. (2016); Bull and Agarwal (1983)), referred to as reversed flow, which

is the reason for flow separation. Later on the flow reattaches to the wall at the reattachment point. This point is experimentally found to be variable in time by Bull and Agarwal (1983), indicating that the pressure gradient pattern is not steady and thus the tangential shear stress will vary. Varying wall shear stresses are experimentally studied for back-facing step flow by Spazzini, Iuso, Onorato, Zurlo and Di Cicca (2001). This involves vortex formation and breakdown attributed to the flapping motion. These vortices are responsible for mixing and intensive fluid behavior. W. K. Blake (1986) explains noise to be generated whenever vortex lines are stretched or accelerated relative to the acoustic medium. The existence of vortex shedding producing sound occurs in particular for orifices with sharp or downstream rounded edges (A. Anderson (1955); Rienstra and Hirschberg (2001)).

Lighthill (1952) initiated a theory describing the acoustic quadrupoles radiating sound in fluid flow. Without simplifying the conversation equation of mass and momentum, a non-homogeneous wave equation is presented

$$\frac{\partial^2 \rho}{\partial t^2} - c^2 \frac{\partial^2 \rho}{\partial x_i^2} = \frac{\partial^2 T_{ij}}{\partial x_i \partial x_j} \quad (2.30)$$

The additional source term at the right hand side of Equation 2.30, T_{ij} , is the Lighthill turbulent stress tensor defined as

$$T_{ij} = \rho u_i u_j - \tau_{ij} + (p - c^2 \rho) \delta_{ij} \quad (2.31)$$

Physically this means that sound produced by fluid flow can be compared with a medium at rest subjected to externally applied fluctuating stresses. In this free-field fluctuating stresses thus behave as sound generating quadrupoles. Lighthill (1952) has shown that for sufficiently low Mach numbers this stress tensor term reduces to

$$T_{ij} \approx \rho u_i u_j + \mathcal{O}(M^2) \quad (2.32)$$

Here, M is the Mach number defined as the water velocity over the speed of sound. The viscous stress term (deviatoric stress) is neglected because of the dominance of inertial effects and the pressure stress term (volumetric stress) is neglected because of low density fluctuations. This is legit in the treated case.

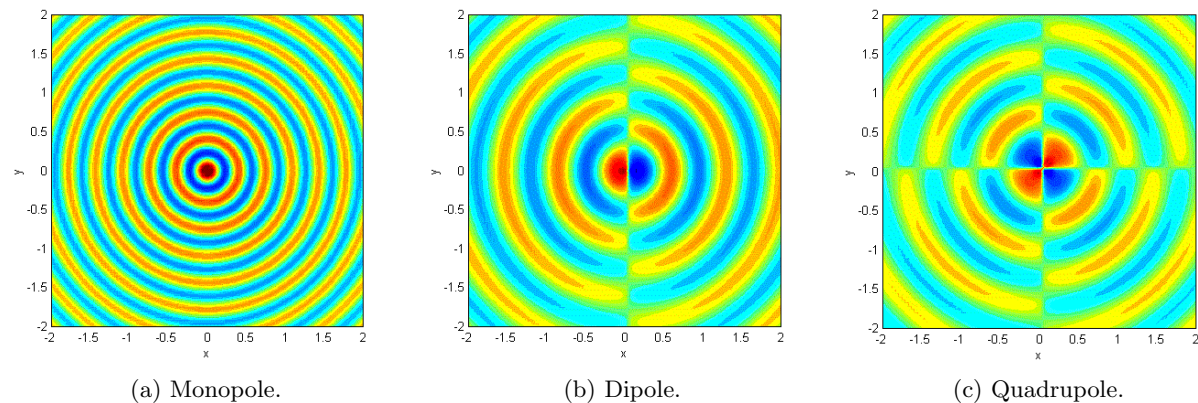


Figure 2.5: The sound fields produced by the different source terms.

2.6.2 Dipole noise

Whereas quadrupole noise arises from free field turbulence, dipole noise is generated when an fluctuating external force is applied on a medium, already clarified by Lighthill (1952). Obviously, in the vicinity of bodies this is likely the case (W. K. Blake (1986); Junger and Feit (1986)). One should think of mechanisms as vortices hitting surfaces, unsteady vortex shedding, and unsteady flow separation that cause these fluctuating forces on surfaces. Try this by comparing blowing in free field and disturbing the flow with an object. Dipole noise is introduced and a higher acoustic level is noticed.

Distribution of turbulent flow over a surface results in normally oriented dipole sources to that surface. These dipole sources are distributed in axial direction over the orifice surface as the orifice is perpendicular to the flow. The strength of this total source depends on the level of unsteady aerodynamic loading (Tao

et al. (2017)). Physically, the noise generating source may be regarded as a piston moving back and forth in a pipe. Alenius (2014) concluded that for compressible pipe flow with orifice, the main sound generating mechanism is fluctuating surface forces at orifice sides caused by strong passing vortex rings. Similarly, W. K. Blake (1986) describes dipole sound to be produced when vortex lines are stretched or accelerated relative to a body in the flow, as forces are exerted on the body-fluid interface.

Curle (1955) continued on Lighthill's work including the influence of solid boundaries upon the sound field. Incorporating the external force, as shown in Equation 2.2, an additional source term appears

$$\frac{\partial^2 \rho}{\partial t^2} - c^2 \frac{\partial^2 \rho}{\partial x_i^2} = \frac{\partial^2 T_{ij}}{\partial x_i \partial x_j} - \frac{\partial F_i}{\partial x_i} \quad (2.33)$$

Besides including the additional source term at the right hand side of the wave equation, Curle (1955) explained that the contribution of sound generation by dipoles sources is most relevant for flows with low Mach number. It is thus more efficient in radiating sound compared to quadrupole type sources. This is especially true in the far field which is of interest in this thesis.

2.6.3 Dominant source term

Two distinct sources may thus be regarded deriving the sound field. These are the fluctuating applied stresses as in Lighthill's theory, and the fluctuating force with which solid boundaries interact with the fluid as in Curle's theory. Lighthill (1952) and Curle (1955) have provided definitions for the intensities of sound generated by either free field turbulence or turbulence interacting with solid bodies. The dominance of both phenomena are studied by Michalke (1989). Howe (2003) summarized the total power radiated in turbulent regions by quadrupoles and dipoles respectively as

$$\Pi_q \propto \frac{V_0}{\ell_0} \rho_0 u^3 M^5 \quad (2.34)$$

$$\Pi_d \propto A \rho_0 u^3 M^3 \quad (2.35)$$

In here, ℓ_0 is the length scale of large energy-containing eddies, V_0 is the volume of the turbulent region, and A is the total surface area wetted by the turbulent flow. In Figure 2.6 an eddy radiating sound in a turbulent region is given.

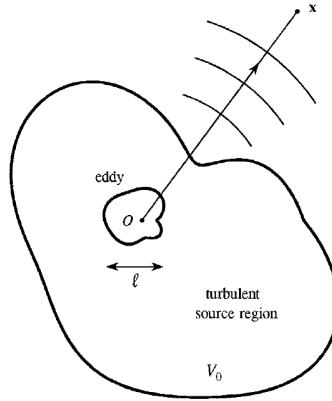


Figure 2.6: Eddy radiating sound in a turbulent region as a quadrupole (Howe (2003)).

Definitions of the total radiated sound arise from exact solutions in integral form. The ratio between both sound radiating sources is

$$\frac{\Pi_q}{\Pi_d} \propto \frac{V_0}{\ell_0} \frac{\ell_0}{A} M^2 \quad (2.36)$$

Details of the flow determine values of V_0/ℓ_0 and A . However, a rough estimation of the relation can be made regarding pipe flow including an orifice. Consider a pipe of length L , with $\ell_0 = xD$, for $0 < x \leq 1$. This results in

$$\frac{V_0}{\ell_0} \frac{\ell_0}{A} = \frac{\frac{1}{4} \pi D^2 L}{\pi D L} = \frac{x}{4} \quad (2.37)$$

Therefore, sound produced by turbulence near surfaces by dipole is dominant with a factor $\sim M^{-2}$ compared to sound produced by quadrupoles (Curle (1955); Howe (2003); Lighthill (1952); Michalke (1989); Rienstra and Hirschberg (2001)). Besides sound radiation by compact bodies, this also holds for non-compact bodies, as in turbulence interacting with edges and corners (Howe (2003)). Thus, for $M \ll 1$, it is legit to mainly consider dipoles as sound radiating sources in bounded flow situations as investigated in this thesis.

Note that the fundamental frequency at which sound is generated by the two phenomena is different. The fundamental frequency of the dipole is half of the fundamental frequency of a quadrupole. When looking at the turbulent stresses, quadrupole are proportional to the inertial term (fluctuations in velocity squared). The dipole is only proportional to the fluctuating velocity (Curle (1955)).

2.7 Exact solution to Curle's analogy

An exact solution to Curle's analogy could give insight in the relation between the force exerted on the fluid and the generated noise field. A complete derivation of this coupling is given in Appendix A. Using Green's functions for fixed and impermeable surfaces (no monopole source), the exact solution to Curle's analogy results

$$\rho'(x_i, t) = \rho(x_i, t) - \rho_0 = \frac{\partial^2}{\partial x_i \partial x_j} \iiint_V \left[\frac{T_{ij}}{4\pi c_0^2 |x_i - y_i|} \right] dV - \frac{\partial}{\partial x_i} \iint_{\partial V} \left[\frac{p m_i}{4\pi c_0^2 |x_i - y_i|} \right] dS \quad (2.38)$$

Under the assumption that dipole sources are dominant over quadrupole sources and that the flow velocity is low, a more usable expression results given as (Atassi (2020))

$$\rho'(x_i, t) c_0^2 = \left[\frac{\partial F_i(\tau)}{\partial \tau} + \frac{F_i(\tau) c_0}{|x_i - y_i|} \right]_{\tau} \frac{\cos(\theta)}{4\pi |x_i - y_i| c_0} \quad (2.39)$$

Note that in between brackets both a long and short distance term are present respectively. The term outside the brackets defines the shape of the field, as seen in Figure 2.5.

2.8 Experimental research

The governing equations of fluid are non-linear making it difficult to accurately predict the sound production of fluid flows (Hirschberg (2007)). Because of this, an experimental approach is a promising way of investigating acoustic noise in pipes induced by orifices. This, however, is only possible for the direct effects by the source term. The source term itself is hard to measure.

Agarwal (1994b) measured pressure fluctuations close and far from sources. In both regions, the content of power spectra are found to be much higher than those for undisturbed flow. As far downstream the flow statistics have returned to their undisturbed state, there the increased content is attributed to propagating acoustic waves. These modes induced by the orifices are attenuating when moving away from the disturbing source (Agarwal (1994a)). Qing et al. (2006) measured the pressure fluctuations in the turbulent region and concluded that orifices significantly disturb pipe flow locally. These are typically hydrodynamic rather than acoustic. The intensity of pressure fluctuations is seen to increase with mass flow rate. Additionally, the energy content at lower frequencies is seen to decrease moving from the orifice. Spazzini et al. (2001) studied flow behavior over a backward-facing step and concluded that low frequency fluctuations are related to a flapping motion. High frequency fluctuations correspond to vortex formation and shedding at the step. This behavior might be equal in flow through orifices. Anantharaman (2014) has indicated low frequency flapping motions of single-hole orifice jets being sustained by the large recirculation zones. He concluded this to happen at Strouhal number of approximately 0.02 based on the hole velocity and the difference in internal diameters of the pipe and orifice. Measured and computed normalized whistling frequencies of single-hole orifices are found to be $St \approx 0.2-0.4$ based on the hole velocity and orifice thickness (Lacombe, Moussou and Aurégan (2011); Moussou, Testud, Hirschberg et al. (2007); Testud, Aurégan, Moussou and Hirschberg (2009)). Assuming that vortex shedding is dominating the whistling phenomenon, this high frequency fluctuating component is contributed to that.

At the location where the flow reattaches to the pipe wall, which is varying in time (Bull and Agarwal (1983)), the wall pressure fluctuations are highest according to Tao et al. (2017). At that wall location

p_{rms} -values are even higher than on the orifice surface. Additionally, Tao et al. (2017) found that on the orifice plate, the highest surface pressure fluctuations are located at the inner upstream corner. Heenan and Morrison (1998) have studied a backward-facing step as well. They concluded that the peak p_{rms} -values can be attenuated using a permeable surfaces at the location of reattachment.

Last, some effort is put in the scaling of pressure measurements to estimate fluctuating force behavior. Moussou (2006) scaled wall pressure measurement data in a water pipe subjected to an orifice. As a function of frequency, the force spectrum is scaled as $\Phi_{FF} \propto f^{-3.2}$. Scaling laws are important in the characterisation of the source term. Measuring the fluctuating forces will namely remain a difficult task as non intrusive accelerometers have to be applied at the orifice plate. This is not possible in the current test setup of ASML.

2.9 Computational Fluid Dynamics studies

Supercomputing power has been growing exponentially which makes doing CFD affordable (Pope (2004)). However, despite the enormous growth in computing power, Direct Numerical Simulations (DNS) still remain out of reach for practical usage. Additionally, DNS may not be needed to get solutions for engineering purposes (Chaouat (2017)). Regarding the flapping motion and the vortex shedding being the dominant phenomena in the sound generation process, it is assumed that only resolving for larger scales is sufficient (Pope (2004)), hence LES is sufficiently accurate for the work done in this thesis. LES is namely able to resolve large scales of motion and being a transient solver. Along with DNS and LES solving the transient problem, time-averaged methods do exist obtaining flow information. A method doing so is Reynolds-Averaged Navier-Stokes (RANS) which averages the Navier-Stokes equations. This method is not suitable for studying acoustics, but nonetheless can give useful insights in flow behavior and will therefore also be applied in this thesis. With an unsteady version of RANS, transient solutions can be obtained, referred to as URANS. But, in the URANS approach turbulent fluctuations of flow quantities are not resolved. Therefore URANS is neither suitable for this study. A hybrid RANS-LES is also possible, but requires very specific turbulence specification at the boundaries (Dhamankar, Blaisdell and Lyrintzis (2018)).

In DNS and LES, methods do exist to compute or resolve the acoustics directly. Direct Noise Computation is one of those but is computationally expensive and sensitive to errors (Alenius (2012)). For example Lacombe et al. (2010) already have used LES acoustics to simulate the whistling ability of an orifice plate. Rütten, Meinke and Schröder (2001) have performed LES of 90° pipe bends and found pressure fluctuations at Strouhal numbers in the same range as measured values. Piellard and Bailly (2010) have tried a two-step approach to determine aeroacoustics in ducted diaphragm flow. This required the addition of an acoustic mesh for interpolation with an acoustic theory. Results did show important differences in terms of acoustic levels. See the work of Alenius (2012) for a full literature review on using LES to directly or indirectly capture the sound field. To summarize; in compressible simulations care must be taken that phase errors by dispersion might lead to errors in the sound cancellation. Additionally, solutions are sensitive to boundary conditions. Solving incompressible flow is also an option. According to Wagner et al. (2007): ‘An additional assumption, commonly used, is that feedback from the acoustic field to the source is negligible. Hence, we can calculate the source term from a numerical simulation that ignores any acoustic wave propagation and subsequently predict the sound production outside the flow. In extreme cases of low-Mach-number flow, a locally incompressible flow simulation of the source region can be used to predict the (essentially compressible!) sound field.’

Because of the above, incompressible LES is found sufficient for the goal of this thesis. Namely, the source term can be captured with this, without the need for an acoustic field description. Since measuring the acoustic field lies within the abilities of ASML, no additional effort is taken to simulate this sound field in ways which require more effort. Note that no pressure fluctuations from the acoustics are expected in incompressible LES. A full description of the principles of LES is given in Chapter 4.

2.10 Conclusions

Review of literature is performed to find answers to the research questions which have to be answered before simulations can be started. From all the above, the following conclusions can be drawn

- FIV disturbances arise from the production and dissipation of turbulence kinetic energy. This phenomenon is always present in flow through orifices and is partly responsible for the creation of the pressure drop. In the jet-wake region two mechanisms are found to generate significant noise. These are a low frequency flapping motion, and a higher-frequency unsteady vortex shedding. The first mechanism, which is the stretching of vortices with respect to a body, or the acceleration of fluid on a surface, is thought to generate the most acoustic content. The frequencies that belong to these phenomena are for now estimated to be around 20 to 1500 Hz. Thus; with this the mechanisms that generate acoustic noise are described.
- Two sources are accountable for the generation of acoustic noise content when no mass is injected or leaking. These sources are dipoles and quadrupoles. Dipole noise is arising from a force applied by a body to the fluid and is physically described as a fluctuating reaction force of a body. Quadrupole noise is generated by the turbulence-turbulence interactions, and are physically described as fluctuating stresses in fluids. In the presence of a solid body perpendicular to the flow direction, significant noise is attributed to dipole noise, which is only true when Mach number are lower than one. As of this, the fluctuating force of the body on the fluid is to be investigated in this thesis. All in all; one single source term plays a dominant role in generating the acoustics.
- As for now, simulating the source term using incompressible LES is regarded as a promising method. Associated accuracy and computational costs are still under investigation. It is chosen not to capture any form of acoustic information with the simulation either simulation directly or using a theory to calculate. So; LES is promising, but the accuracy and applicability have yet to be investigated.

Chapter 3

Review of Experimental Data

In line with previous experimental studies, see Section 2.8, at ASML significant amount of experimental studies are performed to understand acoustic noise and subsequently design to prevent for this. Studies are performed by Remco van de Meerendonk, Vinod Anantharaman, and Rens Liebrand (ASML (2020)). Additionally, experiments are performed by Shravan Kottapalli at the TU/e (Kottapalli (2020)). All studies mainly focus on wall pressure fluctuations in non-disturbed straight water pipes and water pipes with an orifice. An often applied single-hole orifice in machines of ASML is the SS20 which has an area ratio of 20%. In pipes and hoses of standard diameter, $D_p = 9$ mm, these orifices have a hole diameter of $D_h = 4$ mm. Mainly short and sharp orifices are applied having a thickness ratio of $t_h/D_h = 0.5$ where t_h is the hole thickness. A schematic of this part is given in Figure 4.3.

Both the hydrodynamic and acoustic noise are of interest and therefore the experimental data obtained by colleagues is reviewed, analyzed and post processed. The hydrodynamic wall pressure fluctuations in straight pipes as well as wall pressure fluctuations in the jet-wake region are essentially important to compare the LES results with. Acoustic noise measurements give insight in the nature of the pressure fluctuations far up- and downstream of the source. Note that the experimental data sets can be requested (ASML (2020)).

3.1 Experimental setup

Pressure fluctuations are measured with pressure transducers. An experimental setup is created previously explained in the work of Anantharaman (2014). This setup is used at ASML and TU/e to measure hydrodynamic wall pressure fluctuations in the jet-wake region and to measure acoustic wall pressure fluctuations in the far field. In this experimental setup the SS20 orifice plate can be included. At ASML the water cabinet used in actual machines is applied to drive flow. At the TU/e a significantly smaller pump is applied.

Measurements are performed using water at a constant temperature of 22 °C. At this temperature, the dynamic viscosity is $\mu = 9.532 \times 10^{-4}$ Pa s and the density is $\rho = 998$ kg/m³. In this thesis the flow disturbances are studied at a bulk Reynolds number of $Re = 10000$ expressed as

$$Re = \frac{\rho U_b D_p}{\mu} \quad (3.1)$$

In here U_b is the bulk velocity. This Reynolds number is marginally in the turbulent regime and is close to the Reynolds number of most performed experiments. Additionally, being in the lower Re range results in relatively large turbulent structures. This is computationally beneficial when performing LES. The corresponding bulk velocity is calculated to be $U_b = 1.06$ m/s. Small deviations in Re can be scaled for. Specifications of performed experiments are given in Table 3.1.

Table 3.1: Specifications of the experiments performed at ASML and TU/e.

Type	Restriction	Location	Re	U_b [m/s]	Frequency [Hz]	Pump
Straight pipe	-	-	10657	1.18	0 - 12800	No
Orifice (ASML)	SS20	-2,1,2,3,6,10D	11022	1.17	0 - 800	Yes
Orifice (TU/e)	SS20	-2,1,2,3,6D	10000	1.06	0 - 45000	Yes
Orifice	SS20	$\approx 21D$	10489	1.11	0 - 12800	Yes

3.2 Post processing

Post processing of previously reviewed experimental data is required. To study acoustics, the mean is always subtracted from signals first. The resulting pressure fluctuations in time are studied regarding the content as a function of frequency. This is done estimating power spectral densities (PSD) using Welch's method Welch (1967). A PSD gives information about a signal's power as a function of frequency. This helps to understand which mechanisms generate noise because the frequency can be related to a geometry and flow characteristics. A power spectral density of a variable ϕ is given as $\Phi_{\phi\phi}$. A non-dimensionalized PSD is denoted by $\Phi_{\phi\phi}^*$. The frequency can be non-dimensionalized by

$$St = \frac{fD_p}{U_b} \quad (3.2)$$

Signals are divided into eight segments with an overlap of fifty percent. Segments are windowed using a Hamming window. After computing the Fourier spectrum, segments are averaged to generate the PSD. Note that the area under the PSD is not affected by the amount of segments or degree of overlapping. However, details can lack when for example too many segments are used. From a PSD, the root mean square value of the particular signal is determined as done by Qing et al. (2006). For the pressure this is

$$p_{rms} = \sqrt{\int_{-\infty}^{\infty} \Phi_{pp}(f) df} \quad (3.3)$$

With this, the fluctuating behavior of a specific frequency range can be considered. Especially, as content at very low frequencies is produced by system behavior rather than the disturbance source itself, this can result in more fair comparison of flow behavior. The frequency range of interest for this work is 10Hz to 3000Hz. The integral values are determined with the trapezoidal function in MATLAB.

The wall shear stress can be determined with

$$\tau_w = \frac{1}{2} \rho U_b^2 C_f \quad (3.4)$$

Blasius (1913) provided an empirical formulation to calculate the required skin friction coefficient for fully developed straight pipe flow as

$$f_f = \frac{0.316}{Re^{\frac{1}{4}}}, \quad C_f = \frac{f_f}{4} \quad (3.5)$$

3.3 Straight pipe measurement data

In straight pipes, wall pressure fluctuations are rather low. So to study these fluctuations, it is important to disregard any additional disturbance sources by the system. Van de Meerendonk (ASML (2020)) has studied pipe wall pressure fluctuations using potential energy to drive the flow. With a water reservoir at height, additional disturbances of the pumps are therefore excluded. Despite different Reynolds numbers, non-dimensionalizing PSD's does lead to a similar PSD according to W. Blake (1984). He showed this existing merge of non-dimensionalized PSD's for Reynolds number up to one hundred-thousand. Therefore it is legit to compare wall pressure fluctuations of simulated straight pipe flow using LES with this experimental data set. In Figure 3.1a PSDs of pipe wall fluctuations in an empty pipe are depicted for different Reynolds number. Note that the normal form is plotted as the null case cannot be non-dimensionalized. A significant content is measured at the lower and higher frequency range without the motion of flow ($Re = 0$). This is regarded as a background error. The PSDs at close Reynolds numbers do coincide.

However, p_{rms} -values of wall pressure do decrease significantly as a function of decreasing Reynolds number found by van de Meerendonk. This is in line with the straight pipe wall pressure measurements done by Selvam, Öngüner, Peixinho, Zanoun and Egbers (2018).

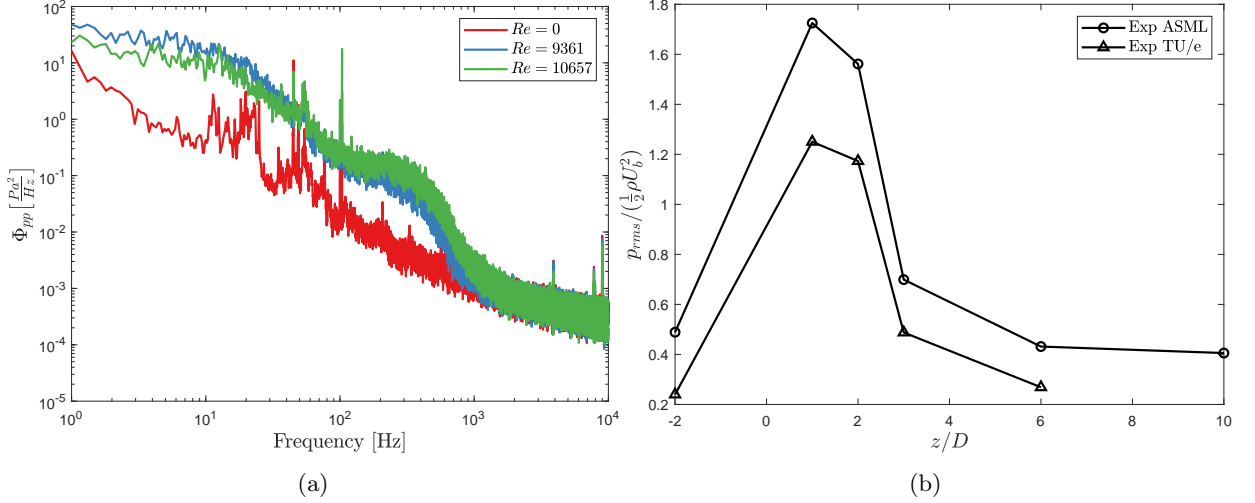


Figure 3.1: a: PSD of hydrodynamic wall pressure fluctuations in a straight pipe for different Reynolds number. b: Comparison of hydrodynamic wall pressure fluctuations measured at ASML normalized with the hydrodynamic pressure q . The orifice is located at $z/D = 0$.

3.4 Hydrodynamic pressure fluctuation measurement data

The hydrodynamic noise in water pipes including an orifice is measured by Anantharaman and Kottapalli (ASML (2020)). Results are non-dimensionalized with the hydrodynamic pressure $q = \frac{1}{2} \rho U_b^2$ to compare with results at different mass flow rates. Unfortunately Anantharaman only considered a frequency up to 800 Hz, which is rather low. Kottapalli considered a frequency up to 45000 Hz and measured with a bulk velocity equal to the bulk velocity used in this thesis. In Figure 3.1b the normalized wall pressure fluctuations are depicted with the orifice located at $z/D = 0$. The highest pressure fluctuations are measured to occur close to the orifice. Around $z/D = 6$ the acoustic pressure fluctuations become dominant. The level of pressure fluctuations reached downstream of the jet-wake region is roughly equal to the p_{rms} upstream of the orifice. The higher pressure fluctuations measured at ASML are attributed to the additional noise generated by the water supply system.

3.5 Acoustic pressure fluctuation measurement data

Rens Liebrand (ASML (2020)) measured acoustic wall pressure fluctuations far up- and downstream of the disturbing component using the available test setup. Details are added to Table 3.1. This experimental data allows investigation of the net effect of the noise source as pressure transducers are located out of the hydrodynamic region. Pressure transducers are placed $\approx 21D$ up- and downstream of the orifice. Regarding Figure 2.5b, a theoretical dipole radiates pressure waves up- and downstream which are perfectly out of phase. To study the power content introduced by the dipole, both signals should be added or subtracted, after which the PSD is calculated. If both signals are perfectly out of phase at every frequency, the signals are expected to cancel out when adding them in time domain first. In contrast, for a theoretical pure dipole the energy content is expected to increase when both signals are subtracted in time domain first. Corresponding PSDs after both adding and subtracting the signals in time domain first are illustrated in Figure 3.2. The PSDs are post processed to remove peaks at frequencies of a multiple of 50 Hz resulting from poor grounding. Figure 3.2a illustrates that indeed power content is increased when subtracting the signals in the time domain. This is the case for a frequency range of roughly 10 to 2000 Hz. In Figure 3.2b the decrease of power content is depicted for a frequency range of roughly 10 to 2000 Hz when adding both the signals in time domain. This presumably indicates that in that range the dipole effects are strong

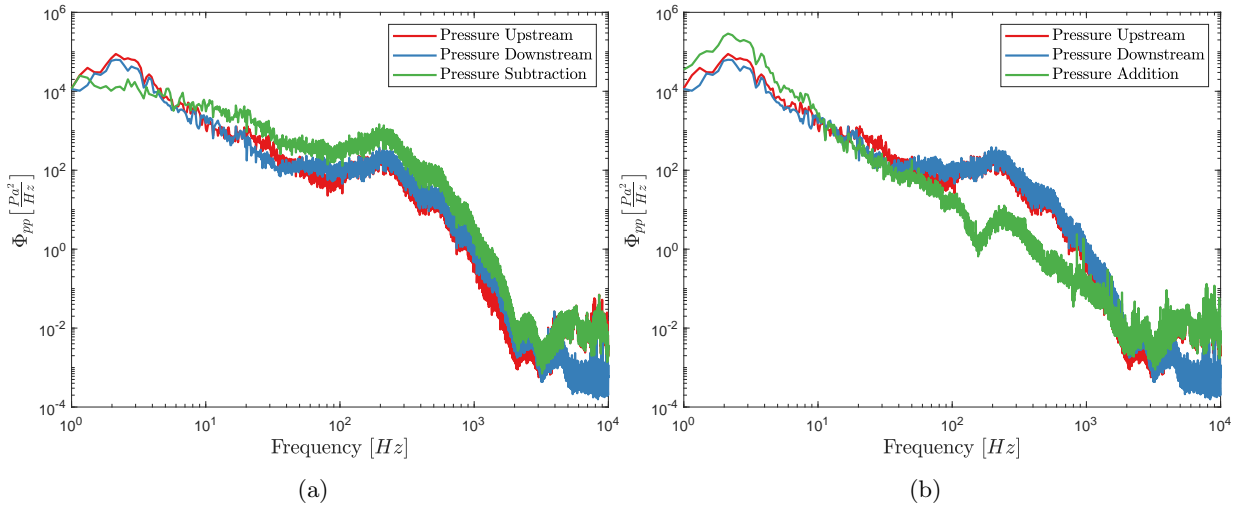


Figure 3.2: PSD of wall pressure fluctuations far up- and downstream of the orifice. a: Supplemented with a PSD of subtracted time signals. b: Supplemented with a PSD of added time signals.

compared to other source types. In the lower frequency range the opposite behavior is visible. Addition of the signals results in an increase in content, whereas subtraction results in a decrease. This might indicate the in-phase noise contribution of the pump.

Now the contribution of the dipole source term to the pressure spectrum is known, the actual source term is computed using the exact solution to Curle's analogy, given in Equation 2.39. The discretization used for this is elaborated on in Appendix A. Figure 3.3a illustrates the resulting PSD of the force signal. Comparing with the pressure spectrum, it is noticed that a significant force is required to generate pressure fluctuations $21D$ up- or downstream. Using the exact analogy and taking the integral of the force spectra, the required F_{rms} to generate the pressure spectrum is calculated as a function of distance between source and observer. This is depicted in Figure 3.3b.

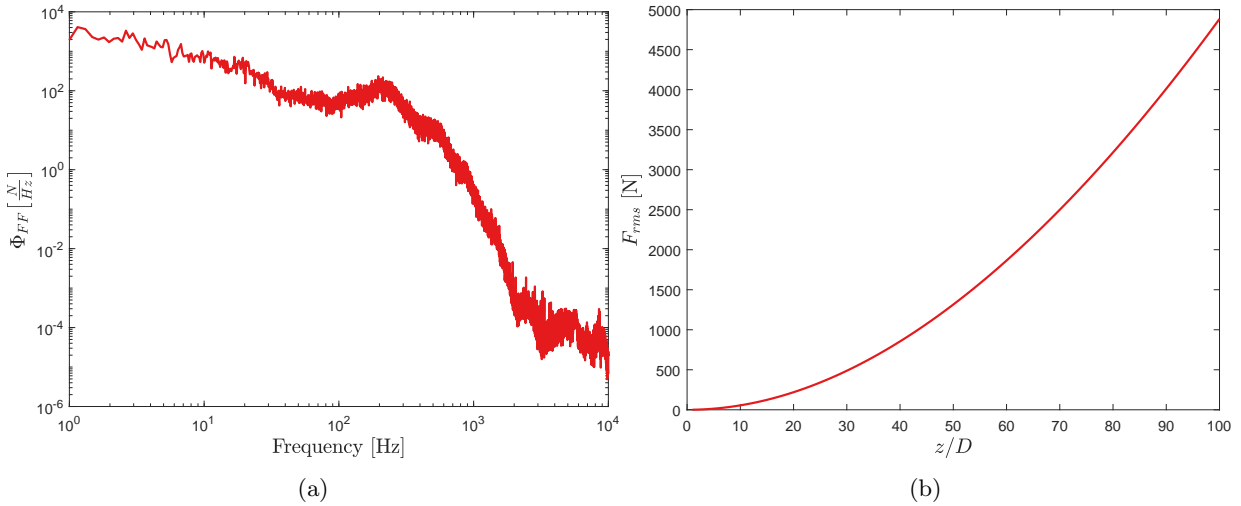


Figure 3.3: a: PSD of the force resulting from the exact solution to Curle's analogy. b: Root mean square of the force required to generate subtraction graphs in Figure 3.2a as a function of the distance between source and observer.

A significant increase in the required force is observed. The exponential decay is physical, but in bounded flow the pressure content is not expected to decrease that significantly with the distance, see for example Figure 22 of Agarwal (1994b). In other words, the calculated F_{rms} -values are significantly above the expected value. One hypothesis why large force fluctuations are required to generate the acoustic pressure

fluctuations is that free field sound propagation is considered. If this is the case, bounds might need to be incorporated to get solutions in the right order. Walls namely do increase the pressure at the source and lead to scattering, the problem becomes non-compact, and the source term is lacking acoustical information (Schram (2009); Schram, Anthoine and Hirschberg (2005)).

3.6 Turbulent pipe LDV measurement data

LES will be performed in the same Reynolds number range as in the presented experiments. To analyse LES results, reference data is required. Either experimental or DNS data are suitable for that. Den Toonder and Nieuwstadt (1997) have carried out Laser Doppler Velocimetry measurements of pipe flow at a Reynolds number of $Re = 10000$. Based on pressure drop measurements, they provided the friction velocity defined as

$$u_\tau = \sqrt{\frac{\tau_w}{\rho}} \quad (3.6)$$

With the density and bulk velocity given, the friction coefficient is calculated to be $C_f = 8 \times 10^{-3}$ using Equation 3.4. Using Equation 3.5, the skin friction coefficient is calculated to be $C_f = 7.9 \times 10^{-3}$ which agrees well with the experimentally obtained value by Den Toonder and Nieuwstadt (1997). For a flow with $Re = 10000$ and $U_b = 1.06$ m/s, the corresponding wall shear stress is calculated to be $\tau_w = 4.44$ Pa using Equation 3.4.

Flow statistics of axial and radial components have been measured by them, lacking the tangential component. Therefore the TKE cannot be computed, especially as pipe flow is highly anisotropic. Therefore the experimental data is compared with a DNS set of El Khoury et al. (2013) at $Re = 11700$, see Figure 3.4. The distance from the wall is normalized as

$$y^+ = \frac{y\nu}{u_\tau} \quad (3.7)$$

The wall distance is defined as $(0.5 - r/D)^+$ as the origin of the coordinate system is in the middle of the geometry. Note that the shear stress component $u_r'u_z'$ is flipped in sign for illustration reasons. Additionally, note that in Cartesian coordinates this stress component is negative in one of the half-heights in xz -plane as will be shown later. Because of circumferential symmetry, $u_t'u_z'$ and $u_r'u_t'$ are zero (Pope (2001)). The normalized velocity profiles do match well, see Figure 3.4a, as well as the stress components of fluid, see Figure 3.4b. Therefore it is assumed that flow at $Re = 10000$ can also be compared with the DNS data of El Khoury et al. (2013).

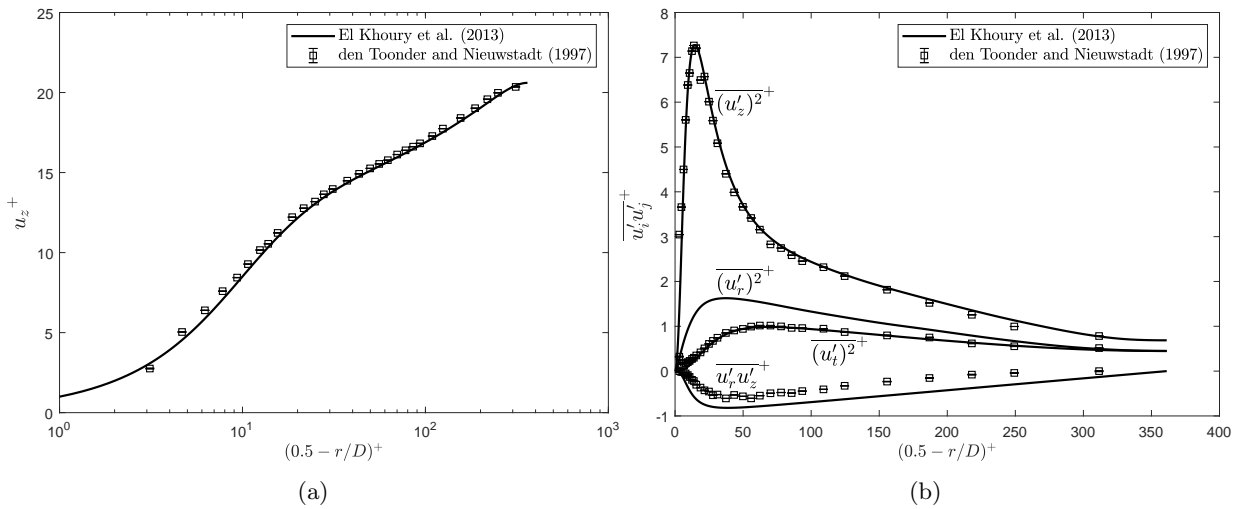


Figure 3.4: Comparison of the flow statistics of DNS data by El Khoury et al. (2013) ($Re = 11700$) and experimental data by Den Toonder and Nieuwstadt (1997) ($Re = 10000$). The experimental measurement error is included. a: The axial velocity normalized with the friction velocity. b: The turbulent stress components in fluid normalized with the friction velocity squared.

Chapter 4

Numerical Approach

As already mentioned in Section 2.9, LES is a promising method to obtain transient data of flow characteristics for engineering purposes. In this chapter the numerical approach of LES will be elaborated on. Information about the numerical solver will be provided, as well as a description of the mesh and setup conditions. The chapter will be concluded with a summary of the main simulation settings of all simulations done. In Appendix B a manual for setting up a simulation is provided. Additionally, steps in this numerical approach regarding RANS simulations are provided in Appendix C.

4.1 Large Eddy Simulation

To resolve all turbulent length and time scales, the computational mesh must be able to represent the whole range of turbulent structures; from the large energy-containing scales all the way to the smallest dissipative scales, see Equations 2.9 and 2.10 and Figure 2.2. This is done in DNS and requires an enormous amount of computational effort. Despite its accuracy, this method remains out of scope for all engineering approaches (Chaouat (2017)). Especially, if the quantities of interest and the rate-controlling processes are determined by the resolved large scales, which may be expected (Pope (2004)).

In LES, only the larger turbulent scales are resolved for, see Figure 2.2b. This means that influences of the smaller scales are not taken into account directly. To account for that, a so-called subgrid-scale (SGS) model is included for modelling these smaller scales. This SGS model is of huge importance to bridge the gap between the large energy-containing eddies ℓ_0 and the dissipative scales η ensuring that the correct amount of TKE is dissipated from the bulk flow, see Figure 2.2a. It is justified to account for the smaller scales using a SGS model as the smaller scales are universal at sufficiently high Reynolds numbers according to the first similarity hypothesis of Kolmogorov (1941). At the Taylor microscale, viscosity significantly starts affecting the dynamical behavior of turbulent eddies, and TKE starts to be dissipated into heat, see Figure 2.2b. For scale resolving simulations to provide good results, Addad, Gaitonde, Laurence and Rolfo (2008) have shown that the maximal local grid size, Δ , has to be limited by the turbulent scale at which the dissipation region begins. Therefore, the resolved to under resolved scales boundary should lie in the inertial subrange. Thus, in practice the boundary should be chosen at least lower than the Taylor microscale. Note that when a grid is significantly refined LES tends to DNS (Speziale (1998)). Ideally, the grid is refined until a grid-independent LES is obtained. From that point on, the philosophy of LES loses its meaning for further grid refinement. Because of that, it should be bared in mind that a grid refinement study is very important so dependency of simulation results on the computational grid can be investigated.

LES distinguishes between unresolved and resolved scales by spatial filtering. Unresolved scales are characterized by a residual field

$$\check{\phi}(x_i, t) = \phi(x_i, t) - \tilde{\phi}(x_i, t) \quad (4.1)$$

Each variable ϕ solved for is thus decomposed into a filtered value $\tilde{\phi}(x_i, t)$ and a sub-filtered value $\check{\phi}(x_i, t)$ as

$$\phi(x_i, t) = \tilde{\phi}(x_i, t) + \check{\phi}(x_i, t) \quad (4.2)$$

Typically ϕ represents velocity components or pressure. Filtered values will be resolved on grids with a filter width, Δ , equal to the grid spacing, h , in case of numerical LES (Pope (2004)). The filter width is defined as

$$\Delta = (\Delta_x \Delta_y \Delta_z)^{1/3} \quad (4.3)$$

Applying a filter to the incompressible mass and momentum conservation equation, see Equations 2.1 and 2.3, results in the to be resolved part of the solution

$$\frac{\partial \tilde{u}_i}{\partial x_i} = 0 \quad (4.4)$$

$$\frac{\partial \tilde{u}_i}{\partial t} + \frac{\partial (\tilde{u}_i \tilde{u}_j)}{\partial x_j} = -\frac{1}{\rho} \frac{\partial \tilde{p}}{\partial x_i} + \frac{\partial}{\partial x_j} \left[\nu \left(\frac{\partial \tilde{u}_i}{\partial x_j} + \frac{\partial \tilde{u}_j}{\partial x_i} \right) - \tau_{ij}^{SGS} \right] + \frac{F_i}{\rho} \quad (4.5)$$

Note that an additional term is introduced, τ_{ij}^{SGS} , which is the residual-stress tensor or SGS tensor defined by

$$\tau_{ij}^{SGS} = \widetilde{u_i u_j} - \tilde{u}_i \tilde{u}_j \quad (4.6)$$

This term is added because the product $\tilde{u}_i \tilde{u}_j$ could not be directly filtered as it appears in Equation 4.5. Additionally, as is the case for RANS, also in LES the filtered nonlinear convection term would be a major difficulty and must be modelled.

4.1.1 SGS model

In STAR-CCM+ the Wall-Adapting Local-Eddy Viscosity (WALE) SGS model by Nicoud and Ducros (1999) provides the subgrid scale turbulent viscosity, ν_T , required for modelling of the SGS stress tensor. The advantages of this method over for example the Dynamic Smagorinsky SGS is its applicability near walls, its relative time efficiency, and its functioning without any form of near-wall damping. In STAR-CCM+ the eddy viscosity modelling for subgrid stresses is done by using

$$\tau_{ij}^{SGS} - \frac{1}{3} \tau_{kk}^{SGS} \delta_{ij} = -2\nu_T \tilde{S}_{ij} \quad (4.7)$$

with the filtered rate-of-strain tensor given by

$$\tilde{S}_{ij} = \frac{1}{2} \left(\frac{\partial \tilde{u}_i}{\partial x_j} + \frac{\partial \tilde{u}_j}{\partial x_i} \right) \quad (4.8)$$

Note that on the left only the deviatoric stress is left after subtracting the hydrostatic stress since this is the only relevant part for incompressible flow. The turbulent viscosity is provided as

$$\nu_T = \Delta^2 S_w \quad (4.9)$$

Where S_w is the deformation parameter defined as (

$$S_w = \frac{(S_{ij}^d S_{ij}^d)^{3/2}}{(S_{ij}^d S_{ij}^d)^{5/4} + (S_{ij} S_{ij})^{5/2}} \quad (4.10)$$

It is a strain rate tensor and consists of velocity gradients from the resolved velocity field. Here S_{ij}^d is defined as (STAR-CCM+, 2018, p. 7038)

$$S_{ij}^d = \frac{1}{2} \left[\left(\frac{\partial \bar{u}_i}{\partial x_j} \right)^2 + \left(\frac{\partial \bar{u}_j}{\partial x_i} \right)^2 \right] - \frac{1}{3} \delta_{ij} \left(\frac{\partial \bar{u}_k}{\partial x_k} \right)^2 \quad (4.11)$$

The length scale Δ , or filter width, is defined in terms of the cell volume V_c as

$$\Delta = C_w V_c^{1/3} \quad (4.12)$$

C_w is a model constant having a default value of $C_w = 0.544$, which works for homogeneous isotropic turbulence as bounded flow. Substituting all into the filtered Navier-Stokes equations results in the LES equations

$$\frac{\partial \tilde{u}_i}{\partial t} + \tilde{u}_j \frac{\partial \tilde{u}_i}{\partial x_j} = -\frac{1}{\rho} \frac{\partial \tilde{p}}{\partial x_i} + \frac{\partial}{\partial x_j} \left[(\nu + \nu_T) \left(\frac{\partial \tilde{u}_i}{\partial x_j} + \frac{\partial \tilde{u}_j}{\partial x_i} \right) \right] + \frac{F_i}{\rho} \quad (4.13)$$

Now an additional term is present which dumps eddy viscosity in the domain to represent subgrid scale stresses.

4.1.2 Implicit LES

If the truncation error in the finite volume scheme is more or less a dissipation-like term, non-physical numerical dissipation will occur. Especially on coarse grids, this effect might be significant. In essence it has the same effect as the explicit SGS model dissipating energy from the field. Relying on the numerics can provide some subgrid scale closure (Adams and Hickel (2009)) called implicit LES (ILES). So when disabling SGS models, still the right amount of energy dissipation might be achieved by information leakage due to numerical dissipation. This is legit as the leading-order truncation term of conventional SGS models is similar in form and magnitude to the truncation term introduced by most numerical schemes (Fernandez, Nguyen, Roca and Peraire (2016); Fureby and Grinstein (1999)). This method is practically applied in STAR-CCM+ by changing the model constant C_w in Equation 4.12 to a reasonable low value resulting in an insignificant modelled turbulent viscosity and therefore SGS stresses.

4.2 Solver

In STAR-CCM+, the Finite Volume Method (FVM) is applied, being successful in solving fluid flow problems. FVM is based on conserving the conservation laws over the surfaces of cells around nodes in a mesh. A solvable system of algebraic equations is obtained by discretizing the governing equations in space and time (STAR-CCM+, 2018, p. 6934). Integrating the convection-diffusion equation over a control volume V and applying Gauss's divergence theorem results in

$$\frac{d}{dt} \int_V \rho \phi dV + \int_A \rho u_i \phi dA = \int_A \mu \frac{\partial \phi}{\partial x_i} dA + \int_V S_\phi dV \quad (4.14)$$

where ϕ represents a scalar property to be transported and S_ϕ expresses the generation or destruction of fluid property ϕ . It consist of a transient term, a convective flux, a diffusive flux, and a source term.

4.2.1 Segregated flow solver

The segregated flow solver solves the integral conservation equations of mass and momentum in a sequential manner for solution variables u_i and p (STAR-CCM+, 2018, p. 6947). In here, a pressure-velocity coupling algorithm corrects the pressure to satisfy the continuity equation with the sought velocity field. In this predictor-corrector approach, the pressure results therefore from this pressure-correction equation.

4.2.2 Convection discretization scheme

Convection fluxes over cell faces can be discretized using different schemes. Along with LES, the Bounded Central-Differencing scheme is suitable (STAR-CCM+, 2018, p. 3152), being a combination of a central-differencing (second-order accurate) scheme and an upwinding scheme (first- or second-order accurate). Namely, pure upwinding is very robust but rather inaccurate, whereas central differencing provides accurate solutions but is not very robust (Van der Weide (2018)). Pure first order upwinding causes turbulent kinetic energy to decay unnaturally fast especially on coarse computational grids, referred to as artificial dissipation. Second-order upwinding is characterized by dispersive errors and smear solutions less compared to first-order upwinding and increases accuracy. The different errors are returning in the residual plots as the first-order upwinding schemes results monotonically decreasing residuals whereas this is not the case for second-order upwinding schemes. So the approach in which fluid property ϕ_f at the face is determined effects stability and accuracy of numerical schemes. In Figure 4.1a three cells are depicted with nodal values of ϕ at upwind, central and downwind locations. To come up with a convection boundedness criterion, normalized values are introduced being

$$\xi_f = \frac{\phi_f - \phi_U}{\phi_D - \phi_U}, \quad \text{and} \quad \xi_C = \frac{\phi_C - \phi_U}{\phi_D - \phi_U} \quad (4.15)$$

To avoid non-physical oscillations in the solution, ϕ_C and thus ϕ_f have to be locally bounded between ϕ_U and ϕ_D . Therefore no non-physical oscillations are present if

$$\phi_U \leq \phi_C \leq \phi_D, \quad \text{or} \quad \phi_D \leq \phi_C \leq \phi_U \quad (4.16)$$

This boundedness is summarized in the Normalized Variable Diagram (NVD) plotting ξ_f as a function of ξ_C . Conditions for boundedness are

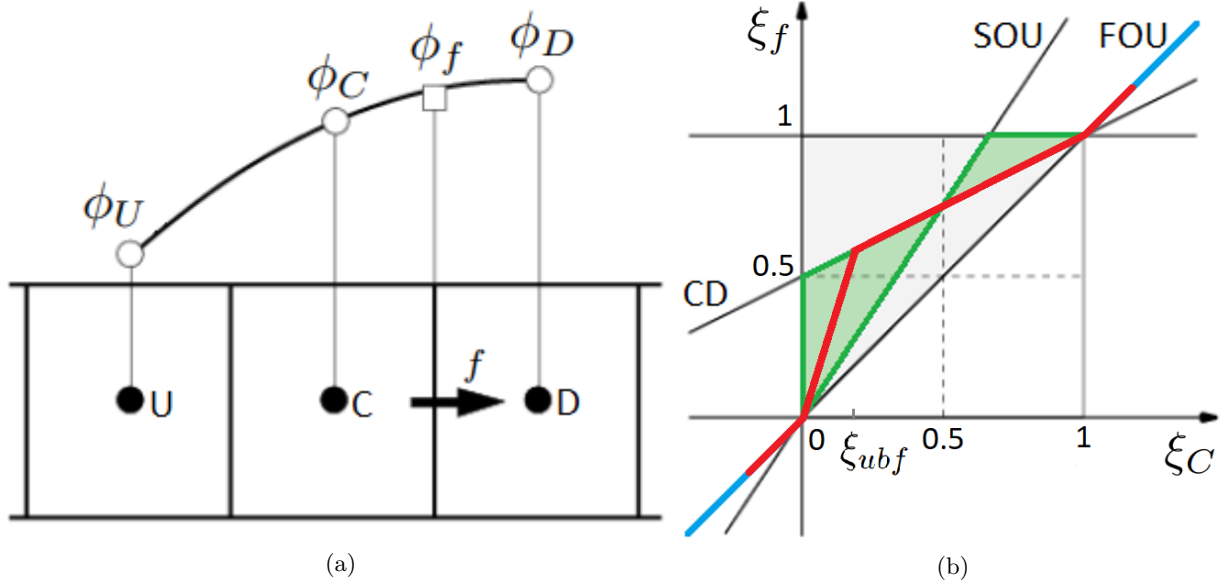


Figure 4.1: FVM convection discretization a: Stencil for interpolating cell face values from known cell-center values.

- For $0 \leq \xi_C \leq 0$, $\xi_f > \xi_C$ which means that the bounded region is above the line $\xi_f = \xi_C$. Additionally, in that region ξ_f should be below one.
- For $\xi_C < 0$ and $\xi_C > 1$, ξ_f is equal to ξ_C .

Convective fluxes are computed with Bounded Central-Differencing for the fluid property at the face, ϕ_f , as

$$(\dot{m}\phi)_f = \begin{cases} \dot{m} \phi_{FOU}, & \text{for } \xi_C < 0 \text{ or } \xi_C > 1 \\ \dot{m} (\sigma \phi_{CD} + (1 - \sigma) \phi_{SOU}), & \text{for } 0 \leq \xi_C \leq 1 \end{cases} \quad (4.17)$$

When $\xi_C < 0$ or $\xi_C > 1$ the face value is determined by a first-order upwinding (FOU) scheme to maintain boundedness. ξ_f then follows the blue line in the NVD, see Figure 4.1b. Depending on the stream direction, the interpolated value ϕ_f is the upwind value and is only first order accurate. For $0 \leq \xi_C \leq 1$, a second order accurate scheme is applied. In here, σ , is introduced which satisfies $\sigma(0) = 0$, and $\sigma(\xi) = 1$ for $\xi_C \geq \xi_{ubf}$, with σ being smooth and monotone. This means that when $\xi_C \geq \xi_{ubf}$, pure central differencing (CD) is applied. If this criterion is not met, a combination of Second-Order Upwinding (SOU) and CD is applied. ξ_{ubf} is the Upwind Blending Factor (UBF). When this value is chosen low, this results in more central differencing, see Equation 4.17. CD provides accuracy, whereas SOU provides robustness. With ξ_{ubf} the proportion of both can thus be tuned. The second order accuracy is achieved in the green part of the NVD, see Figure 4.1b. A STAR-CCM+ default value of $\xi_{ubf} = 0.15$ is considered conservative but is said to reflect optimization for accuracy and performance (STAR-CCM+, 2018, p. 3159). Assuming that the slope of $\sigma(\xi_C)$ is constant and using bounded central differencing, $\xi_f(\xi_C)$ follows the red line, see Figure 4.1b. Note that for $\xi_{ubf} < 0.15$ another line might be followed. Linearity is preserved so the solver does not switch from one scheme to another. This means that ϕ_f is determined with upstream and downstream cell values that are determined with the same scheme and therefore no first order truncation error is introduced (Waterson and Deconinck (2007)). When assuming uniform cells, this linearity should be preserved around $\xi_C = 0.5$. This is not the case using e.g. a minmod scheme when choosing $\xi_{ubf} = 0.5$, which leads a lot of numerical diffusion.

4.2.3 Temporal discretization

The transient term in the transport equation is discretized using an implicit scheme. This requires the subdivision of time in time-steps and uses the solution at the current time step. The major advantage of the implicit method over the explicit method is its stability, helpful when applying large timesteps. A disadvantage is its computational expensiveness as an iterative (or matrix) solver has to be used as the new value appears at both sides of the equation (Van der Weide (2018)). The transient term is approximated

using a second-order temporal implicit differencing scheme at the current time step n as

$$\frac{d}{dt}(\rho\phi V) = \frac{3(\rho\phi V)^n - 4(\rho\phi V)^{n-1} + (\rho\phi V)^{n-2}}{2\Delta t} + \mathcal{O}((\Delta t)^2) \quad (4.18)$$

This uses only two previous solutions. However, when the solution at more previous timesteps are included, the leading-order truncation order can be reduced. When using five time levels the second order truncation error is decreased with a factor 2.64. The use of time levels thus enhances accuracy, but the scheme is harder to stabilize (STAR-CCM+, 2018, p.2892).

4.2.4 Accuracy LES

Having introduced the possible error sources in LES, it is of importance to check the accuracy of the simulations. An approach judging the accuracy of LES on Δ is introducing turbulent statistic Q which has contributions from both the energy-containing and dissipative eddies as done by Pope (2004). Q^m is an estimate to Q defined as

$$Q^m = Q^w + Q^r \quad (4.19)$$

where Q^w comes from the resolved field and Q^r denotes its residual contribution, and its dependency on Δ is depicted in Figure 4.2.

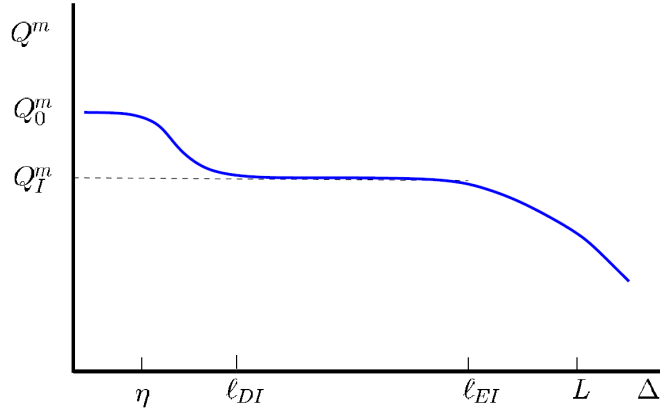


Figure 4.2: Turbulent statistic Q as a function of the filter width Δ (Pope (2004)).

At Q_0^m DNS accuracy is reached and Q_I^m represents an intermediate asymptote indicating that Δ is in the inertial subrange and most of the energy contribution is resolved for. Note again that when $\Delta < \ell_{DI}$, LES loses its meaning. This emphasizes again the need for a grid refinement study. The grid dependency can be studied for a second order statistic of interest, namely comparing the resolved and modelled TKE. It is good practice to monitor modeled TKE on rather coarse grids according to (STAR-CCM+, 2018, p. 3702) and Pope (2004) using

$$M_{TKE} = \frac{k_{SGS}}{k_{SGS} + k_{res}} \quad (4.20)$$

In Appendix B it is described how to enable the field function k_{SGS} in STAR-CCM+. M denotes the fraction of turbulent kinetic energy in the resolved motions. A value of one corresponds to RANS and a value of zero corresponds to DNS. It is recommended to resolve at least 80% of the large scales ($M_{TKE} \leq 0.2$). Additionally, to quantify the contribution of the SGS model, checking the turbulent viscosity is a good measure. With respect to laminar viscosity, the dynamic turbulent viscosity ratio is given as

$$TVR = \frac{\mu_\tau}{\mu} \quad (4.21)$$

A turbulent viscosity ratio of 10 is considered an acceptable value.

4.3 Computational domain

In LES, it is important that the flow reaches its fully developed state possible on the computational grid when approaching the orifice. Fully developed turbulence means that the statistics of the flow properties indicate invariant behavior in the axial direction downstream a reference location. A geometry with an upstream length of twenty diameters and a downstream length of ten diameters from the orifice is created. The same orifice is implemented as done in experiments, See Chapter 3. Pipe and hole diameter are $D_p = 9$ mm and $D_h = 4$ mm which result in an area ratio of 20%. The thickness of the orifice is $t_h/D_h = 0.5$. The origin of the cylindrical coordinate system is located in the very middle of the orifice. For the computational domain see Figure 4.3.

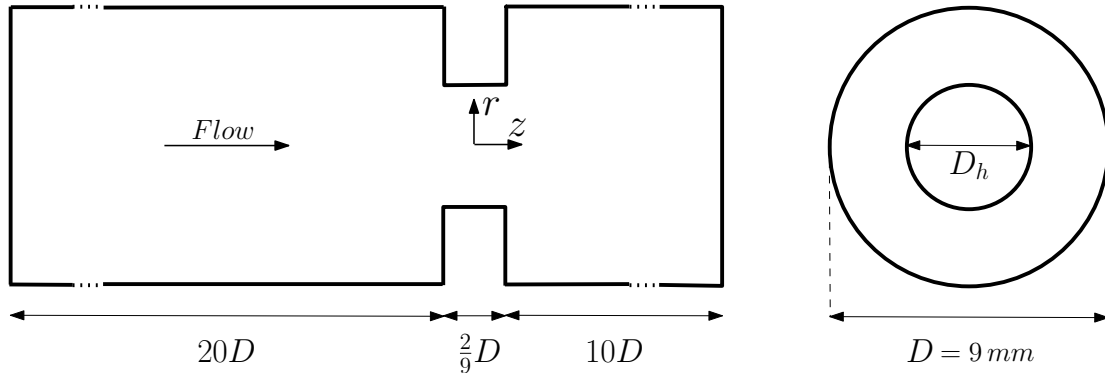


Figure 4.3: Schematic of computational domain used in LES with dimensions.

4.4 Mesh

Meshing the domain is an important part in numerically solving fluid flow. The mesh quality is strongly related to the accuracy of the solution as already discussed. Besides the influence of the filter width itself, a few general rules regarding cell quality should be followed to get accurate simulation results, see Figure 4.4. These are

- Having cell aspect ratios ideally around one in regions with homogeneous flow statistics. Larger gradients are expected close to boundaries. Using prism layers in those regions, the cell aspect ratio is of less importance. The function of prism layers (PL) is explained later on.
- Guaranteeing the skewness angle to be below 90.0° to prevent non-physical solutions (STAR-CCM+, 2018, p. 6941). The skewness angle is the angle between the line connecting two cell centroids and the face normal, see Figure 4.4a.
- Providing smooth changes of cell volume of adjacent cells, see Figure 4.4b.
- Achieving a face validity, also orthogonality, of minimal 1.0. This is a measure of the face normal correctness relative to their attached cell centroid, see Figure 4.4c. For very bad cells these face normals might cross.

These rules are checked running a full mesh diagnostics report. A visualization of these cell criteria is given in Figure The overall mesh quality is judged by checking

- The cell density in either high- or low-gradient areas.
- The correctness of meshing near walls.
- Effect of grid refinement on convergence and flow statistics.

The bulk region is meshed using polyhedral cells. Polyhedral (14 cell faces) cells are favorable over tetrahedral cells having more neighbouring cells and therefore better approximate gradients. Besides, these are less sensitive to stretching. Last, turbulent flows are chaotic and not unidirectional. This means that the possibility of meeting orthogonality requirements is higher enhancing the reduction of numerical diffusion. This is especially important in recirculating internal flows (StevePortal (2019e)).

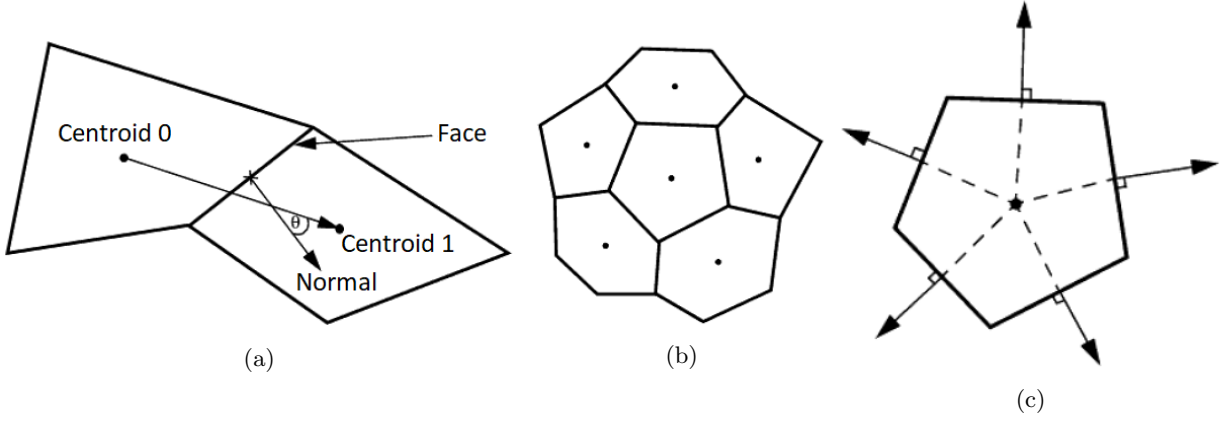


Figure 4.4: Visualization of good computational cells STAR-CCM+ (2018). a: Skewness angle. b: Volume change. c: Face validity.

Cell sizes in the bulk region are based on the Taylor microscale at the pipe centerline modelled with RANS, see Appendix C. Namely, a filter width Δ , and thus maximal cell size, equal to this viscous-driven scale provides good results (Addad et al. (2008)). In Figure C.3 length scales up- and downstream of the orifice are given. Upstream of the orifice, which is essentially a straight pipe, a cell size of 0.5 mm should be sufficient for accurately resolving flow with LES. However, note that in the jet region the Taylor microscale is approximately 0.2 mm, see Figure C.3. Therefore the cell size should not be based on the Taylor microscale in the pipe region. Besides, note that cell sizes are defined as a function of the volume of cells, V_c , as (STAR-CCM+, 2018, p. 2478)

$$Mesh \ size \approx 1.2V_c^{\frac{1}{3}} \quad (4.22)$$

4.4.1 Near-wall treatment

Near the wall a boundary layer exists characterized by high gradients in the direction perpendicular to the wall. Therefore a different mesh type will be applied. Prism layers are able to capture these high gradients. This cell type allows high aspect-ratios without affecting the stream-wise resolution. To simulate molecular shear effects correctly, the prism layer should have a thickness of at least fifty wall units. In that region direct effects of molecular viscosity are non negligible according to Pope (2001). In the outer layer ($y^+ > 50$), direct effects of molecular viscosity on the mean flow velocity are negligible as turbulent shear stress dominates and therefore no prism layers have to be applied there. The corresponding thickness will be determined using Equation 3.7 which defines y^+ . A wall shear stress of $\tau_w = 4.44$ Pa is used for this as calculated in Chapter 3.6.

Near-wall regions in turbulent flows are treated in mainly two ways; either resolving (WRLES) or modelling (WMLES) turbulent structures. WRLES requires $y_1^+ < 1$. FVM stores information at cell centers. This means that the distance between the cell centroid of the first prism layer to the wall should be smaller than one wall unit. WMLES requires $1 < y_1^+ < 5$ or $y_1^+ > 30$. With WMLES it is not desired to have an intermediate resolution which ends up in the buffer layer (Salim and Cheah (2009)), see Figure 4.5. In the end WRLES comes with a higher grid resolution close to the wall which increases the computational costs. Especially for high Reynolds number flows because the number of grid cells to resolve the boundary layer over for example a flat plate increases as $Re^{1.76}$ (Chapman (1979); Pope (2001)). STAR-CCM+ automatically chooses the method of near-wall treatment based on the designed mesh when using the All- y^+ Wall Treatment model. In Figure 4.5 the velocity profile near the wall is depicted. When WMLES is applied, the viscous sublayer and logarithmic layer can be modelled respectively as

$$u_{lam}^+ = y^+, \quad \text{and} \quad u_T^+ = \frac{1}{K} \ln E' y^+ \quad (4.23)$$

In here, K is the Von Kármán constant equal to 0.42 as default, and E' is the wall function coefficient which is dependent on roughness function f_r as $E' = E_r/f_r$. f_r is unity for smooth walls. As default $E_r = 9.0$. For the buffer layer inside STAR-CCM+ a blended wall law is applied.

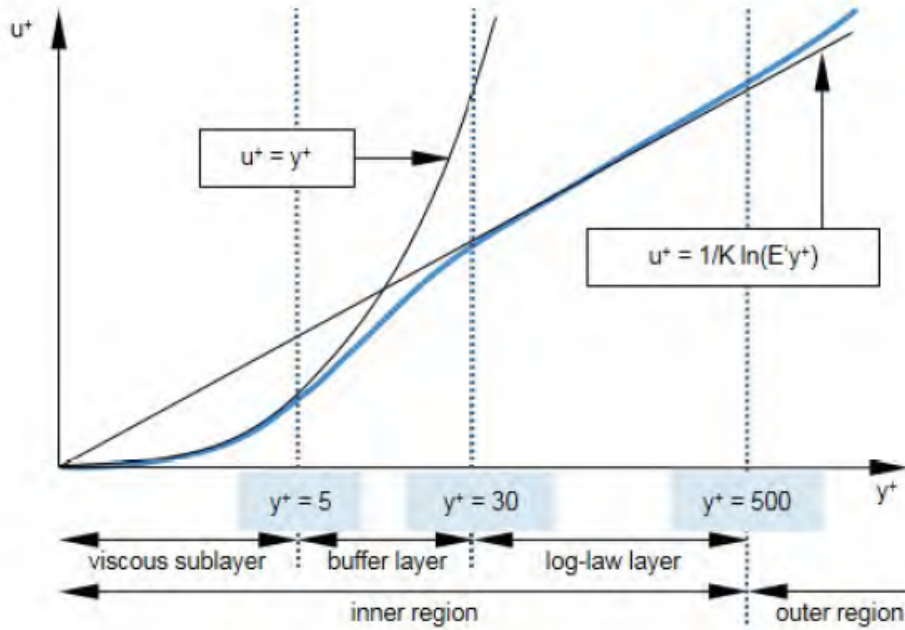


Figure 4.5: Modelling of the wall layer (STAR-CCM+, 2018, p. 3733).

4.4.2 Meshing the pipe region

When simulating a pipe with an orifice still the part upstream of the orifice can be seen as a simple straight pipe. Bad meshes near walls effect the accuracy of the characterization of flow separation and the determination forces on walls. This affects integral results as for example the pressure drop. Therefore meshing near the wall is important. Clear criteria are set up to do so

1. For WRLES: $y_1^+ < 1$. For WMLES $1 < y_1^+ < 5$ or $y_1^+ > 30$.
2. The stretching factor (SF) of adjacent cells in cross stream direction should be below 1.5 to guarantee smoothness ($SF \leq 1.5$).
3. At least ten prism layer cells in cross stream direction ($N_p \geq 10$) for wall resolved simulations (STAR-CCM+, 2018, p. 2379) (depending on Reynolds number). For modelling the inner region at least two to three cells are required (StevePortal (2019b)).
4. The total prism layer thickness, δ_p , should be at least fifty wall units ($\delta_p^+ > 50$).

The total prism layer thickness, the number of prism layer cells in cross stream direction, and stretching factor are mesh generation input variables in STAR-CCM+. Because of a linear increase in prism cell thickness in cross stream direction, y_1^+ can be calculated from these variables. The total prism layer thickness, δ , is related to the thickness of the first prism layer, δ_1 , as

$$\delta_p = \delta_{p1} \sum_{i=0}^{N_p-1} (SF^i) \quad (4.24)$$

Note that $y_1^+ = \frac{1}{2}\delta_{p1}^+$. The distance of the first prism layer cell centroid to the wall can be determined as

$$y_1^+ = \frac{1}{2} \frac{\delta_p^+}{\sum_{i=0}^{N_p-1} (SF^i)} \quad (4.25)$$

With this expression, the stretching factor, the number of prism layers and the total prism layer thickness are parameters to control y_1^+ . Please note that additionally the stretching factor between the prism layers and polyhedral cells should also be small. i.e. a smooth transition from prism layer to bulk region should be provided. So having relatively large cells in the bulk region, requires a thick adjacent prism layer, $\delta_{p,last}$.

Controversially, this is achieved choosing large stretching factors. Therefore a balance between y_1^+ , SF, N_p , and $\delta_{p,last}$ needs to be found.

Using a wall shear stress of $\tau_w = 4.44$ Pa, for both applying WRLES and WMLES, mesh properties are given in Table 4.1. Cross sections of the computational grid are depicted in Figure D.1. Note that WMLES with $y_1^+ > 30$ is not included as no mesh can be created with the proposed criteria while simultaneously guaranteeing smoothness between the prism layer and bulk region. According to Equation 4.22, the mesh size will differ from the cell base size. In a simulation, this cell size is determined following the steps in Appendix B.7.1. The standard deviation and actual cell size are included in Table 4.1.

Table 4.1: Properties of the proposed computational grids for LES.

	Grid 1	Grid 2	Grid 3	Grid 4	Grid 5	Grid 6	Grid 7	Grid 8
Base size [mm]	0.70	0.50	0.50	0.35	0.35	0.35	0.35	0.20
Cell size [mm]	0.86	0.63	0.63	0.43	0.42	0.41	0.42	0.27
Cell size std [mm]	0.118	0.073	0.082	0.059	0.050	0.049	0.066	0.030
No. cells	207k	483k	889k	1882k	610k	1069k	815k	3442k
N_p	10	12	25	25	5	12	8	10
δ_p [mm]	0.70	0.70	0.70	0.70	1.00	1.00	1.00	0.70
δ_p^+	49	49	49	49	70	70	70	49
SF	1.5	1.5	1.3	1.3	1.2	1.2	1.5	1.1
y_1^+	0.22	0.10	0.04	0.04	4.70	0.84	0.71	1.54
$\delta_{p,last}$ [mm]	0.24	0.24	0.16	0.16	0.28	0.19	0.35	0.10
Cell size _{last} [mm]	0.57	0.45	0.40	0.32	0.36	0.32	0.40	0.19
Layer Mesher	PLM	PLM	PLM	PLM	PLM	ALM	ALM	ALM
No. extrusion cells	-	-	-	-	80	80	80	80

4.4.3 Meshing the orifice region

The rules introduced for the straight pipe do also apply for the region around the orifice. However, the orifice region has to be treated separately to guarantee a good mesh. Around the orifice namely the wall shear stress is typically higher requiring a thinner prism layer to the wall to meet the y_1^+ -criterion. However, the problem is that the wall shear stress is significantly different on every location of each orifice surface. The total prism layer thickness is determined from the lowest wall shear stress, ensuring that the boundary layer is always covered with prism layers ($y^+ \geq 50$). Note that this may result in high values of δ^+ for locations where the wall shear stress is high. The value of y_1^+ , on the other hand, is determined based on the highest wall shear stress.

Remaining input parameters are SF and N_p . These parameters are used to tune the values of y_1^+ and δ_{last} . Note that it is intentionally chosen not to decrease the cell size around the orifice to avoid a jump in cell sizes! Since the cell sizes are determined based on the pipe region (computationally less expensive), the cell sizes do not match the decrease in δ_p around the orifice because of the higher wall shear stresses. Therefore, it is often hard to ensure that $\delta_{p,last}$ matches the cell sizes of the bulk region while simultaneously meeting the other mesh criteria based on a higher wall shear stress. For a large $\delta_{p,last}$ the stretching factor has to be chosen high whereas the number of prism layers has to be kept low. The latter comes with an increase of y_1^+ .

For grids 6 to 8 the number of prism layer cells is decreased to decrease the total number of cells so the computational time decreases. To guarantee $y_1^+ < 5$ for wall shear stresses up to at least $\tau_w = 1000$ Pa, the total prism layer thickness is decreased.

Around edges, the prism layer mesher model decreases the total prism layer thickness and number of prism layer cells. The mesher does that to avoid generating highly skewed cells. However, this results in bad prism layers, see Figure 4.6a. This is solved by applying the advancing layer mesher which creates more uniform cell layers and helps to reduce cell skewness, see Figure 4.6b. The cell quality remediation model is additionally enabled which tracks highly skewed cells. This model treats these tracked cells differently enhancing stability. Cross sections of meshes around the orifice are illustrated in Figure D.1.

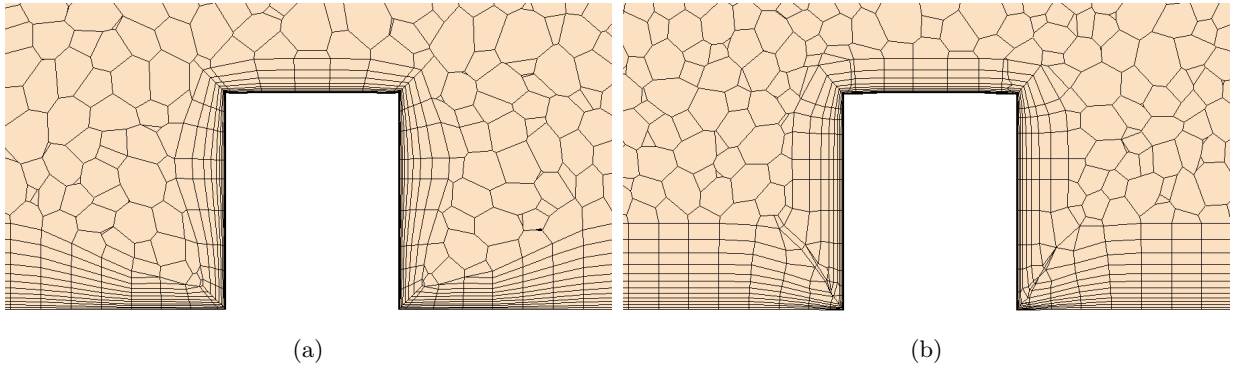


Figure 4.6: Mesh grid around orifice using different near wall layer meshing methods. a: Prism layer mesher. b: Advancing layer mesher.

4.5 Setup conditions

With the meshes being prepared, the setup conditions have to be provided. This involves the choice of a proper timestep, specification of boundary conditions, and the initialization of the solution.

4.5.1 Time stepping

Temporal resolution is additionally important influencing the accuracy of results. For explicitly discretized flow solvers, the Courant-Friedrichs-Lewy (CFL) condition by Courant, Friedrichs and Lewy (1928) is a condition saying that any travelling length of information during one timestep has to be smaller than the distance between two mesh element centroids. Using implicit discretization as in STARCCM, the CFL number is no longer a critical measure of stability. However, it still serves as a measure of accuracy when the truncation error of space and time are of the same order. If the timestep is taken too large, the fluid crosses one or more cells in that time step. The convective CFL number is given as

$$CFL = \frac{u_i \Delta t}{\Delta x_i} \quad (4.26)$$

This convective Courant number should be close to 1.0 in the region of interest (STAR-CCM+, 2018, p. 3703). Besides the CFL number, the turbulent time scale is important as discussed in Section C.4. Another practical aspect is the highest frequency interested in. According to Nyquist's theorem, the sampling frequency should be at least twice as high as the frequency determining the bandwidth. In the book of Wagner et al. (2007) a more conservative recommendation is suggested calculating the frequency as one tenth of the inverse of the time step. An maximal frequency of 5000 Hz is looked for. This results in a time step of $\Delta t = 2 \times 10^{-5}$ s.

In precursor RANS analysis, the smallest turbulent times scales are found to be $t_\ell \approx 1 \times 10^{-4}$ s in the orifice region. This corresponds with instantaneous values of the turbulent time scale in LES. In RANS the smallest time scale is modelled to be $t_\eta = 1 \times 10^{-5}$ s. For calculating the CFL number, defining the maximum jet velocity is possible using conservation of mass ($U_b A_p = u_h A_h$). This results in $u_h = 5.37$ m/s, but this is averaged over the area and averaged in time. With RANS, a modelled maximum velocity of $u_h = 7.33$ m/s is obtained. This value represents the maximum in the jet, but is time averaged as well. A maximal instantaneous velocity magnitude in the jet-wake region in LES is assumed to be $u_h = 10$ m/s. With the proposed grids, theoretically the maximal CFL number will be 1.25 using a time step of $\Delta t = 2.5 \times 10^{-5}$ s. This time step results in an acceptable maximal CFL, the possibility to represent the Kolmogorov time scale almost everywhere, and meets the maximal frequency criterion. One should keep in mind that not every cell has an information travelling length equal to the general cell size and therefore the CFL can be larger for single cells. This is deemed acceptable for the used implicit time integration scheme.

4.5.2 Boundary conditions

Applying realistic turbulent inflow conditions at the inlet boundary is found important by Dhamankar, Blaisdell and Lyrintzis (2017). Optimally, a fully-developed state is achieved right at the inlet by feeding in realistic turbulent structures, as applying plug flow conditions requires longer development lengths. Doing so, three methods for generating turbulence at the inlet are investigated. These are the synthetic eddy method (SEM), applying periodic boundary conditions, and using a recycling based method.

Synthetic eddy method

Generating turbulence synthetically is nowadays a well embraced technique reaching a fully developed state as it does not require data libraries or parallel simulations (Dhamankar et al. (2017)). But, this technique fail when non-correlated structures are generated. This results in too much energy dissipation and leads to laminarization (Aider, Danet and Lesieur (2007)). This happens because the energy is not evenly distributed over the energy spectrum.

In the SEM spatially and temporally correlated unsteady fluctuations are generated and superimposed on an inlet mean velocity field (Jarrin, Benhamadouche, Laurence and Prosser (2006)). In STAR-CCM+ this method is applied giving in fields of velocity and turbulent intensity at the inlet. However, as eddies must span at least two cells to produce correlated signals ($\ell_0 > 2\Delta$), the minimum mesh-spacing imposes a limit on this turbulence scale (STAR-CCM+, 2018, p. 3723). Allowing synthetic turbulence to develop to real turbulence, a sufficient distance should be left to the region of interest. Spurious pressure oscillations introduced by mass flow fluctuations at the boundary using the SEM are reduced by enabling the 'Mass Flow Scaling' option. SEM applied to the geometry is illustrated in Figure 4.7a. Precursor simulations can provide the required input information. The turbulent intensity (TI) is defined as

$$I \equiv \frac{u'}{U_b} = \frac{\sqrt{\frac{2}{3}k}}{U_b} \quad (4.27)$$

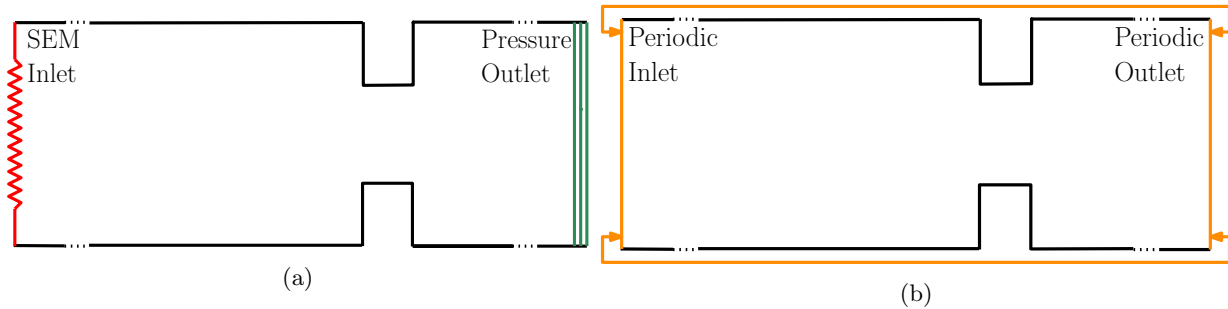


Figure 4.7: a: Boundary conditions using the synthetic eddy method. b: Boundary conditions applying periodic boundary conditions.

Periodic boundary conditions

A second method to provide correlated turbulent structures at the inlet is using periodic boundary conditions. This is used when the geometry of interest and expected flow pattern are of a periodically repeating nature. An example is fully developed pipe flow. By only simulating a short section of the geometry the fully developed behavior is obtained by copying the flow characteristics from the master to slave boundary plane. Using translational periodicity, enough length should be provided so that the largest coherent structures in the turbulent flow can still exist. Applying this type of boundary conditions to a geometry with orifice is presented in Figure 4.7b. Note that when not enough length is provided for the turbulent flow to return to fully developed pipe flow, either upstream or downstream of the orifice, in essence orifices are put in series. To drive the flow, either a mass flow rate or pressure drop in axial direction is to be set.

Recycling method

The problem of putting orifices in series can be solved using a recycling plane method (RPM). A velocity field from a downstream location is re-introduced at the inlet (Dhamankar et al. (2017)). In STAR-CCM+ this can be applied by mapping flow characteristics from a short periodic pipe to the inlet of the geometry of interest, so two simulations are running in parallel. The velocity vector field is mapped from the periodic outlet to geometry inlet, see Figure 4.8a. This method can be applied to every kind of geometry.

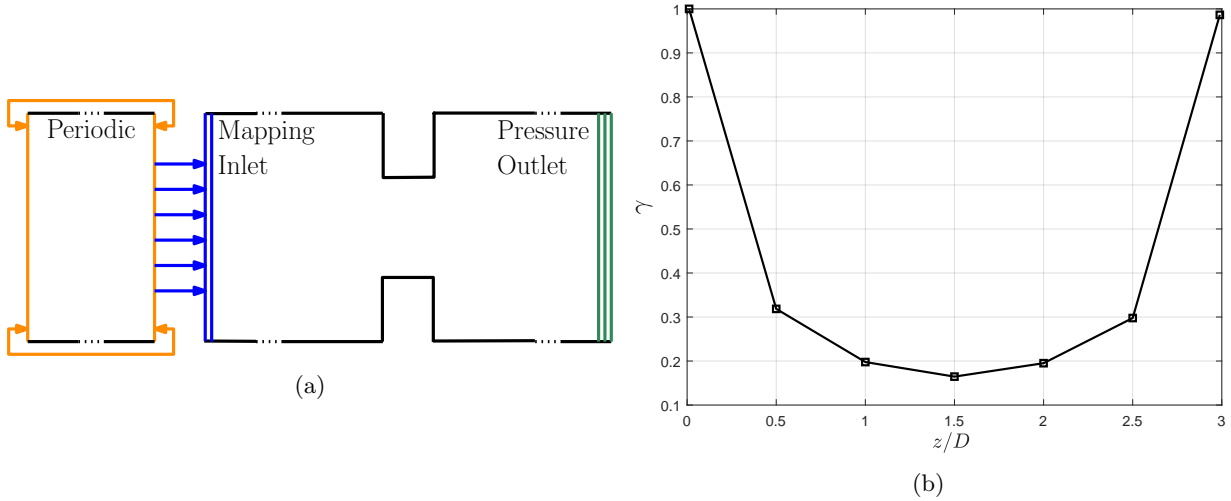


Figure 4.8: a: Boundary conditions using the recycling plane method. b: Cross correlation of the axial velocity in the periodic pipe.

Prescribing the periodic pipe mass flow rate is indirectly specifying the bulk velocity. Prescribing the pressure drop specifies the wall shear stress. It is assumed that specifying mass flow rate is the easiest. First of all, when considering a pipe with orifice, the pressure drop by the orifice has to be known accurately upfront to guarantee the right wall shear stress. Secondly, the right mass flow rate specification is preferred because this is expected to be a dominant factor in the determination of the source term. The mass flow rate is calculated as

$$\dot{m} = \rho A_p U_b \quad (4.28)$$

At the inlet and outlet of the periodic region flow properties are highly correlated. This results in a normalized two-point cross correlation of one. This correlation is defined as

$$\gamma_{ij}(r_i) = \frac{\overline{u'_i(x_i)u'_j(x_i + r_i)}}{(\overline{u'^2_i u'^2_j})^{1/2}} \quad (4.29)$$

r is the shift of the signal probe location. Turbulent structures can develop when the two-point cross correlation coefficient between the boundary and half of the pipe length is zero. This is essential because the large structures are found to be important for generating turbulence at boundaries by Keating, Piomelli, Balaras and Kaltenbach (2004). They have seen a faster transition using turbulent data from a separate solution compared to using the SEM. In Figure 4.8b, the cross correlation coefficient of the axial-velocity component at different locations is depicted for the finest considered computational grid. The reference signal is at $z/D = 0$. The cross correlation with itself is obviously one. In the middle of the pipe, the cross correlation is reaching its final value, i.e. γ will not decrease any further. Therefore, a periodic pipe length of $3D$ is sufficient and will be applied in upcoming simulations.

A description of how to implement the recycling plane method in a simulation is elaborated on in Appendix B.3. The mesh has to be extruded from the inlet. Proposed grids 1 and 4 have a mesh equal to that of the geometry. With the extrusion method it is also possible to create polyhedral cells with are aligned with the flow (StevePortal (2019c)). This reduces numerical diffusion (StevePortal (2019a)). This is applied in grid 5 to 8. The number of extruded layers is determined by dividing the extruded length by the cell base size. Those values are listed in Table 4.1. Note that by mistake Grid 8 contains too less extruded layers.

Pressure outlet

For internal flow it is legit to use a pressure outlet ((STAR-CCM+, 2018, p. 2752)). This is applied in the geometries with the SEM and recycling plane method at the inlet. The pressure is set to 0 Pa. However, this value is not important as it does not change the pressure drop from inlet to outlet. When applying a zero pressure outlet, also fluctuations of pressure at the outlet are forced to zero.

4.5.3 Initialization

LES should be initialized with proper fields to reduce the time to eliminate the effects of the initials. When mapping converged field data of a coarser grid onto a finer grid, the larger turbulent scales are retained and the smaller scales can develop quickly. The initial fields are described with velocity and pressure. Initial turbulence is specified using the SEM.

4.5.4 Data extraction

Data sampling is started when the initial effects are eliminated. This usually takes two to five flow-through cycles (STAR-CCM+, 2018, p. 3703). With the chosen mass flow rate, flow recirculates roughly four times per second for a region length of $30D$. The initial effects are removed from solutions when velocity, pressure and TKE are converged in time. This is the case when the mean of flow properties are settling in time. This is depicted in Figure 4.9 for the axial velocity component, TKE, and pressure respectively.

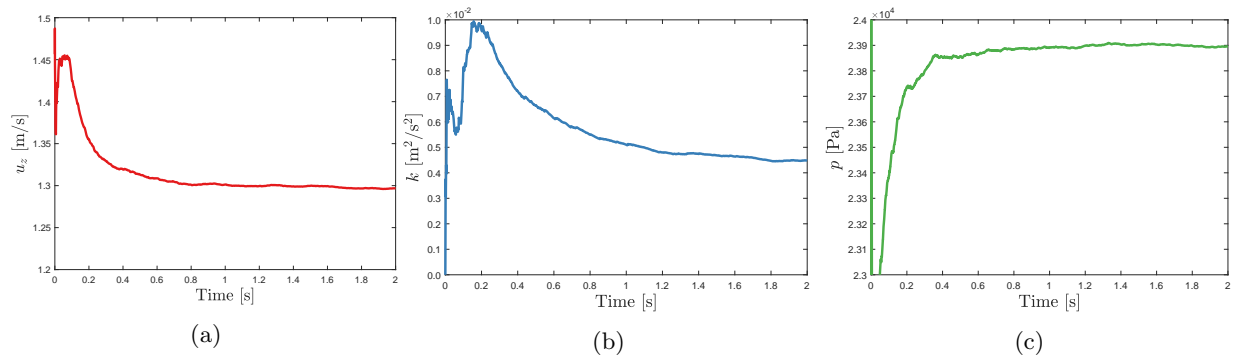


Figure 4.9: a: The mean of the axial velocity as a function of time. b: The TKE as a function of time. c: The mean pressure as a function of time.

The values are probed at the centerline of the pipe at $z/D = -5$. All the variables are settled after one physical second, which corresponds to four flow throughs. Settling of the TKE takes more time because this is a higher order statistic. After converging the data is sampled for another four flow throughs (STAR-CCM+, 2018, p. 3708). In this thesis the main properties of interest are

- Velocity components.
- Turbulent kinetic energy.
- Turbulent shear stresses.
- Wall shear stresses.
- Static pressures.
- Wall pressure fluctuations.
- Forces on the walls.

To plot cross sectional profiles of velocity, TKE and turbulent shear stresses in radial direction, the data is averaged in angular direction at angles $\theta = [0 : 1/8\pi : 2\pi]$. Line probes are created in radial direction for every axial location $z/D = [-20 : 1 : 10]$. The wall shear stresses are sampled with point probes at the same angular and axial locations on the wall. Wall pressure signals are extracted at every axial location $z/D = [-20 : 1/3 : 10]$. The probes are created using JavaScript. The wall force magnitudes are defined

in axial direction and extracted using a report function. From the description it is not clear how this force is computed, but it is expected that this is an integral values of wall pressures over an area.

4.6 Analysis of scalability

Performing LES becomes accessible using high-performance computing (Afzal, Ansari, Faizabadi and Ramis (2017)). Practical LES require a short computational time. It is aimed to perform the LES within a week. The computational time depends on the type and number of processors. The E5 2667 V2 CPU's are found to be the best for the simulations. These nodes consist of 16 processors per node. Preferably the total amount of processors selected is a multiplication of this number. A scalability analysis helps choosing the right amount of processors. Figure 4.10 illustrates the results of a scalability analysis performed on a computational grid of 262k cells. The speed up is expressed as the performance of the number of processors used compared to the performance of 16 processors, see Figure 4.10a. For this coarse grid running LES with a lot of processors leads to a bad performance, see Figure 4.10b. Performing LES on finer grids results in a higher efficiency, see Table 4.1. So when increasing the amount of cells, it is beneficial to increase the amount of processors.

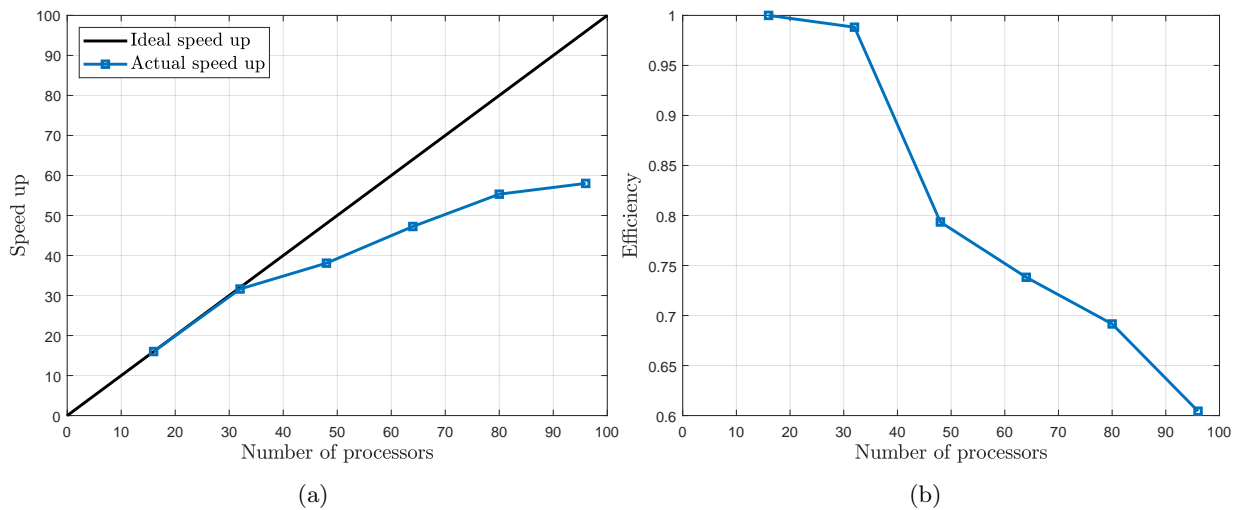


Figure 4.10: Scalability analysis on a computational grid consisting of 262k cells. a: The speed up as a function of the number of processors. b: The efficiency as a function of the number of processors.

Table 4.2: The CPU speed up and the efficiency on a computational grid consisting of 262k cells.

No. processors	Speed up	Efficiency	No. cells/processor
16	16	1.00	16347
32	32	0.99	8173
48	38	0.79	5449
64	47	0.74	4087
80	55	0.69	3269
96	58	0.60	2724

4.7 Residuals

The residuals measure the imbalance of the conservation equations and the degree to which their discretized form is satisfied. Converged solutions are indicated by a minor change of a flow variable from the one iteration to the next iteration. In transient solutions convergence has to be reached every timestep. The amount of inner iterations and the under relaxation factor (URF) are used to control this. URFs do suppress oscillations in the flow that result from numerical errors (Bakker (2002)), see Equation 4.30. On

the other hand, the under relaxation factors do slow down convergence when chosen too conservative.

$$\phi^{new,used} = \phi^{old} + URF (\phi^{new,predicted} - \phi^{old}) \quad (4.30)$$

The URFs are chosen such that smooth converging residuals are obtained. The amount of inner iterations is chosen such that the residuals start to flat at the end of each timestep. For the first simulations the under relaxation factors are 0.7 and 0.3. For the other simulations the under relaxation factors of pressure is increased to 0.7. Respectively 30 and 20 inner iterations are applied. In Figure 4.11 the residuals of LES on grid 1 and grid 8 are depicted. Note that both tend to roughly the same residuals. The residuals of all simulations are listed in Table 4.3.

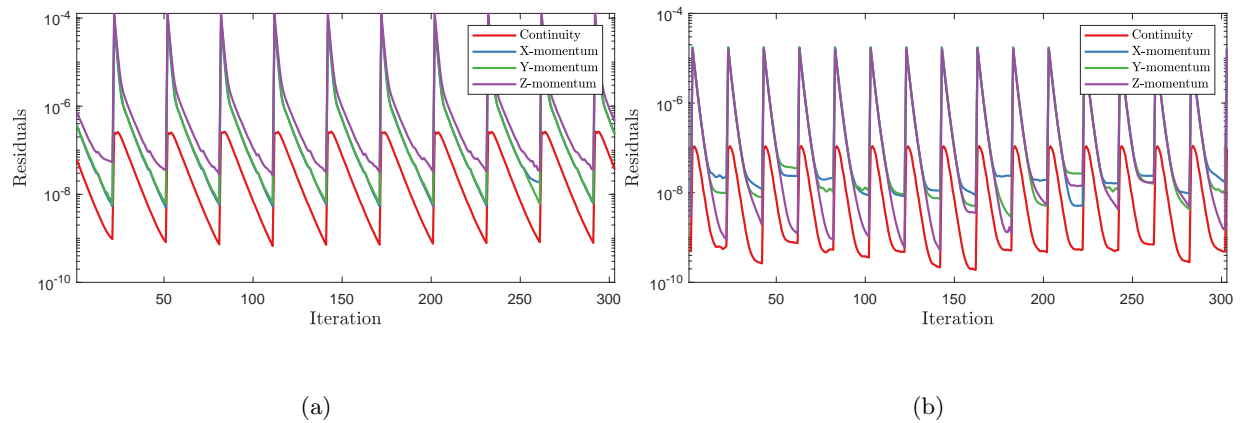


Figure 4.11: a: Residuals of LES on computational grid 1. b: Residuals of LES on computational grid 8.

4.8 Summary of simulation details

In Table 4.3 details of the performed simulations are provided. Upcoming results are based on these simulations.

Table 4.3: Details of the performed simulations.

	Run 1	Run 2	Run 3	Run 4
Grid	Grid 1	Grid 2	Grid 3	Grid 4
Turbulence	RPM	RPM	RPM	RPM
Δt	2.5×10^{-5} s			
Settling time	1 s	1 s	1 s	1 s
Sampling time	1 s	1 s	1 s	1 s
Inner iterations	30	30	20	20
Velocity URF	0.7	0.7	0.7	0.7
Pressure URF	0.3	0.3	0.7	0.7
Residual con	1×10^{-9}	8×10^{-10}	3×10^{-10}	5×10^{-11}
Residual x-mom	1×10^{-8}	8×10^{-9}	5×10^{-9}	4×10^{-9}
Residual y-mom	1×10^{-8}	8×10^{-9}	5×10^{-9}	4×10^{-9}
Residual z-mom	4×10^{-8}	3×10^{-8}	7×10^{-9}	4×10^{-9}
CPU's	96 (16)	96 (16)	96 (16)	96 (16)
CPU time	≈ 17 h	≈ 32 h	≈ 39 h	≈ 77 h
	Run 5	Run 6	Run 7	Run 8
Grid	Grid 5	Grid 6	Grid 7	Grid 8
Turbulence	RPM	RPM	RPM	RPM
Δt	2.5×10^{-5} s			
Settling time	1 s	1 s	1 s	1 s
Sampling time	1 s	1 s	1 s	1 s
Inner iterations	20	20	30	20
Velocity URF	0.7	0.7	0.7	0.7
Pressure URF	0.7	0.7	0.7	0.7
Residual con	8×10^{-11}	3×10^{-11}	2×10^{-11}	2×10^{-10}
Residual x-mom	1×10^{-9}	3×10^{-10}	2×10^{-10}	4×10^{-9}
Residual y-mom	1×10^{-9}	5×10^{-10}	3×10^{-10}	4×10^{-9}
Residual z-mom	1×10^{-9}	3×10^{-10}	4×10^{-10}	3×10^{-9}
CPU's	96 (16)	96 (16)	96 (16)	96 (16)
CPU time	≈ 27 h	≈ 47 h	≈ 54 h	≈ 137 h

Chapter 5

Results of Straight Pipe

In this chapter the LES results of the region upstream of the orifice are presented. The results are divided into two main parts; results based on the application of different boundary conditions and results based on computational grid refinement. These results are required before results of the orifice region can be presented. Cross sectional profiles of flow properties will be discussed, wall shear stress results will be shown, and hydrodynamic pressure fluctuations in straight pipes will be analyzed. Note that some simulations allow to already include an orifice because it does not influence the results upstream of the orifice. Additionally, the application of the different boundary conditions has to be done including the orifice. In the results, the results obtained with LES on computational grid X are shortened as LES X. In the simulation results, the bulk velocity and TKE are calculated respectively as

$$U_b = \frac{\int_0^{2\pi} \int_0^r u_z(r) r dr d\theta}{\pi r^2}, \text{ and } k_b = \frac{\int_0^{2\pi} \int_0^r k(r) r dr d\theta}{\pi r^2} \quad (5.1)$$

5.1 Applied boundary conditions

The different boundary conditions are studied with LES on the coarsest grid (grid 1). The following boundary conditions are applied for that

- Applying the SEM. Velocity input: RANS($k-\epsilon$) mean velocity profile, TI input: based on RANS($k-\epsilon$) TKE profile, TLS of $\ell = 2.0$ mm. See Figure C.2 for RANS($k-\epsilon$) profiles.
- Applying the SEM. Velocity input: RANS($k-\epsilon$) mean velocity profile, TI input: based on RANS($k-\epsilon$) TKE profile, TLS of $\ell = 2.0$ mm. See Figure C.2 for RANS($k-\epsilon$) profiles. Implicit LES.
- Applying the SEM. Velocity input: LES mean velocity profile of periodic pipe on Grid 1, TI input: based on LES mean TKE profile of periodic pipe on Grid 1, TLS of $\ell = 2.0$ mm.
- Applying periodic boundary conditions.
- Applying the recycling plane method.

In here ℓ is based on the criterion $\ell > 2\Delta$. Figure 5.1 depicts the velocity and TKE profiles at $z/D = 2$ normalized with respectively the bulk velocity and bulk velocity squared for the different applied boundary conditions. None of the velocity profiles is perfect. The centerline values are off and the velocity profiles are not steep enough close to the wall. The TKE profiles are not correct as well. Peak values are not simulated appropriately and are shifted from the wall. The wall shear stresses at $z/D = -2$ are respectively 1.43, 1.45, 1.78, 2.10, 2.12 Pa for the different conditions applied. These values are at least 50% off. Lower wall shear stresses indicate a thicker boundary layer. This explains the shallow velocity profiles close to the wall and the shifted peak TKE location from the wall compared to the DNS.

The different methods result in different TKE peak values. Applying RANS profiles as input for the SEM, TKE peak values are low. Additionally, also long lengths are required to develop the TKE profiles. These development lengths are depicted in Figure 5.2. Additional illustrations are given in Appendix E. In the

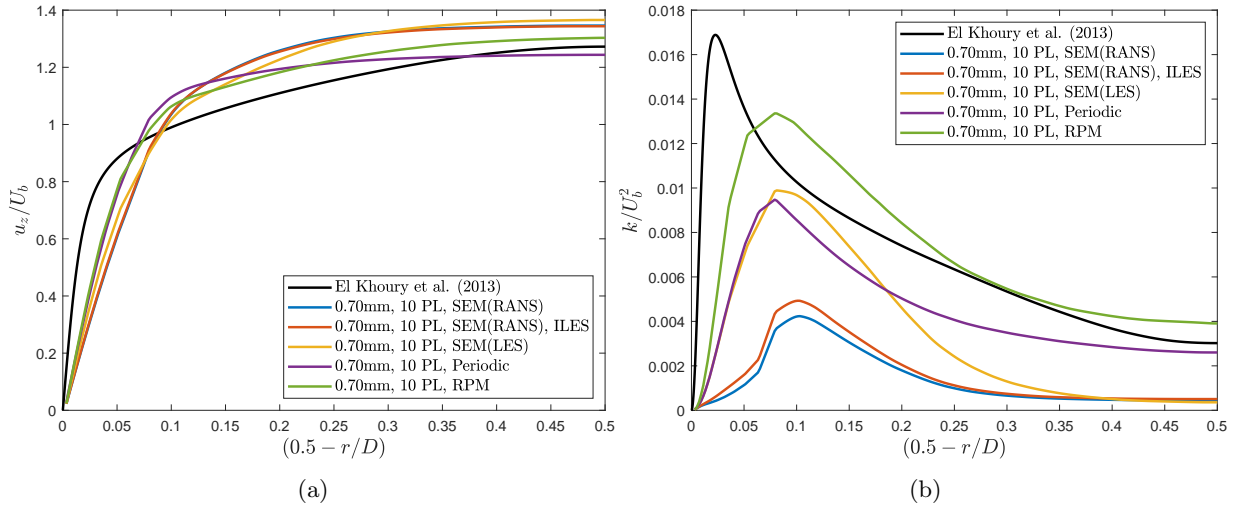


Figure 5.1: Flow statistic profiles for the different boundary conditions applied as a function of radial distance to the wall at $z/D = -2$ compared with DNS. a: The axial velocity normalized with the bulk velocity. b: The TKE normalized with the bulk velocity squared.

beginning the TKE decreases drastically. This is because the TKE peak location of the RANS profile, see Figure C.2, does not match the TKE peak location on this grid. Performing implicit LES is expected to increase the energy in the system as no energy is removed by the SGS model. However, this effect is not significant. Some LES have shown a significant higher bulk TKE. This difference is not due to numerical dissipation only.

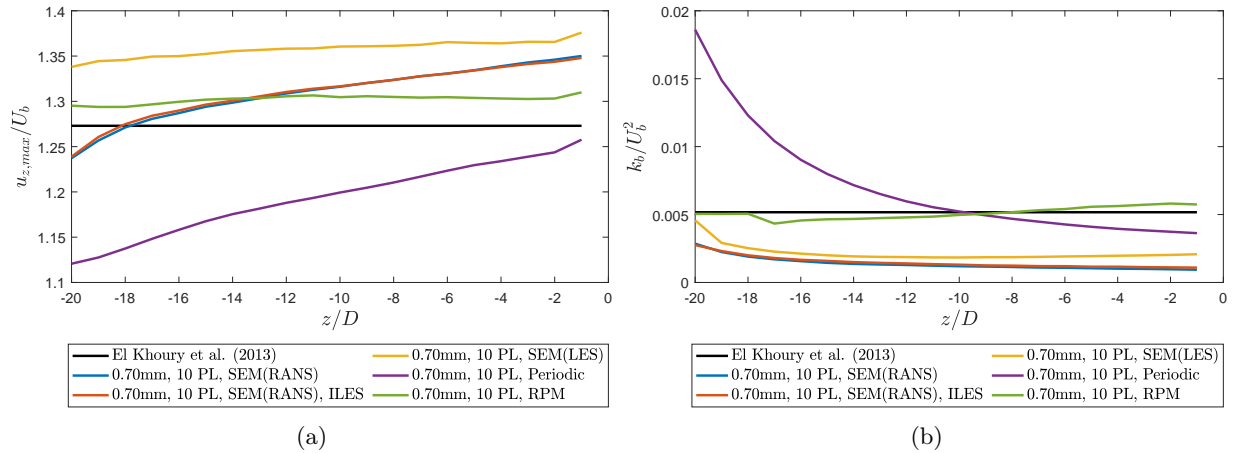


Figure 5.2: The development of quantities as a function of upstream distance to the inlet. a: The centerline velocity in axial direction normalized with the bulk velocity. b: The bulk TKE normalized with bulk velocity squared.

Regarding Figure 5.1b, applying the other proposed boundary conditions shows better simulated TKE peak values. Using the SEM applied with boundary conditions obtained from a precursor LES gives better results than before. Applying periodic boundary conditions results in proper profiles as well. But, with periodic boundary conditions profiles of stronger turbulent flow are applied at the inlet, see Figure 5.2b. This is because an orifice is included. If insufficient distance is provided, the flow does not return to pipe flow conditions. The TKE peak values are higher, but at the centerline the TKE is still insufficient. Besides, this method requires a precursor LES which is undesirable. The recycling plane method shows the best results.

The recycling plane method and using periodic boundary conditions are the easiest to implement. However, when applying periodic boundary conditions higher pressure fluctuations are seen in the whole domain,

see Figure 5.3. This is nonphysical because no significant hydrodynamic pressure fluctuations should be present upstream of the orifice. These higher pressure fluctuations are coupled in the CFD solver with the high velocity fluctuations at the inlet, see Figures 5.2b. The pressure fluctuations decay linearly from the inlet whereas the velocity fluctuations decay exponentially. Note that when using the SEM, the mass flow scaling specification option should be enabled as fluctuations in mass flow rate cause pressure fluctuations using incompressible solvers, see Figure 5.3a. All in all, specifying inlet turbulence with the recycling plane method is the most favorable method for LES on coarse computational grids with an orifice.

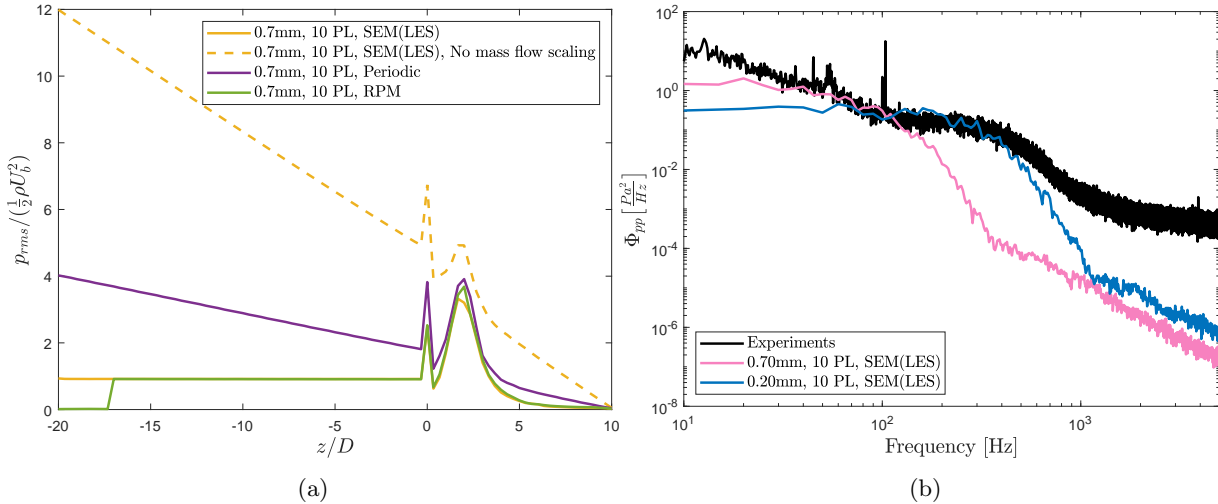


Figure 5.3: a: Wall pressure fluctuations normalized with the hydrodynamic pressure. b: The PSD of wall pressure fluctuations in a straight pipe.

Applying the RPM, lower wall pressure fluctuations exist in the extruded part of the domain, see Figure 5.3a. This $3D$ domain is obviously not influenced by the orifice which explains the lower wall pressure fluctuations. Van de Meerendonk (ASML (2020)) performed wall pressure measurements in straight pipes, see Section 3.3. Power spectra of wall pressure fluctuations just upstream of the outlet are compared with these experiments in Figure 5.3b. Results are obtained applying the SEM to the coarsest and finest computational grid. Results are not normalized because the mean wall shear stresses are significantly different.

In the frequency range from 50 to 500 Hz, LES on the finest computational grid compares well with experimental data. For higher frequencies, the content starts to deviate significantly from the measurement data. However, at this frequency the measurements include background noise and is therefore not reliable for higher frequencies. LES on the coarsest computational grid shows better results till a frequency of 100 Hz. At higher frequencies the LES deviates from the measurement and LES spectrum on the finest grid. According to Wagner et al. (2007) this might be indicative of a lack of spatial resolution which is manifested by an underpredicted power level. This is because energy contained by the unresolved eddy structures is lost in the SGS which explains the bad resolution at higher frequencies.

5.2 Computational grid refinement

Mainly LES results on grid 1 were regarded previously. This coarse grid has cell sizes larger than the Taylor microscales. Therefore, it should definitely be possible to obtain better simulation results by refining the computational grid. From now on only the recycling plane method will be applied for this refinement, for reasons mentioned in the previous section. The results of the refinement study will be compared with the DNS results of El Khoury et al. (2013). The velocity profiles at $z/D = -2$ are depicted in Figure 5.4 for the computational grids proposed in Table 4.1. LES on coarser grids result in shallow velocity slopes in the boundary layer. For finer grids the velocity slope steepens as illustrated in Figure 5.4a. However, the solution on the finest grid does not result in a better velocity profile at the centerline. In Figure 5.4b the velocity profiles are normalized with the friction velocity. In the viscous sublayer ($1 < y^+ < 5$) the velocity

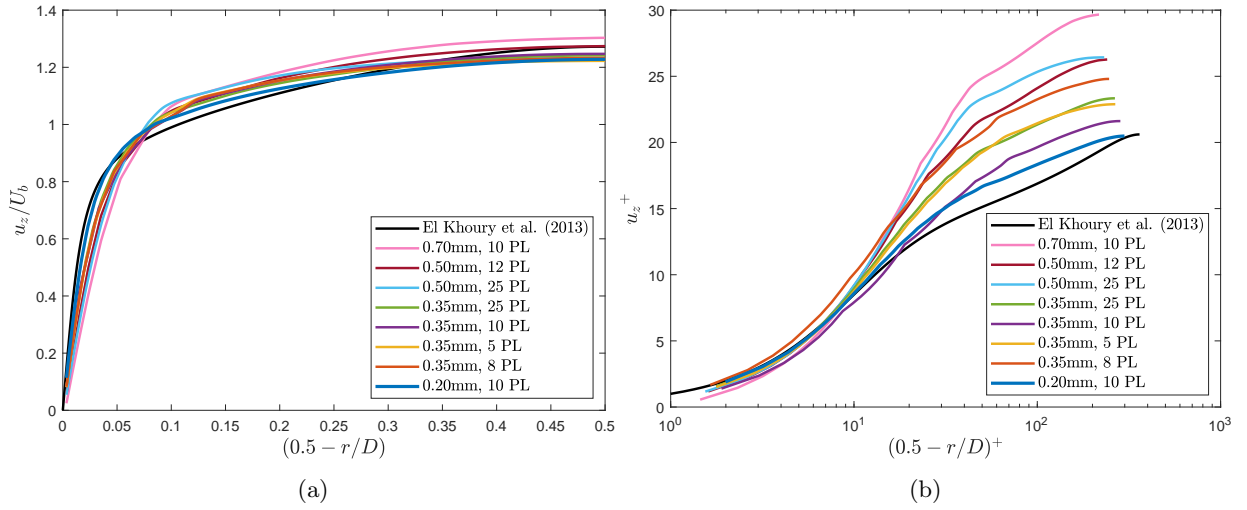


Figure 5.4: Velocity profiles in the axial direction at $z/D = -2$ for LES on different grids. a: Normalized with the bulk velocity. b: Normalized with the friction velocity.

is resolved or modelled with a reasonable accuracy. But, the solutions on the finer grids are significantly better. In the buffer layer ($5 < y^+ < 30$) the velocity profile starts to deviate from the DNS. This starts when the velocity profiles start to deviate from being approximately linear ($u^+ = y^+$). Further from the wall it should adopt the logarithmic representation of the profile. Refining the grid, the velocity gradually moves to the DNS solution in the logarithmic region. This behavior is coupled with the simulated wall shear stress. These wall shear stresses are significantly different for the LES on the analyzed computational grids.

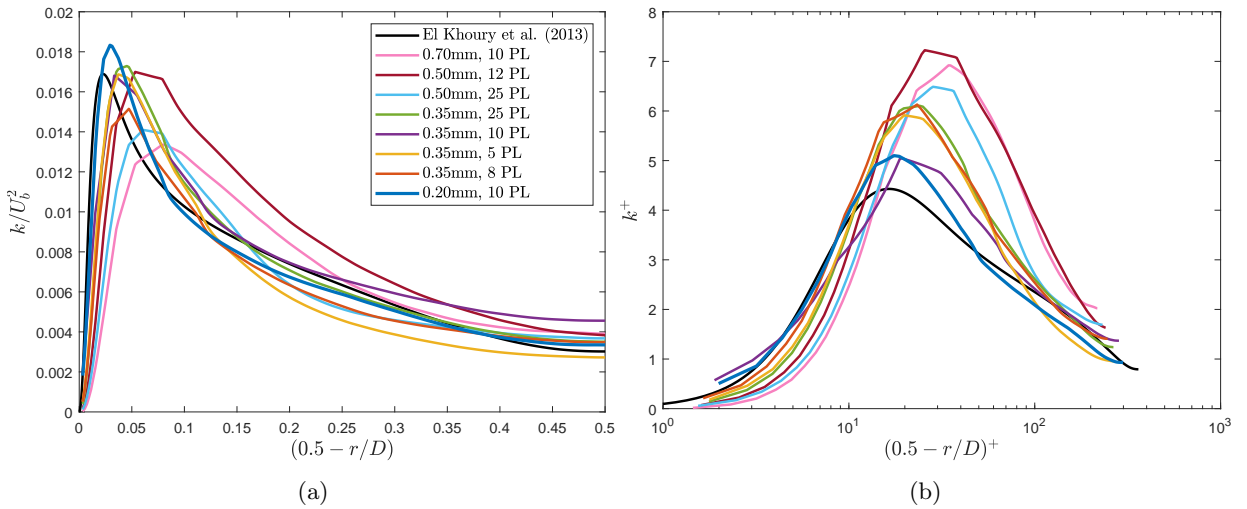


Figure 5.5: TKE profiles at $z/D = -2$ for LES on different grids, see Table 4.3. Results are compared with DNS of El Khoury et al. (2013). a: Normalized with the bulk velocity squared. b: Normalized with the friction velocity squared (see legend of others).

The TKE profiles are compared in Figure 5.5. The TKE peak values normalized with the bulk velocity squared tends to the right value for LES on finer grids, see Figure 5.5a. Additionally, the peak shifts to the right location closer to the wall. The TKE normalized with the friction velocity squared is illustrated in Figure 5.5b. The TKE is more accurately resolved and modelled in the whole inner and outer layer for LES on finer grids. A main contribution to this is the simulated wall shear stress, affecting the friction velocity, see Equation 3.6. The turbulent wall shear stress are compared with DNS in Figure 5.6. The total

shear stress in fluids is given in Equation 2.24. Den Toonder and Nieuwstadt (1997) mentioned that

$$\tau_T^+ + \tau_v^+ = 2 \frac{r}{D} \quad (5.2)$$

The solutions tend to this straight line as seen in Figure 5.6a. In Figure 5.6b it is shown that the turbulent shear stress is better resolved with LES on finer grids. This is again affected by wall shear stress which will be elaborated on later.

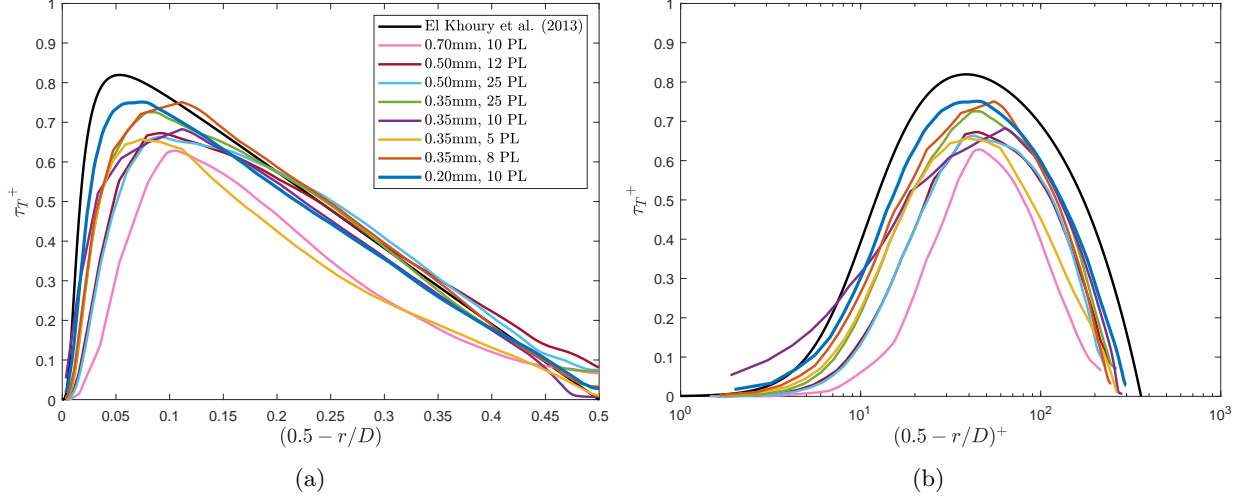


Figure 5.6: Turbulent shear stress profiles at $z/D = -2$ for LES on different grids. a: Normalized with the friction velocity squared. b: Normalized with the friction velocity squared on logarithmic x-axis (see legend of others).

The development of the bulk velocity and centerline velocity in axial direction normalized with the bulk velocity as a function of distance to the orifice are illustrated in Figure E.2. Both are stabilizing in the provided $20D$ upstream for all used computational grids. In Figure E.3 the development of the bulk and peak TKE normalized with the bulk velocity squared is depicted as a function of distance to the orifice. Downstream of the first $3D$, both show a decrease in TKE. The TKE values on the different computational grids then recover and stabilize within the provided $20D$. The TKE needs more distance to settle compared to the velocity, which is a lower order statistic.

5.3 Wall shear stress

As mentioned before, there is a significant deviation in simulated wall shear stresses using the different computational grids. The wall shear stresses and grid parameters that might affect the wall shear stress are tabulated in Table 5.1.

Table 5.1: The simulated wall shear stress and the computational grid properties.

	Grid 1	Grid 2	Grid 3	Grid 4	Grid 5	Grid 6	Grid 7	Grid 8
τ_w [Pa]	2.12	2.60	2.42	3.16	3.62	3.19	2.97	4.02
Cell size (CS) [mm]	0.86	0.63	0.63	0.43	0.42	0.41	0.42	0.27
No. prism layers	10	12	25	25	5	12	8	10
δ_p^+	49	49	49	49	70	70	70	49
SF	1.5	1.5	1.3	1.3	1.2	1.2	1.5	1.1
y_1^+	0.22	0.10	0.04	0.04	4.70	0.84	0.71	1.54
$\delta_{p,last}/CS$	0.27	0.37	0.26	0.37	0.66	0.45	0.83	0.43
CS_{last}/CS	0.66	0.72	0.64	0.74	0.85	0.77	0.95	0.79

The total prism layer thickness does not seem to have a direct effect on τ_w . Neither does the y_1^+ -value. However, τ_w increases with a decrease in cell size in the bulk region and cell size of the last prism layer. The

fraction of both, which represents the smoothness in cell size between the bulk region and near wall region, also shows a strong correlation with the wall shear stress. This is all depicted in Figure E.4. However, some computational grids diverge from this trend. This is the case for the grid with a base size of 0.35mm and 8 prism layers. This is explained by its high stretching factor compared to the other meshes with a base size of 0.35mm. Therefore the fraction of the cell sizes and stretching factor are divided with the stretching factor. Figure 5.7a illustrates a trend of increasing wall shear stress by decreasing the stretching factor and ratio of cell sizes. Additionally, in general the cell size has to be decreased.

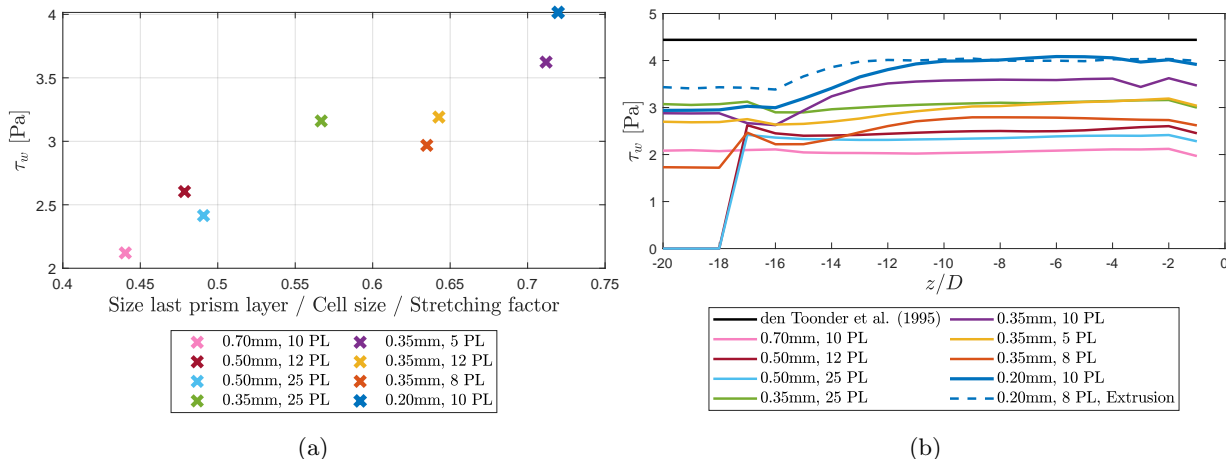


Figure 5.7: a: The wall shear stress as function of different computational grid properties. b: The wall shear stress development as a function of upstream distance to the inlet.

The development of the wall shear stress as a function of upstream distance to orifice is illustrated in Figure 5.7b. Note that in some simulations the wall shear stress is extracted zero because the pipe wall of the extruded part which is just a setup mistake. In general the wall shear stress settles very fast applying the recycling plane method. However, some simulations show a lower wall shear stress in the extruded part, which is not expected using the recycling plane method. The LES which are extruded without remeshing (grid 5 to grid 8) are showing this. This is in contrast with the conclusions in Section 4.5.2. Having extruded cells was namely expected to be better. So the transition in cell structure explain the different predicted wall shear stress. The choice not to change the cell size locally around the orifice is thus strengthened.

Grid 8 does not contain the right amount of extruded layers in stream wise direction, see 4.1. Comparing with a LES of a straight pipe extruded with the right number of layers (135 cells), a better match in wall shear stress is simulated, see Figure 5.7b. The wall shear stress of the dashed line is higher in the extruded part. This emphasizes the importance of applying correct cell shapes again in LES. Despite that, both wall shear stress lines match for sufficient distance from the inlet. It is concluded that extrusion in combination with remeshing works better for providing information to inlet of the region of interest.

5.4 Conclusions

In the previous study flow characteristics in turbulent pipe flow have been analyzed. The results of this analysis are taken into account for analyzing the turbulent flow around and orifice using practical LES. The results of this study are treated in the following chapter. The main conclusions from the straight pipe analysis are

- Inlet profiles should be applied which are close to the expected profiles in turbulent pipe flow on that grid when applying the SEM on coarse grids.
- The recycling plane method performs best in terms of development length and flow statistics and is therefore used for further analysis.
- The LES on the finest grid shows a good agreement with the experimental data of wall pressure fluctuations for turbulent flow in straight pipes.

- The flow characteristics simulated with LES on the finest grid compares best with DNS.
- Remeshing the extruded part results in a better prediction of the wall shear stress in straight pipes.

Chapter 6

Results of Orifice

In this chapter LES results turbulent flow through pipes with an orifice are presented. The recycling plane method will be used at the inlet and the same computational grids will be applied as in Chapter 5. First the velocity fluctuations will be studied and compared with DNS. Afterwards, the static pressure drop and mean force on the plate are studied. The static pressure drop will be compared with values found in literature. Also the fluctuating pressure drop and fluctuating force on the plate are analyzed. Additionally, the accuracy of the simulations will be analyzed. This will be done based on different value criteria and comparing the data with experimental data and DNS. In this chapter always the gauge pressure is considered, which is the difference between the total pressure and atmospheric pressure. Besides, a simulation performed with LES on computational grid 8 is abbreviated with LES 8.

6.1 Velocity fluctuations

The frequency content of velocity fluctuations in the domain is studied computing the one-dimensional energy spectrum. One-dimensional energy spectra are computed by generating the PSD of velocity signals in axial direction. Results will be compared with DNS data of turbulent channel flow at $Re = 10000$ by Lee and Moser (2015) extracted from a turbulence database. It is assumed that the energy content at the centerline of pipe and channel flow are equal for similar turbulent levels. This data is provided as a function of the wave number, κ . According to Taylor's hypothesis Taylor (1938), power spectra and frequency are related as $E(\hat{f}) = E(\kappa)2\pi/U_b$ because $\hat{f} = \kappa U_b/(2\pi)$. This assumption of frozen turbulence thus allows to interpret measured time series at a single point as spatial variations. As done by Lee and Moser (2015), energy spectra of LES and DNS are normalized respectively as

$$\Phi_{vv}^*(f) = \frac{f E_{zz}(f)}{U_b^2}, \text{ and } \Phi_{vv}^*(\hat{f}) = \frac{\hat{f} E_{zz}(\hat{f})}{U_b^2} \quad (6.1)$$

Note that the spectra are normalized with the bulk velocity of the pipe. When normalizing the spectra with the friction velocity, a distorted view is expected between the spectra of the different results. In Figure 6.1 the one-dimensional velocity spectra are compared with DNS for axial locations $z/D = -5, 0, 5$ and 10. Kolmogorov (1941) has shown that for isotropic hydrodynamic turbulence, the inertial subrange of an one-dimensional energy spectrum scales as $\Phi_{vv} \propto f^{-5/3}$. This slope is included in the following figures.

In Figure 6.1a the upstream velocity spectrum, at $z/D = -5$, simulated on the finest grid matches with the slope for isotropic turbulence. Additionally, results on that grid are in accordance with the DNS for a wider frequency range. Velocity spectra on computational grids with the same grid size coincide at frequencies above 100 Hz. This indicates a strong grid dependency. The area under the graphs increases as a function of decreasing grid sizes. It is concluded that in the straight pipe region a larger part of the flow is resolved when performing LES on finer grids. Besides, LES 8 shows a slope of $f^{-5/3}$ in the inertial subrange, so this range is properly resolved in the straight pipe region. Every LES shows a particular frequency at which the energy content starts to deviate from DNS. This effect is attributed to dispersion as content is shifted to higher frequencies. The occurrence of this numerical noise starts at lower frequencies for coarser

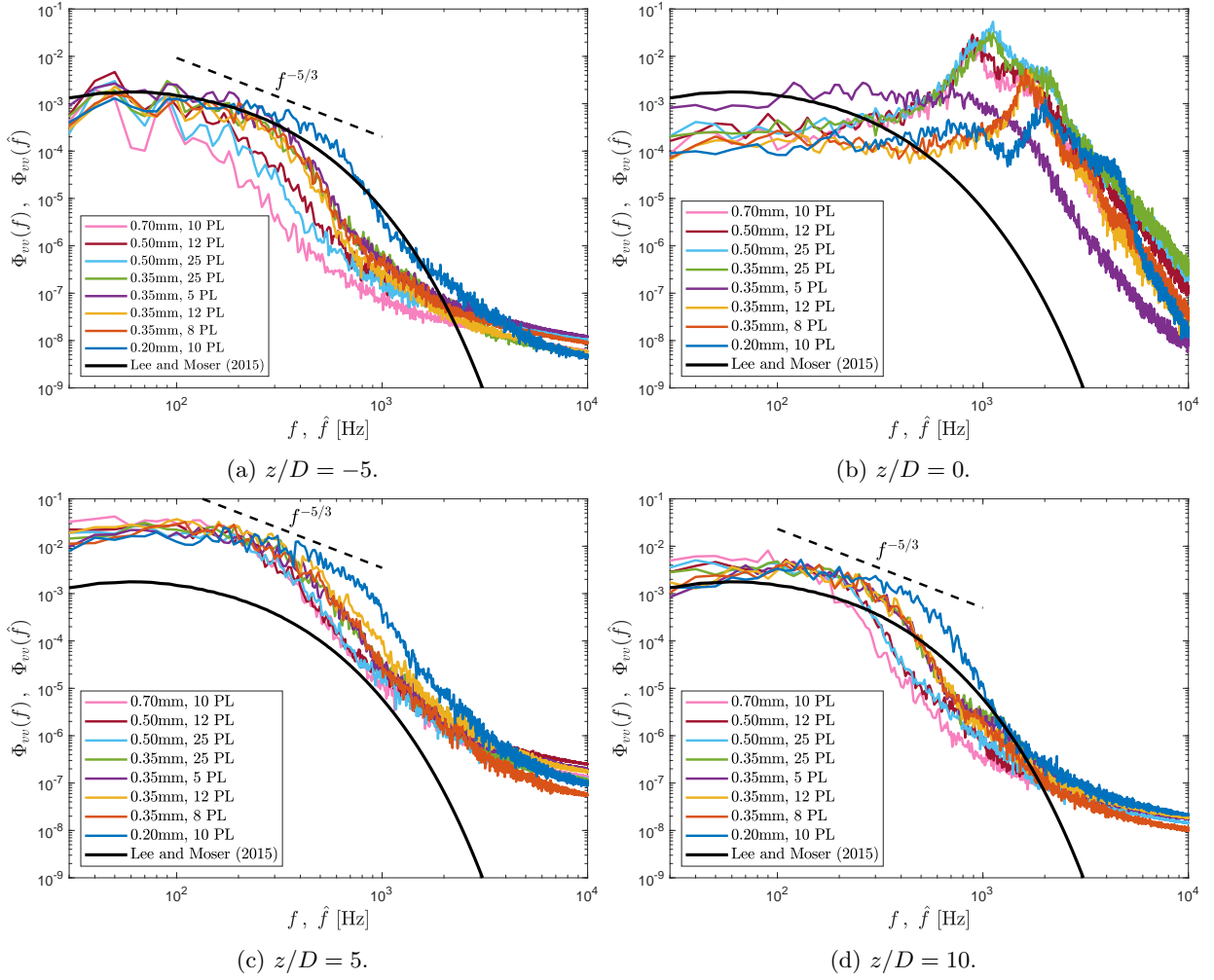


Figure 6.1: The normalized one-dimensional velocity spectra in flow direction obtained with LES on different grids compared with DNS (Lee and Moser (2015)). Data is probed at the centerline at different axial locations; a: $z/D = -5$, b: , c: , and d: .

grids and at higher frequency if finer grids. This is due to the grid frequency a computational grid can represent.

Inside the orifice, at $z/D = 0$, the turbulent flow strongly deviates from isotropic turbulence, see Figure 6.1b. The content of the velocity fluctuations is decreased in the lower frequency range and is increased in the higher frequency range compared to $z/D = -5$. This implies that larger turbulent structures are not entering the orifice. However, smaller turbulent structures are forming and dominate the energy spectrum at higher frequencies. The energy spectrum simulated on grid 5 strongly deviates from the other results. This might be related to the very poor resolution in the orifice region, see Figure D.1. The peaks around 1000 Hz may be introduced by the orifice. However, no general peak frequency can be designated. At higher frequencies the decay is high. Note that no dominant numerical errors are visible at higher frequencies. This is likely because content is higher than the error itself. Besides, the grid frequency is higher which may result in errors at higher frequencies only.

Downstream of the orifice, at $z/D = 5$, the energy content is large for all frequencies, see Figures 6.1c. Moving in flow direction, at $z/D = 10$, the energy spectrum shows that the flow returns to isotropic turbulent flow, see Figure 6.1d. The $f^{-5/3}$ -trend is recognized again for the energy spectrum by LES 8. Additionally, computational grids with similar cell sizes cause results to merge and the content over the whole frequency range drops.

6.2 Pressure drop

Table 6.1: Pressure and force data by LES on different computational grids.

	Grid 1	Grid 2	Grid 3	Grid 4	Grid 5	Grid 6	Grid 7	Grid 8
$\overline{\Delta p}$ [bar]	0.236	0.239	0.239	0.242	0.169	0.257	0.252	0.241
Δp_{rms} [Pa]	732.4	732.3	738.4	720.2	345.4	248.9	281.6	571.9
\overline{F}_{total} [N]	1.483	1.514	1.510	1.535	1.070	1.631	1.601	1.532
ζ_1 [%]	1.023	0.532	0.538	0.270	0.305	0.102	0.217	0.045
$F_{t,rms}$ [mN]	46.0	46.0	46.0	45.7	21.4	15.1	17.6	35.6
ζ_2 [%]	0.042	0.038	0.038	0.009	0.052	0.044	0.020	0.052

The pressure drop induced by an orifice is significantly larger than the pressure drop in a straight pipe. Including an orifice with an area ratio of 20% and a thickness of $t/D_h = 0.5$ should result, with the chosen mass flow rate, in a pressure drop of $\Delta p = 0.260$ bar (Idelchik (1986); Tullis (1989)). The mean wall pressure as a function of normalized distance to the orifice is depicted in Figure 6.2. In here also a schematic of the point probe locations around the orifice is added. Note that the pressure goes to 0 Pa because a zero pressure boundary is applied at the outlet in LES. The difference between the maximal and total permanent pressure drop is clearly visible.

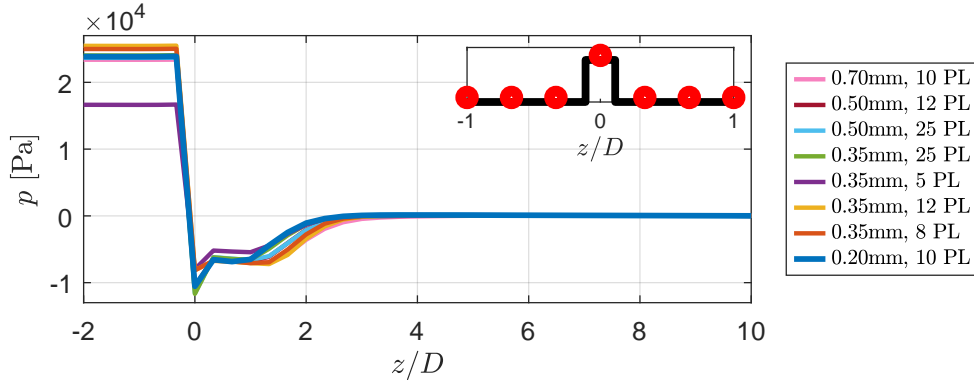


Figure 6.2: Mean wall pressure as a function of normalized distance to the orifice for LES on different computational grids. A schematic of distribution of wall point probes is included.

The total permanent pressure drop of all LES is tabulated in Table 6.1. All LES show a pressure drop around $\Delta p = 0.25$ bar which are close to the value in literature, except for grid 5. The root mean square values of the pressure drop fluctuations between the inlet and outlet are tabularized in Table 6.1. In contrast with the mean pressure drop values, the fluctuations of the pressure drop show a significant spread.

6.3 Pressure fluctuations

Despite that pressure waves cannot radiate in incompressible CFD simulations, the wall pressure fluctuations in the jet-wake region can be compared with the measured pressure fluctuations. Hydrodynamic pressure fluctuations are measured by Anantharaman (2014) and Kottapalli. Data of Anantharaman only ranges till a frequency of 800 Hz. Therefore, Equation 3.3 is applied to specify the frequency range for the p_{rms} calculation. This guarantees a fair comparison between experimental data and LES. Integrals are evaluated over a frequency range from 10 Hz to 800 Hz so significant pump behavior is disregarded, see Figure 3.2. The normalized wall pressure fluctuations as a function of normalized distance to the orifice are depicted in Figure 6.3. LES on all grids and both experiments are included.

No pressure fluctuations are seen at $z/D = 10$ because in LES a zero pressure boundary is applied at the outlet. Additionally, $2D$ upstream of the outlet no large pressure fluctuations are found because

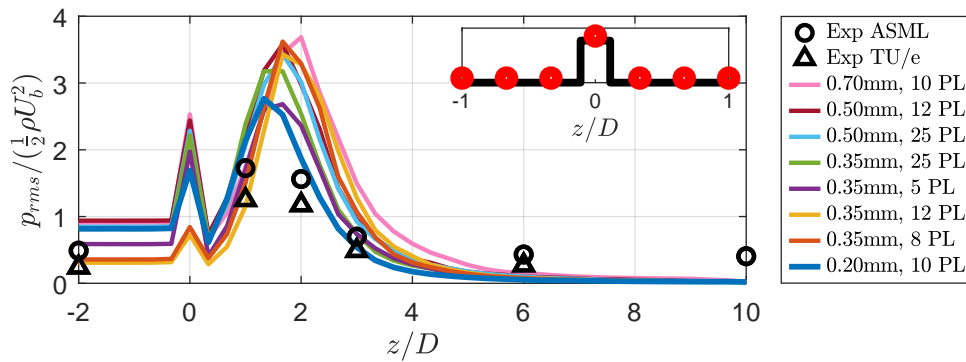


Figure 6.3: Normalized wall pressure fluctuations obtained with LES on different computational grids as a function of normalized distance to the orifice. A frequency range from 10 Hz to 800 Hz is considered. A schematic of the distribution of wall point probes is included.

acoustic waves do not radiate in incompressible LES. Therefore, there LES and experiments are not directly compared. The LES pressure fluctuation just upstream and downstream of the orifice are roughly equal. In the jet-wake region, at $z/D = 1$, both LES and experiments compare well. At $z/D = 2$ and $z/D = 3$ refining the computational grid leads to a better comparison with the experiments. However, as the experimental data obtained at the TU/e is expected to contain the least noise, the LES wall pressure fluctuations are over predicted. Unfortunately the experimental data does not provide additional resolution at $z/D = 1.5$ as Agarwal (1994b) has measured a peak in pressure fluctuations of air flow through an orifice between $z/D = 1$ and $z/D = 2$. At $z/D = 6$ the acoustic content in the experiments declares the difference between LES and experiments.

On the middle surface of the orifice, at $z/D = 0$, significant pressure fluctuations are simulated, see Figure 6.3. At that location flow separation occurs which is expected to give, in combination with reattachment, high pressure fluctuations (Anantharaman (2014)). No pressure transducer is included in the experiments at that location. However, as the pressure fluctuations are coupled with the fluctuations in velocity, shear stress components at that location can be regarded. In Figure 6.11a, τ_{xx} and τ_{zz} show larger fluctuations in velocity at the orifice compared to the dead zone close to the wall. PIV results performed by Anantharaman (2014) confirm the velocity fluctuations around the orifice, see Figure 6.11b. Additionally, higher velocity fluctuations are expected because of an increase in Reynolds number in the orifice hole. This indicates that the large hydrodynamic pressure fluctuations at the orifice at $z/D = 0$ are physical. Regarding the PIV results in Figure 6.11b, hydrodynamic pressure fluctuations simulated with LES 6 and 7 are expected to be inaccurate. Upstream of the orifice wall pressure fluctuations out of LES cannot be directly compared with the experimental data. But, it is remarkable that the wall pressure fluctuations are high and constant as a function of axial distance to the orifice. This behavior will be explained later.

Besides the average value of pressure fluctuations, the pressure content as a function of frequency gives in the LES results. The wall pressure spectra simulated with LES at $z/D = 1, 2, 3$ and 6 downstream of the orifice are depicted in Figure 6.4. Pressure spectra obtained with experiments by Kottapalli are added. The slope of the measured pressure spectra is included in the figures. Acoustic noise is neglected.

At $z/D = 1$ the pressure content of the LES deviates within one order of magnitude at frequencies till 500 Hz, see Figure 6.4a. The shape of the PSDs match with the experimental pressure spectrum, but no clear trend is seen. At higher frequencies, the spectra start to decay. The slope is simulated steeper with LES for coarser grids. Neglecting the acoustic content, the slope of LES 8 matches best with the experiments. The slopes by the other LES are too steep. At $z/D = 2$ content at lower frequencies is more stable as a function of frequency, see Figure 6.4b. LES on coarser grids show a higher content and is decreasing for LES on finer grids. At 300 Hz the content starts to decrease. The decay of LES 8 again matches best with experimental data. The others are again steeper.

At $z/D = 3$, the acoustic pressure fluctuations become dominant over the hydrodynamic pressure fluctuations already at a frequency of 300 Hz. Regarding Figure 6.4c and neglecting the acoustics, the content and slope of LES 8 are the best comparing with the experimental data. The content at lower frequencies

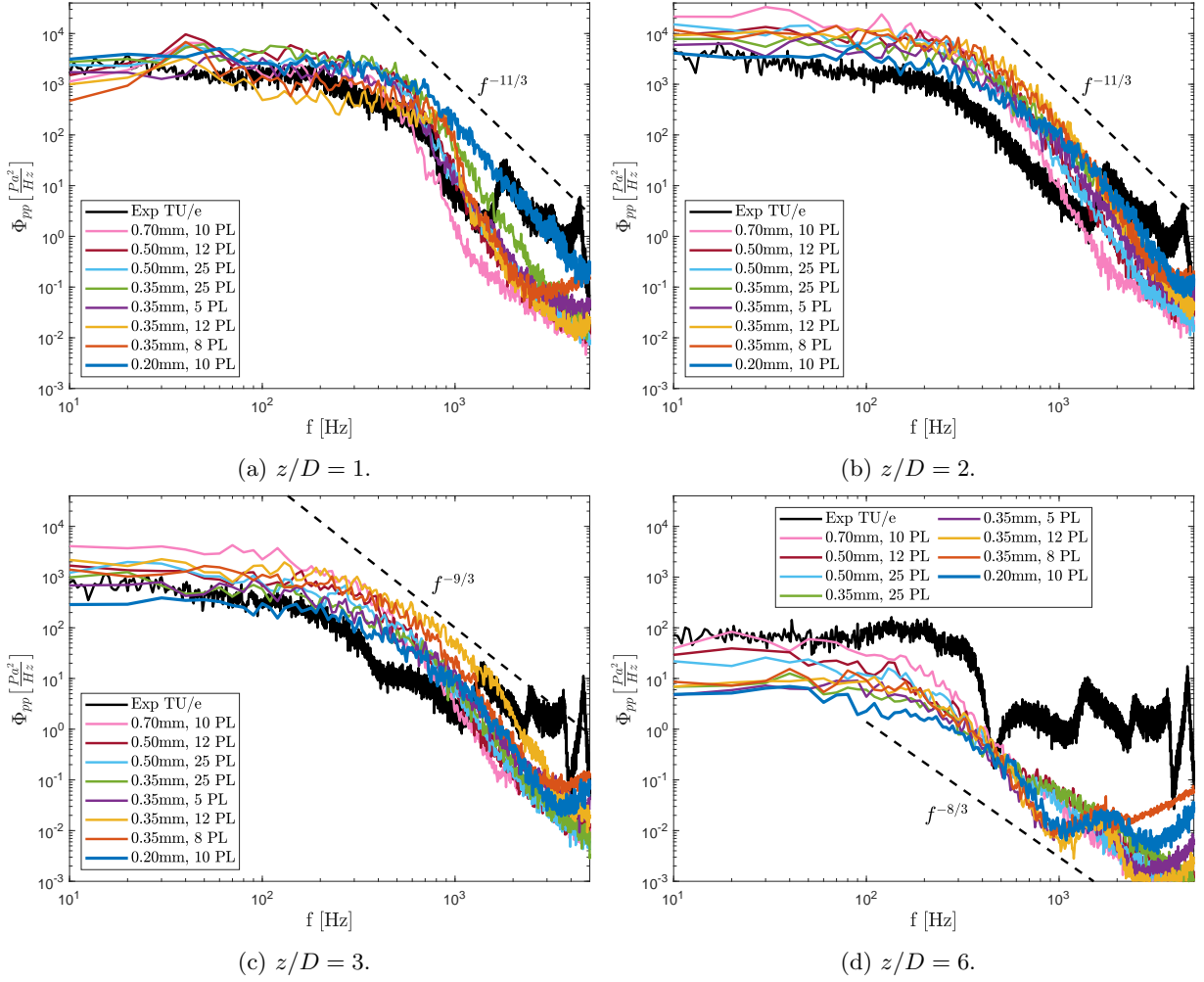


Figure 6.4: The wall pressure spectra obtained with LES on all computational grids. The slope of the experimental data obtained by Kottapalli is included. Data is probed at different axial locations.

decreases when refining the grid, as seen before. Further downstream, at $z/D = 6$, the acoustics are very dominant, see Figure 6.4d. Remarkably the LES on coarser meshes simulate a better slope compared to the fine simulations. Additionally, strange fluctuations are found for the LES on grid 5 to 8. LES 1 and 2 are performed with a lower pressure under-relaxation factor. This might result in a better monotonic stabilization of the residuals. Dispersive errors, characteristic of second-order upwind schemes, can produce non monotonic residuals and smear results less. Because of the increased pressure under-relaxation factor, residuals are not perfectly flattening in a monotonic way, see Figure 4.11. This might introduce dispersive errors which are especially dominant in the higher frequency range where pressure content is small. However, it is more likely that it is a grid dependent phenomenon. Grids 6 to 8 have a thinner prism layer around the orifice, see Section 4.4.3. This change maybe leads to errors or the capture of a physical behavior. Nonetheless, the observed pressure fluctuations are assumed not to affect the force spectrum because the magnitudes are low. So from the comparison with pressure fluctuations in the jet-wake region with experimental data, LES 8 shows best results in terms of p_{rms} values and slopes of decay.

The obtained LES pressure spectra are compared with power laws, as suggested by Kottapalli (2020). They mentioned that in homogeneous isotropic turbulence, the inertial subrange of power spectra typically shows a power law of $f^{-7/3}$ resulting from a turbulence-turbulence interaction (Hill and Wilczak (1995); Zhao, Cheng, Qiu, Burnett and Liu (2016)). Isotropic conditions do only apply in shear free flow. At locations close to the orifice, shear stresses play a major role, as will be shown later in Figure 6.11. George, Beuther and Arndt (1984) found that pressure spectra decay as $f^{-11/3}$ when dominated by shear stress-turbulence interactions. With that, the decay of a pressure spectrum in the inertial subrange as a function of frequency

for sufficiently high turbulence is superposed as

$$\Phi_{pp}(f) = \Phi_s(f) + \Phi_t(f), \quad \Phi_s(f) \propto f^{-11/3}, \quad \Phi_t(f) \propto f^{-7/3} \quad (6.2)$$

Tsuji and Kaneda (2012) have shown that this suggestion also holds for anisotropic wall bounded shear flows. Pressure spectra of wall pressure fluctuations at different location downstream of the orifice are depicted in Figure 6.5 for respectively LES 4 and LES 8.

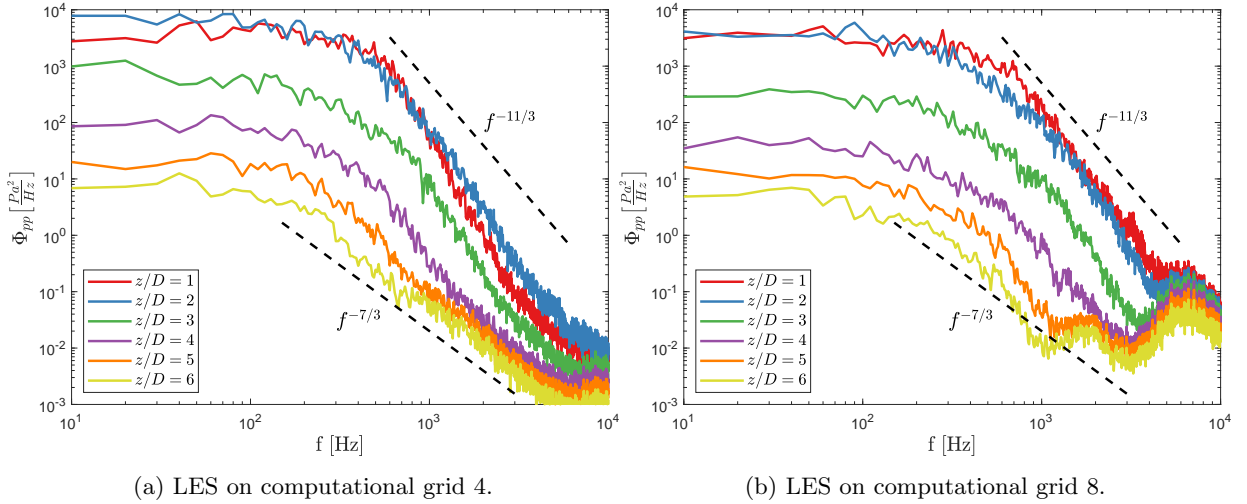


Figure 6.5: Wall pressure spectra obtained with LES at locations $z/D = 1$ till $z/D = 6$. Power laws $\Phi_s(f)$ and $\Phi_t(f)$ are included.

At $z/D = 1$ and $z/D = 2$, where the shear stresses are the highest, the PSDs agree with $f^{-11/3}$ indicating shear stress-turbulence interaction. Further downstream, the slope of the PSDs decrease. At those locations, a significant frequency range agrees with $f^{-7/3}$ indicating turbulence-turbulence interaction. Note again that LES 8 shows higher frequency content at higher frequencies possibly due to dispersion. All in all the resulting pressure spectra are concluded to be in well agreement with the power laws, as also found for the presented experimental results obtained by Kottapalli at TU/e.

Although comparison with experimental data is not legit for pressure fluctuations upstream of the orifice because of the dominance of acoustic noise, the characteristics of the flow give insight. As already seen in Figure 6.1 and in Chapter 5, the one-dimensional energy spectrum upstream of the orifice and the cross sectional flow statistics meet the characteristics of turbulent pipe flow. Additionally, the pressure spectrum is according to $\Phi_{pp} \propto f^{-7/3}$ in the inertial subrange for homogeneous isotropic turbulence.

Pressure spectra inside the orifice, at $z/D = 0$, and upstream of the orifice, at $z/D = -2$, are depicted in Figure 6.6. Inside the orifice sharp peaks are seen in the power spectra for every LES. As these peaks are not appearing at a similar frequency for every grid simulated on for a constant mass flow rate, it is thought that these peaks are nonphysical. Note that the peaks of LES 1 to 4 are roughly the same, whereas the other LES show very different behavior. Additionally, note that the extruded region of the first four grids is remeshed. This might lead to a smoother transition from extruded part to the region of interest which consequently might result in less introduced numerical pressure fluctuations. The frequencies at which the peak occurs scales with the grid size for grids 1, 3, 6 and 8. However, not every grids follows this trend. With this in mind, two main decay rates are found for every simulation: one including the peak and one excluding the peak. For LES 8 these are f^{-3} and f^{-12} as depicted in Figure 6.6a. The first slope is considered physical, whereas the latter slope is expected to be nonphysical because it is very high compared to the presented power laws of pressure spectra. Regarding the locations upstream of the orifice, all pressure spectra are similar to those inside the orifice, see Figure 6.6. The shapes are roughly the same showing similar peak-frequencies and decay rates. However, the values are generally lower. Because an orifice is a very strong disturbing source acting as a low-pass filter, the pressure spectra upstream of the orifice are resulting from this. As incompressible LES is performed, the pressure spectra are similar everywhere upstream of the orifice. This explains why the pressure spectra are different compared to the pressure spectrum in straight pipe flow.

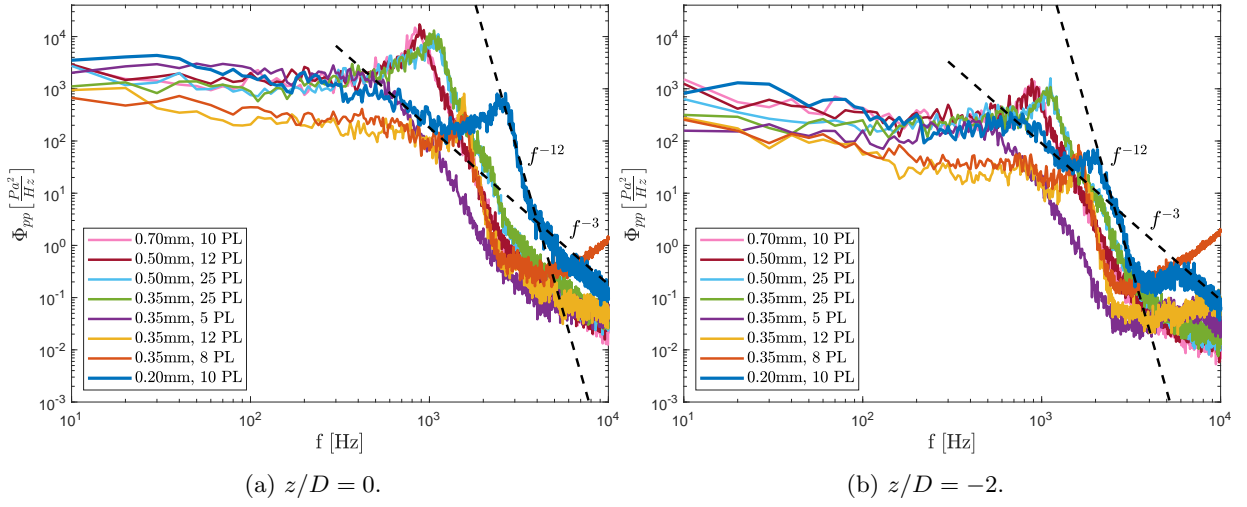


Figure 6.6: Wall pressure spectra obtained with LES on all computational grids.

To investigate if a high-frequency phenomenon can be attributed to the pressure spectra peaks, snapshots of the velocity field simulated with LES on computational grid 8 are studied. After counting the amount of vortex rings that have been shed in a time span of 0.06 physical seconds, a shedding frequency of $f \approx 1000 Hz$ is found. This corresponds to a nondimensionalized frequency of $St \approx 0.37$ which is in line with a Strouhal number range $St \approx 0.2-0.4$ found in literature. But, this frequency does not match the frequency of the peak simulated with LES on grid 8. Snapshots of the field are illustrated in Figure 6.7. Note that the snapshots are taken with the vortex ring visible at roughly $z/D = 1$.

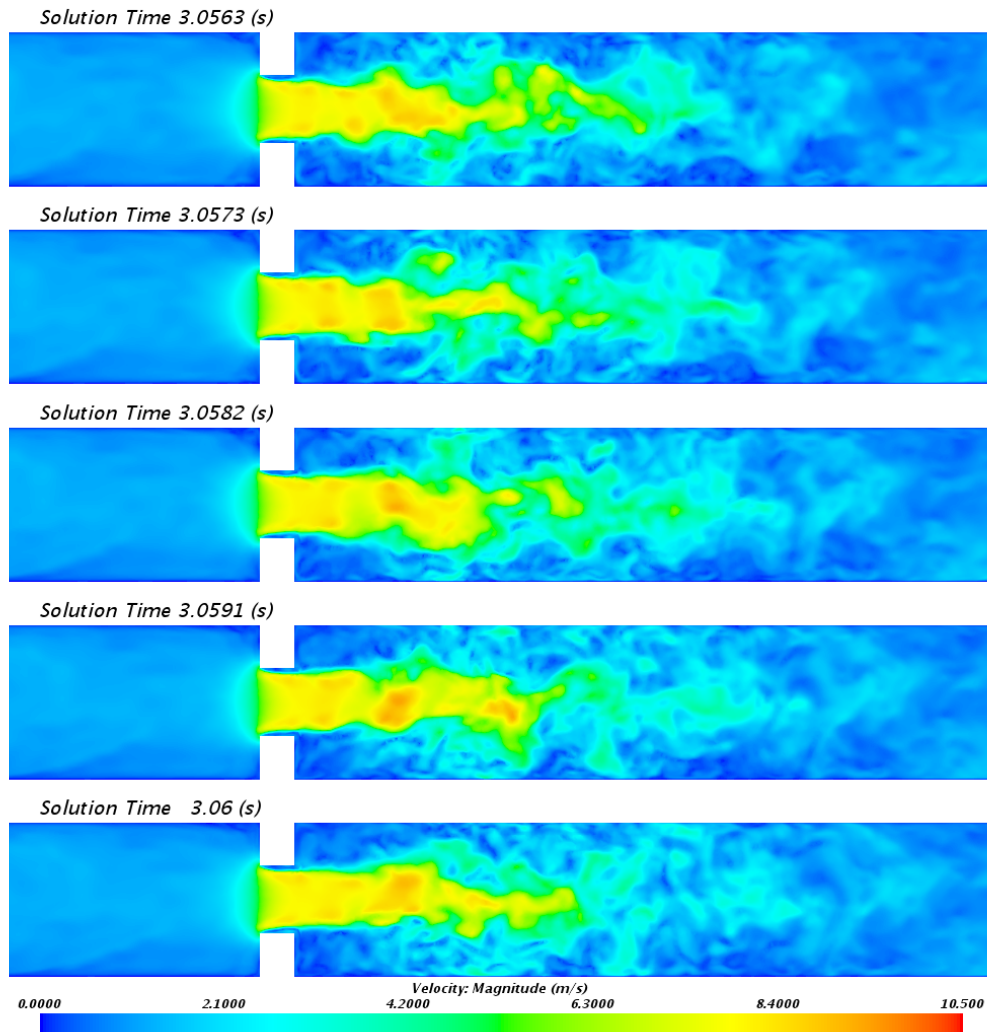


Figure 6.7: Snapshots of the velocity magnitude field at different time instants obtained with LES on the finest computational grid.

6.4 Source term

The source term is found to be a fluctuating force in Chapter 2. In LES the forces on the pipe wall, orifice up- and downstream facing surface and orifice middle surface are coupled with the pressure fluctuations in the system. The power spectra of these fluctuating forces simulated on the coarsest and finest grid are depicted in Figure 6.8a.

The up- and downstream facing surfaces of the orifice are showing the largest force fluctuations. These surfaces are exposed to most fluid inertia as these surfaces are perpendicular to the flow. It is seen in Figure 6.8a that the fluctuations on the upstream orifice surface are higher. A reason for this might be the increased pressure fluctuations upstream of the orifice introduced by the orifice itself. The fluctuating forces on the other two surfaces are resulting from wall shear stresses. The fluctuations on the pipe wall are seen to be submissive to the fluctuating forces on the orifice plate. So possible wall shear stresses by the jet have no significant effect on the force fluctuations via the pipe wall. Besides, this fluctuating force is a function of the domain length and is therefore disregarded in the determination of the source term. Note that it still plays a role in the momentum balance.

The summation of mean forces on the orifice surfaces is listed in Table 6.1 for the different LES. As the orifice stagnates the flow and creates a pressure drop, both the mean force and the pressure drop are

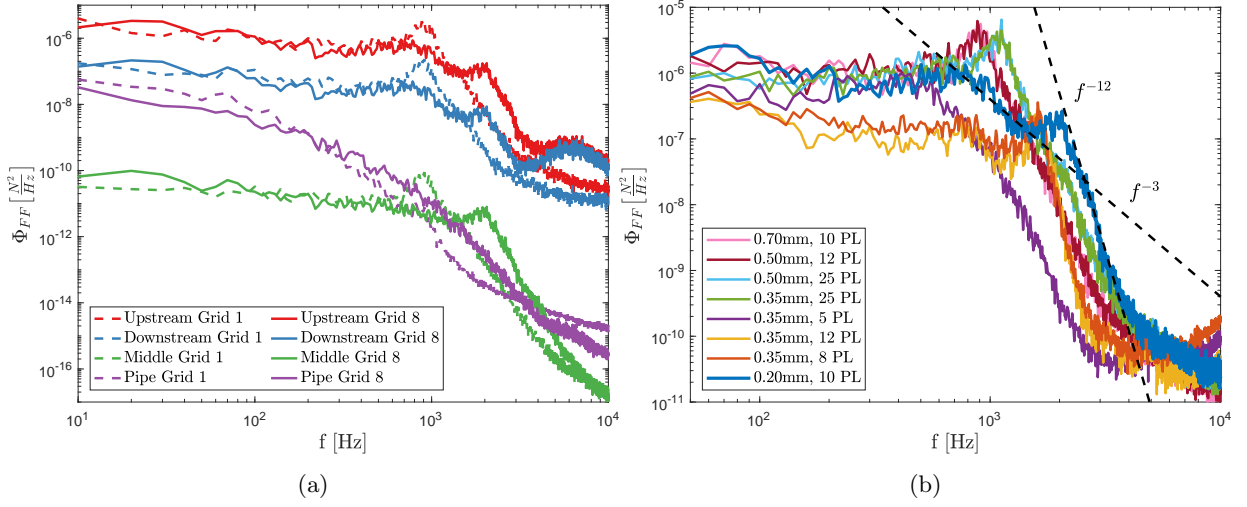


Figure 6.8: a: Force spectra on the different geometry surfaces simulated on the coarsest and finest grid using LES. b: Net force spectra on the orifice plate for different LES.

compared by calculating the normalized difference between the two as

$$\zeta_1 = \frac{\overline{\Delta p} - \frac{\overline{F}_{total}}{A_p}}{\overline{\Delta p}} \cdot 100\%, \quad \zeta_2 = \frac{\Delta p_{rms} - \frac{F_{t,rms}}{A_p}}{\Delta p_{rms}} \cdot 100\% \quad (6.3)$$

For the different considered computational grids, these values are listed in Table 6.1 as well. The normalized difference between the two is 1% or lower. These values therefore indicate that the mean pressure drop is directly coupled with the mean total force in the system divided by the cross sectional pipe area, A_p .

The force spectra of the total fluctuating force on the orifice plate are depicted for all LES in Figure 6.8b. Roughly speaking, most spectra show a constant content at higher frequencies and starts to decay at a particular frequency. A peak is present in almost all spectra as is found for the pressure spectra at $z/D \leq 0$. The force spectra therefore also show to slopes which are visualized in Figure 6.8b for LES 8. The decay rates are again f^{-3} and f^{-12} . No direct comparison with measurements is possible for Φ_{FF} , but it is likely that the spectra are coupled with the pressure spectra and therefore a slope of f^{-12} is again considered high. In contrast to this, the slope f^{-3} is very close to the proposed scaling $\Phi_{FF} \propto f^{-3.2}$ by Moussou (2006).

Root mean square values of the total force on the orifice plate, $F_{t,rms}$, are added to Table 6.1. Note that these values are obtained by taking the rms of the resultant total force signal in time, so all frequencies are included. Note that disregarding the force fluctuation on the pipe wall has a minor effect on the momentum balance. A large deviation in $F_{t,rms}$ -values is found for the LES on the different computational grids. As was the case for the mean values, the fluctuating pressure drop times pipe area and the fluctuating force are related. The normalized differences between the two are calculated with ζ_2 , see Equation 6.3, and also added to Table 6.1. Both are in balance with an error smaller than 0.1%.

To understand the similarity between force and pressure differences, the momentum equation (Equation 2.2) is rewritten in integral form, as done in the book by J. Anderson (2016), as

$$\frac{\partial}{\partial t} \iiint_V \rho u_i dV + \iint_S (\rho u_i dS) u_i = - \iint p dS - F_i \quad (6.4)$$

Note that viscous effects are neglected as these scale with $1/Re$. The problem is regarded as an interaction between a control volume inside the geometry and the geometry itself as depicted in Figure 6.9. p is the pressure to the body and F is the reaction force of the body to the fluid.

In Equation 6.4 the derivative w.r.t. time drops out as a constant mass flow rate is applied at the inlet boundary in LES and therefore the mass flux is constant. Note that incompressible LES are performed so the density is constant. The second term represents the mass flux over an area times the velocity, or

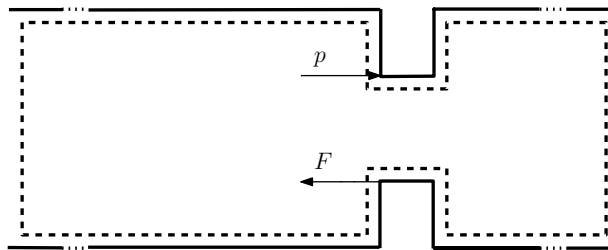


Figure 6.9: Control volume of the fluid in the domain.

momentum flux. The average mass flux at the inlet and outlet of the control volume are equal as well. However, the momentum flux deviates dependent on the location of the in- and outlet of the control volume as the velocity profile might be different. If the boundaries are taken far enough up and downstream, the velocity profiles are equal to that of turbulent pipe flow and the convective term is of no influence on the momentum balance. The boundaries of the control volume are the inlet and outlet boundary as the pressure drop is compared with. Therefore, the momentum equation only contains surface forces and reduces to

$$F_i = - \iint p dS \quad (6.5)$$

The difference in sign is explained from the fact that the pressure drops in positive direction. The small difference indication parameters ζ_1 and ζ_2 imply that momentum is conserved in the performed LES. Note that the contribution of the convective term can be determined by using the cross sectional profiles of pressure and velocity. Based on Figure 6.3 it can already be concluded that the convective terms has a contribution when the downstream control volume boundary is within the jet. Namely, then the fluctuating pressure drop in downstream direction is positive.

To study the correctness of the plateau of the PSDs, i.e. to analyze the values Δp_{rms} and $F_{t,rms}$, different control volumes need to be analyzed. Because the pressure is very diffusive, this value is for now assumed to be constant over a cross section in cross stream direction. Then, when regarding Figure 6.3, already the effect of choosing the downstream boundary inside the jet region can be judged. The Δp_{rms} will be positive in streamwise direction in that case. Therefore, the fluctuations in the convective term will be significant. This requires an additional investigation including the right profiles which can be obtained from the performed simulations. But, it is expected that the $F_{t,rms}$ -value will be affected by the slightly overpredicted pressure fluctuation in the jet-wake region.

All in all, the high pressure fluctuations upstream of the orifice are a direct result of the fluctuating force by the orifice to the fluid. The high pressure fluctuations are located upstream of the orifice because a zero pressure outlet is applied. If the inlet is chosen to be a zero pressure inlet and the outlet is chosen to be a mass flow outlet, the result will be equal, but the high pressure fluctuations are build up downstream of the orifice.

6.5 Orifice resolution

Besides the resolution of flow in the straight pipe region treated in Chapter 5, the orifice and jet-wake region have to be resolved with an acceptable accuracy. A well resolved solution in this region requires finer computational grids. This is shown in Figure C.3 regarding the Taylor micro scales. In Section 4.2.4 a method to judge accuracy is proposed comparing the subgrid kinetic energy to TKE (M_{TKE}) and the turbulent viscosity ratio (TVR). Maximum LES field values of these parameters are tabulated in Table 6.2. As around the orifice one single cell gives very high values for the TVR , the listed values are based on maxima in the jet-wake region. For the M_{TKE} , the cells adjacent to the wall are not taken into account as these are always one because of pure modelling. The turbulent viscosity ratio decreases linearly with cell size refinement. μ_T accounts for the stress effects of the smaller underresolved eddies on the larger resolved scales. A small μ_T -value indicates that a larger proportion is directly resolved for. Please note that the total simulated fluid stresses are not necessarily different. So, in line with expectations, a larger proportion of scales is resolved using LES on finer computational grids. For LES $TVR = 10$ is considered sufficiently low. The TVR -field simulated with LES 8 is depicted in Figure 6.10a. Most of the values in the jet-wake

region are around $TVR = 15$. Far up- and downstream of the orifice these values are $TVR < 2$ for all LES. Therefore, it is concluded that the pipe region is properly resolved whereas the jet-wake regions are simulated with an insufficient accuracy. Nonetheless, the TVR on grid 8 is acceptable.

Table 6.2: Values for the turbulent viscosity ratio ($TVR = \mu_T/\mu$) and the subgrid kinetic energy to TKE ratio ($M_{TKE} = k_{SGS}/(k_{SGS} + k_{res})$) simulated with LES on different computational grids.

	Grid 1	Grid 2	Grid 3	Grid 4	Grid 5	Grid 6	Grid 7	Grid 8
TVR	104.9	73.65	77.88	52.33	55.06	56.56	52.79	24.94
M_{TKE}	0.980	0.973	0.977	0.967	0.966	0.963	0.963	0.895

The listed maximum values for M_{TKE} are large compared to the criterion $M_{TKE} = 0.2$, see Table 6.2. Most TKE is modelled just upstream of the orifice, see Figure 6.10b. This is explained by ℓ_0 being smallest upstream of the orifice, see Figure 6.10c. In contradiction with TVR , decreasing cell size does not lead to a significant decrease in the modelled TKE. In the pipe region and jet-wake region, M_{TKE} -values are acceptable for all performed simulations.

Based on M_{TKE} , in some regions large proportions of the velocity fluctuations are not resolved. Via the velocity-pressure coupling, this would mean that the pressure fluctuating field is also simulated poorly as well. So if only the velocity fluctuations just upstream of the orifice hole determine the p_{rms} -field, this would lead to poor representations of the p_{rms} -field. However, as the TKE is a minor fraction of the TKE downstream of the orifice, this is not a problem.

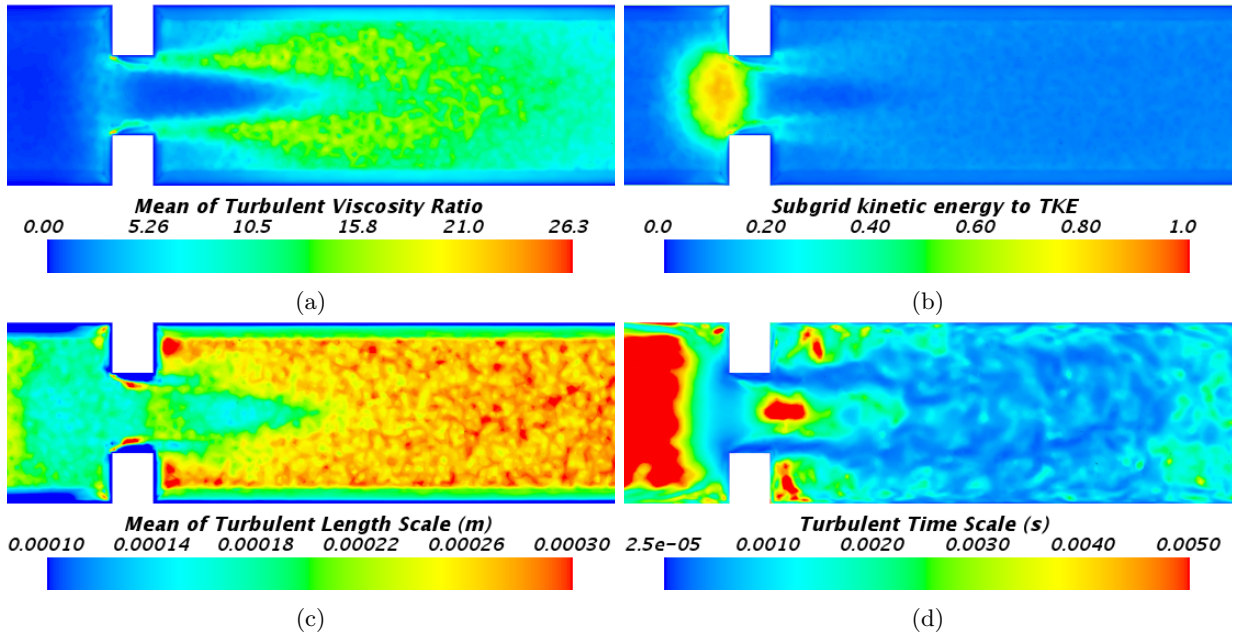


Figure 6.10: Results of LES performed on grid 8. a: The mean of the turbulent viscosity ratio, TVR . b: The TKE by the sugrid scale model to the resolved TKE, M_{TKE} . 6.10c: The mean of the turbulent length scale, $\bar{\ell}_0$. d: The instantaneous turbulent time scale, t_ℓ .

Time-averaged turbulent length scales are small just around the orifice as depicted in Figure 6.10c. $\bar{\ell}_0$ is already smaller than the filter width at some locations, let alone the smaller Taylor microscales. Therefore the cell sizes have to be reduced around the orifice, assuming that the presented length scales are simulated correctly. A snapshot of the instantaneous turbulent time scale, t_ℓ , shows that the chosen time step $\Delta t = 2.5 \times 10^{-5}$ s is small enough, see Figure 6.10d.

The flow field statistics obtained with LES are compared with 2D-PIV performed by Anantharaman (2014) ($Re \approx 10500$) in Figure 6.11. The fields are shown just downstream of the orifice till $z/D \approx 4$. The top figures compare mean velocity magnitude normalized with bulk velocity, which show a good

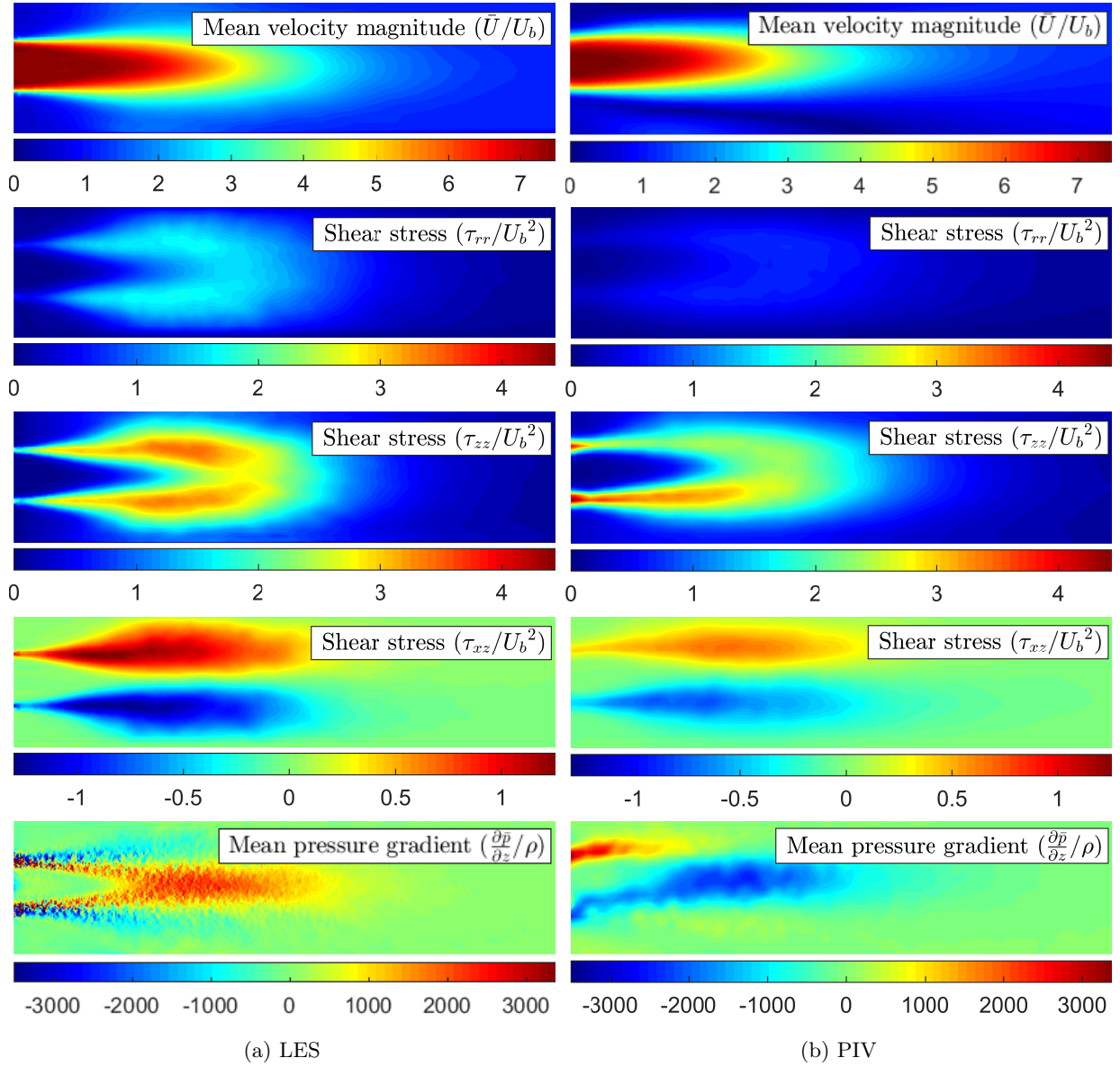


Figure 6.11: The field visualization of the mean velocity and the cross stream and axial fluid stresses normalized with respectively the friction velocity and friction velocity squared, and the static pressure gradient. a: LES on the finest grid ($Re = 10000$). b: PIV by Anantharaman (2014) ($Re \approx 10500$).

comparison. In the middle figures, fluid shear stresses in respectively rr -direction, zz -direction, and xz -direction normalized with bulk velocity squared are compared. The field shapes are similar, but LES simulates slightly higher stress values compared to PIV measurements. The bottom pictures in Figure 6.11 compare the mean pressure gradient in axial direction using

$$\frac{\partial \bar{p}}{\partial x_i} = -\bar{\rho} \bar{u}_j \frac{\partial \bar{u}_i}{\partial x_j} - \bar{\rho} \frac{\partial \overline{u'_i u'_j}}{\partial x_j} - \overline{u'_i u'_j} \frac{\partial \bar{\rho}}{\partial x_j} \quad (6.6)$$

as done by van Gent, van Oudheusden and Schrijer (2018). For incompressible flow the last term drops out and the field can be computed with central differencing using the Reynolds decomposition to determine the stress terms. Both results are different. It is recommended to redo the analysis using a first order accurate scheme at the boundary van Dijk and Krabben (2018). This is required as the resolution of the PIV-field is poor.

6.6 Conclusions

In the previous study flow characteristics in turbulent pipe flow including an orifice have been studied. Integral values of the mean pressure and the mean force are studied as well as the fluctuations of these. Additionally, velocity, pressure and force spectra are studied and compared with experiments, DNS and literature. Finally, flow fields are visualized to interpret the flow behavior. Based on the results that have been shown in this chapter the following conclusions are drawn

- The proposed recycling plane method is found suitable to generate turbulence at the inlet of a straight pipe including an orifice. It is therefore expected that it can be implemented for different geometries as well.
- Based on the region upstream of the orifice, the resolved one-dimensional energy spectra are concluded to be very dependent on the applied cell size. LES 8 is concluded to resolve straight pipe flow properly. In the orifice, the energy spectra are showing peaks at different frequencies for the different computational grids. It is concluded that the behavior cannot be directly contributed to one phenomenon and therefore might be physical or nonphysical. This requires additional research. If nonphysical, this might be due to the applied extruded part, the grid resolution, or orifice meshing. This peak content at high frequencies is concluded to have no significant effect on the flow behavior. Further, it is supposed that the turbulent structures in this region are better resolved for finer computational grids in line with the results found upstream of the orifice.
- The pressure drop is simulated properly for almost all LES based on values found in literature. The wall pressure fluctuations in the jet-wake region by LES are concluded to be slightly overpredicted comparing with experiments. The momentum balance is seen to be conserved based on the pressure drop fluctuations and orifice plate force fluctuations.
- In the jet-wake region the slopes of pressure spectra compare well with theoretical and experimental values. This is especially true for LES 8. Close to the orifice, the pressure spectra show a peak similarly as found in the energy spectra. This requires further research.
- The force spectrum is concluded to dominate the pressure spectra upstream of the orifice. Therefore the same conclusions are drawn as for the pressure spectra around the orifice. When neglecting the peak, the decay of the force spectrum shows a good match with a scaling law found in literature. Therefore, LES on grid 8 is assumed to give an accurate representation of the force spectrum by an orifice in bounded turbulent flow.
- Additionally, LES 8 meets the accuracy criteria and shows similar flow fields compared with PIV measurements. Therefore, the finest grid applied is found suitable to represent flow behavior on using LES.
- Analyzing time varying velocity field, the vortex rings are shed at a frequency of roughly 1000 Hz which corresponds to $St \approx 0.37$ based on the hole velocity and orifice thickness.

Chapter 7

Conclusions & Recommendations

This work basically consists of two parts to answer the proposed research questions. First literature is reviewed. Later on practical LES are performed to achieve the goal of this thesis. This goal is to determine the source term that disturbs bounded pipe flow.

7.1 Conclusions

From the literature review it is concluded that a couple of mechanisms contribute to the generation of acoustic noise. These are stretching vortices relative to the body, the separation of flow from the pipe wall, the shedding of vortex rings and the action of turbulence. From the sound generating sources, only the dipole term is found important. A monopole term only arises from bad pump behavior and mass injection or leakage, which is not the case. Quadrupole noise represents the noise generated by fluid shear stresses. This noise source is, however, only significant for Mach numbers in the neighbourhood of one or above. Mach number considered in this thesis are lower. Therefore, the only source term present in the current problem are dipoles which represent a fluctuating reaction force of a body to the fluid. From a review of literature it is concluded that this term cannot be measured easily. It is tried to determine the source term based on an analytical coupling with pressure measurements. This analytical solution estimates that large force fluctuations are required to generate noise elsewhere. These values are overestimated because free-field noise propagation was considered. Therefore performing incompressible Large Eddy Simulations is suggested.

LES results of straight pipe flow have shown that a recycling plane method is easiest and best to generate turbulence at the inlet of the domain. No accurate initial information is required and results have shown that the length to reach real turbulent pipe flow are shorter using this method. Therefore the domain length can be decreased. This decreases the simulation time which is beneficial. Only a domain extension of three pipe diameters is found sufficient to apply this method. Additionally, based on the results this method is concluded to be applicable to all kinds of geometries. With the design choices discussed in this work a LES setup is thus suggested which is suitable to study pipe flow.

Simulation results of turbulent pipe flow disturbed by an orifice agree can also be studied using this setup. Velocity and pressure results of LES are in accordance with literature, experiments and DNS. In the grid refinement study all results converged to the reference values. Therefore the LES on the finest grid is found to perform best. The captured source term is seen to be accurately simulated with LES on the finest grid showing a power spectral density shape equal to literature. The corresponding grid sizes are close to the Taylor microscales and therefore this is concluded to be a good length scale to base the grid size on. With this the proposed setup is found suitable to study the characteristics of the sound source. Simulations are performed within a week. So from this work it is concluded that the source term disturbing bounded flow can be determined with an acceptable accuracy using practical Large Eddy Simulations.

7.2 Recommendations

Based on the performed work a couple of recommendations are done. First of all the work achieved on the analytical solution of the source term has to be extended including proper boundary conditions. Afterwards, a predicted force spectrum based on measured acoustic pressure spectra should be compared with force spectra obtained with the performed LES.

Secondly, it is recommended to investigate the origin of content peaks in velocity, pressure and force spectra. The computational grid around the orifice has to be reviewed and a with that a possible link between the proposed grids and peak-frequencies should be investigated. To do so additional LES can be executed on very coarse grids. In that setup, the extruded part has to contain the same cell structures as in the domain of interest. If the peak behavior is nonphysical, this should give the required information. Physical peak behavior should be studied performing LES for different flow speeds and geometry dimensions. For this purpose the different flow structures should be studied simultaneously. The obtained data can be directly used to come up with a scaling law to determine the source term. When performing the LES, it is suggested to decrease the length of the computational domain upstream of the orifice to speed up the LES.

Last, the source term can be determined from velocity and vorticity fields. A complete description of this is given by Rienstra and Hirschberg (2001). It is recommended to compare the force spectra by this method with the force spectra given in this thesis.

References

- Adams, N. & Hickel, S. (2009). Implicit large-eddy simulation: Theory and application. In *Advances in turbulence xii* (pp. 743–750). Springer.
- Addad, Y., Gaitonde, U., Laurence, D. & Rolfo, S. (2008). Optimal unstructured meshing for large eddy simulations. In *Quality and reliability of large-eddy simulations* (pp. 93–103). Springer.
- Afzal, A., Ansari, Z., Faizabadi, A. R. & Ramis, M. (2017). Parallelization strategies for computational fluid dynamics software: state of the art review. *Archives of Computational Methods in Engineering*, *24*(2), 337–363.
- Agarwal, N. (1994a). The sound field in fully developed turbulent pipe flow due to internal flow separation, part 2: modal amplitude and cut-off frequencies. *Journal of sound and vibration*, *175*(1), 65–76.
- Agarwal, N. (1994b). The sound field in fully developed turbulent pipe flow due to internal flow separation, part i: Wall-pressure fluctuations. *Journal of sound and vibration*, *169*(1), 89–109.
- Aider, J.-L., Danet, A. & Lesieur, M. (2007). Large-eddy simulation applied to study the influence of upstream conditions on the time-dependant and averaged characteristics of a backward-facing step flow. *Journal of Turbulence*(8), N51.
- Alenius, E. (2012). *Flow duct acoustics: an les approach* (Unpublished doctoral dissertation). KTH Royal Institute of Technology.
- Alenius, E. (2014). Sound generating flow structures in a thick orifice plate jet. In *Progress in turbulence v* (pp. 201–204). Springer.
- Anantharaman, V. (2014). Characteristics of flow through orifices in pipes: an experimental investigation.
- Anantharaman, V., Waterson, N., Nakiboglu, G., Persin, M. & van Oudheusden, B. (2016). Experimental investigation of turbulent flow through single-hole orifice placed in a pipe by means of time-resolved particle image velocimetry and unsteady pressure measurements. In *11th international conference on flow-induced vibrations*.
- Anderson, A. (1955). Structure and velocity of the periodic vortex-ring flow pattern of a primary pfeifenton (pipe tone) jet. *The Journal of the Acoustical Society of America*, *27*(6), 1048–1053.
- Anderson, J. (2016). *Fundamentals of aerodynamics*. McGraw-Hill Education.
- ASML, N. W. (2020). *Data sets of inhouse performed experiments*. (unpublished)
- Atassi, P. H. M. (2020). *Teaching - fundamental solutions*. <https://www3.nd.edu/~atassi/Teaching/AME%2060633/Notes/fundamentals.w.pdf>. University of Notre Dame.
- Bakker, A. (2002). *Lecture 5 - solution methods: Applied computational fluid dynamics*. Fluent Inc.
- Bird, R. B., Stewart, W. E., Lightfoot, E. N. & Klingenberg, D. J. (2015). *Introductory transport phenomena*. Wiley Global Education.
- Blake, W. (1984). Aero-hydroacoustics for ships, vol. ii. *DTRC Report*, *84*(010).
- Blake, W. K. (1986). *Mechanics of flow-induced sound and vibration, volume 1: General concepts and elementary sources*. Academic press.
- Blasius, H. (1913). Das aehnlichkeitsgesetz bei reibungsvorgängen in flüssigkeiten. In *Mitteilungen über forschungsarbeiten auf dem gebiete des ingenieurwesens* (pp. 1–41). Springer.
- Blevins, R. (1979). Flow-induced vibration in nuclear reactors: a review. *Progress in Nuclear Energy*, *4*(1), 25–49.
- Blevins, R. D. (2001). *Flow-induced vibration, reprint edition*. Malabar, Florida: Krieger Publishing Company.
- Bull, M. & Agarwal, N. (1983). Characteristics of the flow separation due to an orifice plate in fully-developed turbulent pipe-flow. In *Proc. 8th australian fluid mechanics conference, university of newcastle, australia*.

- Bull, M. & Norton, M. (1981). On the hydrodynamic and acoustic wall pressure fluctuations in turbulent pipe flow due to a 90 mitred bend. *Journal of Sound and Vibration*, 76(4), 561–586.
- Bush, S. (1992). Failure mechanisms in nuclear power plant piping systems. *Journal of pressure vessel technology*, 114(4), 389–395.
- Cairns, C., Whitson, R., Strachan, P. & Wheel, M. (1970). Prediction of noise generated by orifice plates in liquid systems using a modified form of iec 534-8-4: 1994. *WIT Transactions on Engineering Sciences*, 29.
- Chaouat, B. (2017). The state of the art of hybrid rans/les modeling for the simulation of turbulent flows. *Flow, turbulence and combustion*, 99(2), 279–327.
- Chapman, D. R. (1979). Computational aerodynamics development and outlook. *AIAA journal*, 17(12), 1293–1313.
- Courant, R., Friedrichs, K. & Lewy, H. (1928). Über die partiellen differenzgleichungen der mathematischen physik. *Mathematische annalen*, 100(1), 32–74.
- Curle, N. (1955). The influence of solid boundaries upon aerodynamic sound. *Proceedings of the Royal Society of London. Series A. Mathematical and Physical Sciences*, 231(1187), 505–514.
- Den Toonder, J. & Nieuwstadt, F. (1997). Reynolds number effects in a turbulent pipe flow for low to moderate re. *Physics of Fluids*, 9(11), 3398–3409.
- Dhamankar, N. S., Blaisdell, G. A. & Lyrintzis, A. S. (2017). Overview of turbulent inflow boundary conditions for large-eddy simulations. *Aiaa Journal*, 56(4), 1317–1334.
- Dhamankar, N. S., Blaisdell, G. A. & Lyrintzis, A. S. (2018). Overview of turbulent inflow boundary conditions for large-eddy simulations. *Aiaa Journal*, 56(4), 1317–1334.
- Ebrahimi, B., He, G., Tang, Y., Franchek, M., Liu, D., Pickett, J., . . . Franklin, D. (2017). Characterization of high-pressure cavitating flow through a thick orifice plate in a pipe of constant cross section. *International Journal of Thermal Sciences*, 114, 229–240.
- El Khoury, G. K., Schlatter, P., Noorani, A., Fischer, P. F., Brethouwer, G. & Johansson, A. V. (2013). Direct numerical simulation of turbulent pipe flow at moderately high reynolds numbers. *Flow, turbulence and combustion*, 91(3), 475–495.
- Fernandez, P., Nguyen, C., Roca, X. & Peraire, J. (2016). Implicit large-eddy simulation of compressible flows using the interior embedded discontinuous galerkin method. In *54th aiaa aerospace sciences meeting* (p. 1332).
- Fureby, C. & Grinstein, F. (1999). Monotonically integrated large eddy simulation of free shear flows. *AIAA journal*, 37(5), 544–556.
- George, W. K., Beuther, P. D. & Arndt, R. E. (1984). Pressure spectra in turbulent free shear flows. *Journal of Fluid Mechanics*, 148, 155–191.
- Heenan, A. & Morrison, J. (1998). Passive control of pressure fluctuations generated by separated flow. *AIAA journal*, 36(6), 1014–1022.
- Hill, R. J. & Wilczak, J. M. (1995). Pressure structure functions and spectra for locally isotropic turbulence. *Journal of Fluid Mechanics*, 296, 247–269.
- Hirschberg, A. (2007). Introduction to aero-acoustics of internal flows. In *Basics of aeroacoustics and thermoacoustics* (pp. 1–112). Von Karman Institute for Fluid Dynamics.
- Howe, M. S. (2003). *Theory of vortex sound* (Vol. 33). Cambridge University Press.
- Idelchik, I. E. (1986). Handbook of hydraulic resistance. *Washington, DC, Hemisphere Publishing Corp.*, 1986, 662 p. *Translation.*
- Jarrin, N., Benhamadouche, S., Laurence, D. & Prosser, R. (2006). A synthetic-eddy-method for generating inflow conditions for large-eddy simulations. *International Journal of Heat and Fluid Flow*, 27(4), 585–593.
- Junger, M. C. & Feit, D. (1986). *Sound, structures, and their interaction* (Vol. 225). MIT press Cambridge, MA.
- Kao, D., Graham, D., Knight, B. & Pericleous, K. (2007). A mathematical description of the acoustic coupling of the mass/spring model. *Applied mathematical modelling*, 31(12), 2684–2695.
- Keating, A., Piomelli, U., Balaras, E. & Kaltenbach, H.-J. (2004). A priori and a posteriori tests of inflow conditions for large-eddy simulation. *Physics of fluids*, 16(12), 4696–4712.
- Kemper, N. (2014). Pir low dynamics - acceleration induced disturbances..
- Kolmogorov, A. N. (1941). The local structure of turbulence in incompressible viscous fluid for very large reynolds numbers. *Cr Acad. Sci. URSS*, 30, 301–305.
- Kottapalli, S. (2020). Pressure and velocity fluctuations in an orifice flow: Experiments and les. *Journal of Fluid Mechanics*.

- Kundu, P. K., Dowling, D. R., Tryggvason, G. & Cohen, I. M. (2015). Fluid mechanics.
- Lacombe, R., Moussou, P. & Aurégan, Y. (2011). Whistling of an orifice in a reverberating duct at low mach number. *The Journal of the Acoustical Society of America*, 130(5), 2662–2672.
- Lacombe, R., Moussou, P., Föller, S., Jasor, G., Polifke, W. & Aurégan, Y. (2010). Experimental and numerical investigations on the whistling ability of an orifice in a flow duct. *exergy*, 2, 1.
- Launder, B. E. & Spalding, D. B. (1983). The numerical computation of turbulent flows. In *Numerical prediction of flow, heat transfer, turbulence and combustion* (pp. 96–116). Elsevier.
- Lee, M. & Moser, R. D. (2015). Direct numerical simulation of turbulent channel flow up to $re_\tau \approx 5200$. *Journal of Fluid Mechanics*, 774, 395–415.
- Lighthill, M. J. (1952). On sound generated aerodynamically i. general theory. *Proceedings of the Royal Society of London. Series A. Mathematical and Physical Sciences*, 211(1107), 564–587.
- Michalke, A. (1989). On the propagation of sound generated in a pipe of circular cross-section with uniform mean flow. *Journal of Sound and Vibration*, 134(2), 203–234.
- Moussou, P. (2006). An attempt to scale the vibrations of water pipes. *Journal of pressure vessel technology*, 128(4), 670–676.
- Moussou, P., Lafon, P., Potapov, S., Paulhiac, L. & Tijsseling, A. (2004). Industrial cases of fsi due to internal flows. In *Proc. of the 9th int. conf. on pressure surges* (Vol. 1, pp. 13–31).
- Moussou, P., Testud, P., Hirschberg, A. et al. (2007). An acoustic criterion for the whistling of orifices in pipes. In *Asme 2007 pressure vessels and piping conference* (pp. 345–353).
- Nicoud, F. & Ducros, F. (1999). Subgrid-scale stress modelling based on the square of the velocity gradient tensor. *Flow, turbulence and Combustion*, 62(3), 183–200.
- Piellard, M. & Bailly, C. (2010). Several computational aeroacoustics solutions for the ducted diaphragm at low mach number. In *16th aiaa/ceas aeroacoustics conference* (p. 3996).
- Pope, S. B. (2001). *Turbulent flows*. IOP Publishing.
- Pope, S. B. (2004). Ten questions concerning the large-eddy simulation of turbulent flows. *New journal of Physics*, 6(1), 35.
- Qing, M., Jinghui, Z., Yushan, L., Haijun, W. & Quan, D. (2006). Experimental studies of orifice-induced wall pressure fluctuations and pipe vibration. *International journal of pressure vessels and piping*, 83(7), 505–511.
- Richardson, L. F. (1922). Weather prediction by numerical process cambridge university press. *Cambridge Richardson Weather prediction by numerical process, 1922*.
- Rienstra, S. W. & Hirschberg, A. (2001). An introduction to acoustics. *Report IWDE*, 92–06.
- Russo, F. & Basse, N. T. (2016). Scaling of turbulence intensity for low-speed flow in smooth pipes. *Flow Measurement and Instrumentation*, 52, 101–114.
- Rütten, F., Meinke, M. & Schröder, W. (2001). Large-eddy simulations of 90-pipe bend flows. *J. Turbul*, 2(003).
- Salim, S. M. & Cheah, S. (2009). Wall y strategy for dealing with wall-bounded turbulent flows. In *Proceedings of the international multiconference of engineers and computer scientists* (Vol. 2, pp. 2165–2170).
- Santana, D. L. D. (2019, February). *Basic concepts of aeroacoustics*. University of Twente.
- Schram, C. (2009). A boundary element extension of curle’s analogy for non-compact geometries at low-mach numbers. *Journal of Sound and Vibration*, 322(1-2), 264–281.
- Schram, C., Anthoine, J. & Hirschberg, A. (2005). Calculation of sound scattering using curle’s analogy for non-compact bodies. In *11th aiaa/ceas aeroacoustics conference* (p. 2836).
- Selvam, K., Öngüner, E., Peixinho, J., Zanon, E.-S. & Egbers, C. (2018). Wall pressure in developing turbulent pipe flows. *Journal of Fluids Engineering*, 140(8), 081203.
- Spazzini, P., Iuso, G., Onorato, M., Zurlo, N. & Di Cicca, G. (2001). Unsteady behavior of back-facing step flow. *Experiments in fluids*, 30(5), 551–561.
- Speziale, C. (1998). Turbulence modeling for time-dependent rans and vles: a review. *AIAA journal*, 36(2), 173–184.
- STAR-CCM+. (2018). Star ccm+ user guide version 13.06. *CD-Adapco: New York, NY, USA*.
- StevePortal. (2019a). *Discussion on numerical diffusion: Poly vs. trimmed*. Retrieved 2019-11-26, from https://thesteveportal.plm.automation.siemens.com/articles/en_US/FAQ/Discussion-on-numerical-diffusion-Poly-vs-Trimmed
- StevePortal. (2019b). *Do i need prism layers? how many should i use?* Retrieved 2019-11-26, from https://thesteveportal.plm.automation.siemens.com/articles/en_US/FAQ/AR-4-255
- StevePortal. (2019c). *How can i generate a flow aligned mesh? can a polyhedral mesh be aligned?* Retrieved

- 2019-11-26, from https://thesteveportal.plm.automation.siemens.com/articles/en_US/FAQ/NP-4-377
- StevePortal. (2019d). *How to calculate turbulent kinetic energy in les*. Retrieved 2020-01-08, from https://thesteveportal.plm.automation.siemens.com/articles/en_US/FAQ/How-to-calculate-Turbulent-Kinetic-Energy-in-LES
- StevePortal. (2019e). *What is the benefit of a polyhedral mesh*. Retrieved 2019-12-16, from https://thesteveportal.plm.automation.siemens.com/articles/en_US/FAQ/JC-4-332
- Tao, F., Joseph, P., Zhang, X., Stalnov, O., Siercke, M. & Scheel, H. (2017). Investigation of the sound generation mechanisms for in-duct orifice plates. *The Journal of the Acoustical Society of America*, *142*(2), 561–572.
- Taylor, G. I. (1938). The spectrum of turbulence. *Proceedings of the Royal Society of London. Series A-Mathematical and Physical Sciences*, *164*(919), 476–490.
- Testud, P., Aurégan, Y., Moussou, P. & Hirschberg, A. (2009). The whistling potentiality of an orifice in a confined flow using an energetic criterion. *Journal of Sound and Vibration*, *325*(4-5), 769–780.
- Testud, P., Moussou, P., Hirschberg, A. & Aurégan, Y. (2007). Noise generated by cavitating single-hole and multi-hole orifices in a water pipe. *Journal of fluids and structures*, *23*(2), 163–189.
- Tsuji, Y. & Kaneda, Y. (2012). Anisotropic pressure correlation spectra in turbulent shear flow. *Journal of fluid mechanics*, *694*, 50–77.
- Tucker, P. G. (2016). *Advanced computational fluid and aerodynamics* (Vol. 54). Cambridge University Press.
- Tullis, J. P. (1989). *Hydraulics of pipelines: Pumps, valves, cavitation, transients*. John Wiley & Sons.
- Van der Weide, E. (2018). Dcretization schemes for hyperbolic partial differential equations..
- Van der Zande, M. J. (2000). Droplet break-up in turbulent oil-in-water flow through a restriction.
- van Dijk, J. & Krabben, I. (2018). Computational fluid dynamics assignment portfolio..
- van Gent, P. L., van Oudheusden, B. W. & Schrijer, F. F. (2018). Determination of mean pressure from piv in compressible flows using the reynolds-averaging approach. *Experiments in Fluids*, *59*(3), 41.
- Wagner, C., Hüttl, T. & Sagaut, P. (2007). *Large-eddy simulation for acoustics* (Vol. 20). Cambridge University Press.
- Waterson, N. P. & Deconinck, H. (2007). Design principles for bounded higher-order convection schemes—a unified approach. *Journal of Computational Physics*, *224*(1), 182–207.
- Welch, P. (1967). The use of fast fourier transform for the estimation of power spectra: a method based on time averaging over short, modified periodograms. *IEEE Transactions on audio and electroacoustics*, *15*(2), 70–73.
- Zhao, S., Cheng, E., Qiu, X., Burnett, I. & Liu, J. C.-c. (2016). Pressure spectra in turbulent flows in the inertial and the dissipation ranges. *The Journal of the Acoustical Society of America*, *140*(6), 4178–4182.

Appendix A

Coupling with Theory

In this appendix, Curle's analogy in integral form is worked out, given in Equation 2.38. First, the route to this expression is given, explaining why an additional source term is present in the vicinity of solid bodies (Curle (1955)). Additionally, assumptions and conditions are listed. In order to do so, the non homogeneous wave equation, or Lighthill's equation, see Chapter 2.6.1, is started with

$$\frac{\partial^2 \rho}{\partial t^2} - c_0^2 \frac{\partial^2 \rho}{\partial x_i \partial x_i} = \frac{\partial^2 T_{ij}}{\partial x_i \partial x_j} \quad (\text{A.1})$$

Green's function, $G(\mathbf{x}, t | \mathbf{y}, \tau)$, can be used to solve differential equations of the form

$$Lu(x) = f(x) \quad (\text{A.2})$$

In here, L is an differential operator. A property of Green's function is that it satisfies

$$LG(x, s) = \delta(s - x) \quad (\text{A.3})$$

Assuming that Green's function also satisfies the wave equation, results in

$$\frac{\partial^2 G}{\partial \tau^2} - c_0^2 \frac{\partial^2 G}{\partial y_i^2} = \delta(\mathbf{x} - \mathbf{y})\delta(t - \tau) \quad (\text{A.4})$$

τ is the source time and $\mathbf{x} - \mathbf{y}$ is the distance between source and observer. Now Lighthill's equation is rewritten such that $\rho' c_0^2$ appears everywhere. As done obtaining the wave equation, multiplying Lighthill's equation with Green's function and multiplying Equation A.4 with $\rho' c_0^2$ results in both

$$\left(\frac{1}{c_0^2} \frac{\partial^2 (\rho' c_0^2)}{\partial \tau^2} - \frac{\partial^2 (\rho' c_0^2)}{\partial y_i^2} = \frac{\partial^2 T_{ij}}{\partial y_i \partial y_j} \right) \cdot G \quad (\text{A.5})$$

$$\left(\frac{1}{c_0^2} \frac{\partial^2 G}{\partial \tau^2} - \frac{\partial^2 G}{\partial y_i^2} = \delta(\mathbf{x} - \mathbf{y})\delta(t - \tau) \right) \cdot \rho' c_0^2 \quad (\text{A.6})$$

Subtracting the first from the second results in

$$\delta(\mathbf{x} - \mathbf{y})\delta(t - \tau)\rho' c_0^2 - \frac{\partial^2 T_{ij}(\mathbf{y}, \tau)}{\partial y_i \partial y_j} G = \frac{1}{c_0^2} \left(\rho' c_0^2 \frac{\partial^2 G}{\partial \tau^2} - G \frac{\partial^2 (\rho' c_0^2)}{\partial \tau^2} \right) - \left(\rho' c_0^2 \frac{\partial^2 G}{\partial y_i^2} - G \frac{\partial^2 (\rho' c_0^2)}{\partial y_i^2} \right) \quad (\text{A.7})$$

Note that the fluctuations of pressure (or density) are now regarded. Now this expression can be integrated with respect to \mathbf{y} over volume V and with respect to τ between $t = -T$ and $t = T$. After rewriting, the density field for a observer at a certain time is given as

$$\begin{aligned} \rho'(\mathbf{x}, t)c_0^2 = & \int_{-T}^T \iiint_V \frac{\partial^2 T_{ij}(\mathbf{y}, \tau)}{\partial y_i \partial y_j} G d^3 \mathbf{y} d\tau + \int_{-T}^T \iiint_V \frac{1}{c_0^2} \left[\rho(\mathbf{y}, \tau)' c_0^2 \frac{\partial^2 G}{\partial \tau^2} - G \frac{\partial^2 (\rho(\mathbf{y}, \tau)' c_0^2)}{\partial \tau^2} \right] d^3 \mathbf{y} d\tau \\ & - \int_{-T}^T \iiint_V \left[\rho(\mathbf{y}, \tau)' c_0^2 \frac{\partial^2 G}{\partial y_i^2} - G \frac{\partial^2 (\rho(\mathbf{y}, \tau)' c_0^2)}{\partial y_i^2} \right] d^3 \mathbf{y} d\tau \end{aligned} \quad (\text{A.8})$$

Note that integrating the Dirac delta function, δ , over a distance equals one. Using Gauss's divergence theorem results in

$$\begin{aligned} \rho'(\mathbf{x}, t)c_0^2 = & \int_{-T}^T \iiint_V \frac{\partial^2 T_{ij}(\mathbf{y}, \tau)}{\partial y_i \partial y_j} G d^3 \mathbf{y} d\tau + \int_{-T}^T \iint_{\partial V} \left[\rho(\mathbf{y}, \tau)' c_0^2 \frac{\partial^2 G}{\partial y_i^2} - G \frac{\partial^2 (\rho(\mathbf{y}, \tau)' c_0^2)}{\partial y_i^2} \right] n_i d^2 \mathbf{y} d\tau \\ & - \left[\iiint_V \frac{1}{c_0^2} \left[\rho(\mathbf{y}, \tau)' c_0^2 \frac{\partial G^2}{\partial \tau^2} - G \frac{\partial^2 (\rho(\mathbf{y}, \tau)' c_0^2)}{\partial \tau^2} \right] d^3 \mathbf{y} \right]_{\tau=-T} \end{aligned} \quad (\text{A.9})$$

According to (Rienstra and Hirschberg (2001)) the initial condition term drops out if T is large enough. This results in a volume and surface integral. The volumetric source is rewritten using Gauss's divergence theorem and following Curle's Doak approach (Santana (2019)). The volumetric term is rewritten to

$$\begin{aligned} \int_{-T}^T \iiint_V \frac{\partial^2 T_{ij}(\mathbf{y}, \tau)}{\partial y_i \partial y_j} G d^3 \mathbf{y} d\tau = & \int_{-T}^T \iiint_V T_{ij} \frac{\partial^2 G}{\partial y_i \partial y_j} d^3 \mathbf{y} d\tau \\ & + \int_{-T}^T \iint_{\partial V} \left[T_{ij}(\mathbf{y}, \tau) \frac{\partial G}{\partial y_i} - G \frac{\partial T_{ij}(\mathbf{y}, \tau)}{\partial y_i} \right] n_i d^2 \mathbf{y} d\tau \end{aligned} \quad (\text{A.10})$$

Substituting Equation A.10 into Equation A.9 and grouping terms gives

$$\begin{aligned} \rho'(\mathbf{x}, t)c_0^2 = & \int_{-T}^T \iint_{\partial V} \left[(\rho(\mathbf{y}, \tau)' c_0^2 \delta_{ij} + T_{ij}) \frac{\partial G}{\partial y_i} - G \frac{\partial (\rho(\mathbf{y}, \tau)' c_0^2 \delta_{ij} + T_{ij})}{\partial y_i} \right] n_j d^2 \mathbf{y} d\tau \\ & + \int_{-T}^T \iiint_V \frac{\partial^2 G}{\partial y_i \partial y_j} T_{ij}(\mathbf{y}, \tau) d^3 \mathbf{y} d\tau \end{aligned} \quad (\text{A.11})$$

Implementation of the Lighthill stress tensor, see Equation 2.30, into the surface integral leads to

$$\begin{aligned} \rho'(\mathbf{x}, t)c_0^2 = & \int_{-T}^T \iint_{\partial V} \left[(\rho u_i u_j + \sigma_{ij}) \frac{\partial G}{\partial y_i} - G \frac{\partial (\rho u_i u_j + \sigma_{ij})}{\partial y_i} \right] n_j d^2 \mathbf{y} d\tau \\ & + \int_{-T}^T \iiint_V \frac{\partial^2 G}{\partial y_i \partial y_j} T_{ij}(\mathbf{y}, \tau) d^3 \mathbf{y} d\tau \end{aligned} \quad (\text{A.12})$$

Now

$$\frac{\partial}{\partial y_j} (\rho u_i u_j + \sigma_{ij}) n_j = - \frac{\partial}{\partial \tau} (\rho u_i) \quad (\text{A.13})$$

Due to the reciprocity theorem

$$\frac{\partial G_0}{\partial y_i} = - \frac{\partial G_0}{\partial x_i}, \quad \frac{\partial^2 G_0}{\partial y_i \partial y_j} = \frac{\partial G_0}{\partial x_i \partial x_j} \quad (\text{A.14})$$

Equation A.12 is rewritten to the form

$$\begin{aligned} \rho'(\mathbf{x}, t)c_0^2 = & - \frac{\partial}{\partial x_i} \int_{-T}^T \iint_{\partial V} (\rho u_i u_j + \sigma_{ij}) G_0 n_j d^2 \mathbf{y} d\tau + \int_{-T}^T \iint_{\partial V} \frac{\partial (\rho u_j)}{\partial \tau} G_0 n_j d^2 \mathbf{y} d\tau \\ & + \frac{\partial^2}{\partial x_i \partial x_j} \int_{-T}^T \iiint_V T_{ij}(\mathbf{y}, \tau) G_0 d^3 \mathbf{y} d\tau \end{aligned} \quad (\text{A.15})$$

In here the free-field Green's function is defined as

$$G_0(\mathbf{x}, t | \mathbf{y}, \tau) = \frac{\delta(t - |\mathbf{x} - \mathbf{y}|/c_0 - \tau)}{4\pi |\mathbf{x} - \mathbf{y}|} \quad (\text{A.16})$$

The contribution of the monopole, dipole and quadrupole are already recognized in Equation A.15. If each surface is fixed or vibrating in its own plane and additionally impermeable, then

$$u_i n_i \equiv 0 \quad (\text{A.17})$$

This means that the second surface integral in Equation A.15 drops out. In other words, if there is no mass injection, the surface integral representing the monopole drops out. Obviously only at the time the sources are active, the source terms contribute to the density field. The source time is defined as the observer time minus the time a wave needs to travel from the source to the observer

$$\tau = t - |\mathbf{x} - \mathbf{y}|/c_0 \quad (\text{A.18})$$

Applying this to Green's function, it returns only one if the difference between the source time and the recalculated source time from the observer its perspective is zero. Evaluating the integral therefore leads to the density field

$$\rho'(\mathbf{x}, t)c_0^2 = -\frac{\partial}{\partial x_i} \iint_{\partial V} [\rho u_i u_j + \sigma_{ij}]_\tau \frac{n_j d^2 \mathbf{y}}{4\pi |\mathbf{x} - \mathbf{y}|} + \frac{\partial^2}{\partial x_i \partial x_j} \iiint_V [T_{ij}(\mathbf{y}, \tau)]_\tau \frac{d^3 \mathbf{y}}{4\pi |\mathbf{x} - \mathbf{y}|} \quad (\text{A.19})$$

Equation A.19 is the fundamental result of Curle as already given in Chapter 2.7. However, as mentioned, this expression is not very useful in this form. As described in Chapter 2.6.3, quadrupoles are playing a minor role in specific cases. Continuing with the exact expression assuming quadrupoles can be neglected leads to

$$\rho'(\mathbf{x}, t)c_0^2 = -\frac{\partial}{\partial x_i} \iint_{\partial V} [\rho u_i u_j + \sigma_{ij}]_\tau \frac{n_j d^2 \mathbf{y}}{4\pi |\mathbf{x} - \mathbf{y}|} \quad (\text{A.20})$$

Applying the next chain rule

$$\frac{\partial F(\tau)}{\partial x_i} = \frac{\partial \tau}{\partial x_i} \left[\frac{\partial F(\tau)}{\partial \tau} \right]_\tau \quad (\text{A.21})$$

In this expression, $\partial \tau / \partial x_i$ can be defined as

$$\frac{\partial \tau}{\partial x_i} = -\frac{(x_i - y_i)}{|\mathbf{x} - \mathbf{y}|c_0} = -\frac{\cos(\theta)}{c_0} \quad (\text{A.22})$$

Those terms are typical for dipole sound behavior. Applying the chain rule to Equation A.20 results in

$$\rho'(\mathbf{x}, t)c_0^2 = \iint_{\partial V} \left[\frac{\rho u_i u_j + \sigma_{ij}}{\partial \tau} + \frac{(\rho u_i u_j + p_{ij})c_0}{|\mathbf{x} - \mathbf{y}|} \right]_\tau \frac{n_j \cos(\theta) d^2 \mathbf{y}}{4\pi |\mathbf{x} - \mathbf{y}|c_0} \quad (\text{A.23})$$

Assuming low speeds, the momentum terms drop out. Additionally the net force applied by the surface to the fluid is

$$F_i(\tau) = \iint_{\partial V} \sigma_{ij} n_j d^2 \mathbf{y} \quad (\text{A.24})$$

Therefore the final approximation to Curle's exact analogy reads

$$\rho'(\mathbf{x}, t)c_0^2 = \left[\frac{\partial F_i(\tau)}{\partial \tau} + \frac{F_i(\tau)c_0}{|\mathbf{x} - \mathbf{y}|} \right]_\tau \frac{\cos(\theta)}{4\pi |\mathbf{x} - \mathbf{y}|c_0} \quad (\text{A.25})$$

This expression is not found often in literature, see for example (Atassi (2020)). Most of time the second term between brackets is not included as this term becomes less important for large distances between source and observer ($\mathbf{x} - \mathbf{y}$).

A.1 Discretization

Equation A.25 provides a coupling between of the fluctuation part of the pressure and the fluctuating force in time. In order to calculate the one signal from the other, this expression has to be discretized. Using one sided difference this derivative can be expressed. As the force is mainly pointing perpendicular to the orifice plate, which is in flow direction, $i = 1$. Index j is introduced for indexing the signal. The direction interested in is $\cos(\theta) = 1$, see Figure 2.5b. This results in

$$\rho'(\mathbf{x}, t)c_0^2 = \left[\frac{\partial F_i(\tau)}{\partial \tau} + \frac{F_i(\tau)c_0}{r} \right]_\tau \frac{1}{4\pi r c_0} \quad (\text{A.26})$$

Rewriting results in

$$p' = \left[\frac{1}{rc_0} \frac{\partial F_i(\tau)}{\partial \tau} + \frac{F_i(\tau)}{r^2} \right] \frac{1}{4\pi} \quad (\text{A.27})$$

Using one sided differencing to discretize the derivative results in

$$p'_j = \left[\frac{1}{rc_0} \frac{F(t_j - r/c_0) - F(t_{j-1} - r/c_0)}{\Delta t} + \frac{F(t_j - r/c_0)}{r^2} \right] \frac{1}{4\pi} \quad (\text{A.28})$$

Regrouping results in

$$p'_j 4\pi = F(t_j - r/c_0) \left(\frac{1}{rc_0 \Delta t} + \frac{1}{r^2} \right) - F(t_{j-1} - r/c_0) \frac{1}{rc_0 \Delta t} \quad (\text{A.29})$$

Rewriting results in

$$F(t_j - r/c_0) = \left(p'_j 4\pi + F(t_{j-1} - r/c_0) \frac{1}{rc_0 \Delta t} \right) / \left(\frac{1}{rc_0 \Delta t} + \frac{1}{r^2} \right) \quad (\text{A.30})$$

The solution can be initialized using a moderate value for the force.

Appendix B

Simulation Setup Steps STAR-CCM+

In this appendix a general full simulation setup procedure is enumerated to re-do RANS simulations and/or LES performed in this thesis.

B.1 Geometry/Continuum/Region

1. Open new file.
2. Create a new 3D-CAD model under **Geometry > 3D-CAD Models**. Sketch the region of interest. Rename the surfaces to inlet, outlet, pipe wall etc. Update and close the 3D-CAD model.
3. Right click the created 3D-CAD model and click **New Geometry Part** and continue using default settings. Rename this created part to Fluid Part under **Parts**.
4. Then assign this part to a region by right-clicking the created part. Select **Create a Boundary for Each Part Surface** and continue. Rename the region to Fluid Region under **Regions**. Change the boundary types in the region. The inlet is typically a velocity inlet and the outlet is a pressure outlet. The pipe wall is just a wall already by default.
5. The region needs a physics continuum. Under **Continua** create a new physics continuum. Rename to either LES or RANS continuum depending on the simulation technique to be used. If both techniques will be used, for example using RANS to initialize LES, then just create two continua. Depending on the technique, select the following models in this continuum: Three Dimensional, Implicit Unsteady, Liquid, Segregated Flow, Constant Density, Turbulent, Large Eddy Simulation. Keep the automatically selected models. The automatically selected models are: Gradients, WALE Subgrid Scale, Exact Wall Distance, and All $y+$ Wall Treatment.
6. In these models change the material properties of the medium under **Liquid** to that of water at the temperature of interest. When intentionally central differencing is desired to be used, lower the upwind blending factor under the **Segregated Flow** model. For Implicit LES, the C_w value under the **WALE Subgrid Scale** model has to be lowered.
7. The region additionally needs a mesh. Create a new Automated Mesh operation under **Geometry > Operations > New > Automated Mesh**. Select the part of interest and the following meshers: Polyhedral Mesher, Surface Remesher, and Advancing Layer Mesher. Please note that sometimes the Prism Layer Mesher is also sufficient.
8. In this automated Mesh, change the **Base Size**, **Surface Growth Rate**, **Number of Prism Layers**, **Prism Layer Stretching**, and **Prism Layer Total Thickness**. If specific faces require different values of above parameters, a new specific surface control can be created under **Operations > Automated Mesh > Custom Controls**.

9. Execute the created mesher under **Mesh > Generate Volume Mesh**.
10. Run a full mesh analysis under **Mesh > Diagnostics**. Select the region and report type full and check the cell skewness ($< 85^\circ$) and minimum face validity (>1). Additionally, always judge the quality of the mesh by visualizing for example the inlet/outlet creating a scene of the mesh.

B.2 Initialization/Boundary conditions

1. Change the maximal number of eddies to at least 1000000 under **Continua > "Physics Continuum" > Reference Values > Maximum Number of Eddies**.
2. Specify under **Continua > "Physics Continuum" > Initial Conditions** the pressure and velocity field using average fields of a precursor simulation. Specify turbulence by selecting Intensity + Length Scale under Synthetic Turbulence Specification. Also specify those using average fields of a precursor simulation. If this is not possible, give constant values. If the solution converges this is no problem, but eliminating the initials will take more time.
3. Under **Regions > "Region" > Boundaries > "Inlet"** change the boundary conditions of the inlet. In case of using the Synthetic Eddy Method for specifying turbulence, the method under **Synthetic Turbulence Specification** has to be set to **Intensity + Length Scale**. Also enable **Mass Flow Scaling** under **Synthetic Turbulence Mass Flow Scaling Specification**. Then set the **Physics Values** of the Intensity, Length Scale and Velocity at the inlet by importing cross sectional fields of a precursor simulation and provide them using tables. If the recycling plane method will be applied, follow the steps in Appendix B.3.

B.3 Data mapping

In order to create a fully developed profile at the inlet of the geometry of investigation, fully developed data can be mapped onto this inlet boundary plane. An extra part has to be created over which fully developed conditions are obtained. The procedure is as follows:

1. Extend the already created part at the inlet side under **Geometry > Operations > New > Surface Preparation > Surface Extruder**. Select the already existing part and inlet surface part. Under **Output Part Surfaces** select **Single Side**. Change the **Extrusion Distance** and enable both options **Create Volume Extruder Operation From Output Parts** and **Execute Surface Extruder Operation Upon Creation**.
2. Assign the new Surface Extruder part to the already existing region. This procedure is the same as done before, but select the setting **Assign All Parts to an Existing Region** in the **Assign Parts to Regions** menu and select the region. Again **Create a Boundary for Each Part Surface**. In the bottom drop down menu select **Do Not Create Interfaces From Contracts** as data will be mapped from the one surface to the other. Then continue.
3. Under **Regions > "Region" > Boundaries** set the boundary types of the extruded part to again a velocity inlet and a pressure outlet. Also rename the surfaces.
4. Create a fully developed interface using the inlet and outlet of the extruded part selecting both boundaries and click **Create Interface**.
5. Under **Interfaces** rename the created interface and change the type to Fully-Developed Interface. Under **Interfaces > "Interface" > Physics Conditions > Fully Developed Flow option** select **Mass Flow Rate**. Set this value under **Physics Values**.
6. Create a new Data Mapper under **Tools > Data Mappers > New Data Mapper > Surface Data Mapper**. Select the outlet of the extruded part (not interface) as **Source Surface** of the Surface Data Mapper. Select Velocity as the vector field function. Then under **Target Specifications > "Surface"** select the inlet of the region of interest as the target entity. Then under **Update** enable this data mapper and select **Time Step** as the trigger for it. Please note that the surfaces of the region have to be selected instead of the part surfaces.

7. Run the mesher again under **Mesh > Generate Volume Mesh**.
8. The newly created field functions, probably called MappedVertexVelocity, have to be used to assign the physics values to the velocity inlet of the original part. To do so, change the **Synthetic Turbulence Specification** method to **None** under **Regions > "Region" > Boundaries > "Inlet" > Physics Conditions >** and change the **Velocity Specification** to components. Under **Physics Values** now the velocity is provided by a field function selecting the vector function MappedVertexVelocity.

B.4 Solver

1. Under **Solvers > Implicit Unsteady** change the time step and the temporal discretization. Most likely **2nd-order** is chosen.
2. Under **Solvers > Segregated Flow** change the Under-Relaxation Factor of Velocity and Pressure. Additionally, if stability allows, choose **Optimized 2nd-order (5)** under **High-Accuracy Temporal Discretization**.
3. Under **Stopping Criteria** the number of inner iterations and physical time can be specified.

B.5 Derived parts/Report/Monitor

Derived parts have to be created to display or monitor results. This, however, is a matter of choice and is therefore less strictly listed.

1. Plane sections can be created under **Derived Parts > New Part > Section > Plane**. Likely, cross sectional planes are to be created at every diameter in axial direction downstream of the inlet. Additionally, a cross section in axial direction is helpful.
2. Additionally create point probes in cross sectional direction to capture profile data. A general tip is to open for example a mesh scene and then create new derived parts, **Edit in Current Scene**. This gives additional options such as snapping the derived parts to parts. Another tip is to select besides the region, also the surfaces of the part as input parts. If not, it might be that field values cannot be captured by the derived parts.
3. To collect for example wall pressure data, point probes are to be created. For wall probes it is very important to snap them to the pipe wall of the part.
4. To avoid repetitive work, **Macros** can be used to generate a lot of derived parts, as well as reports, monitors and result tables. To do so, first start recording by clicking the **blue dot in the toolbar**. Then create a derived part as described above. Then stop the recording and save the macro. Opening the macro with a text editor gives the option to adjust the macro and therefore automate the creation of for example derived parts. Apply for loops in the style of JavaScript.
5. Report can be created under **Reports**. To get point data, a maximum report should be created.
6. To get the data as a function of iteration or timestep, a monitor should be created from the report. This is done by right-clicking the report and clicking **Create Monitor from Report**. Data can be exported after a simulation by right-clicking the monitor and clicking **Export**.
7. Data of line probes can be exported using tables under **Tools > Tables > New Table > XYZ Internal Table**. The right scalar and derived parts should be selected. Additionally, the **Data on Vertices** option should be enabled.
8. To get the mean or variance values in time of quantities, a monitor should be created. Under **Monitor > New Monitor** both a field max or field variance can be created.

B.6 Field functions

An important step is ensuring that all data is collected for good post processing. This requires the right field functions. A list of possibly important quantities to monitor is provided.

1. The development of mean values over simulation time are very important. It is advised to create mean field monitors of axial velocity, pressure, and variances of the velocity components (axial, tangential and radial).
2. With the variances of the velocity components, the turbulent kinetic energy can be computed using Equation 2.6. A new field function can be created under **Tools > Field Functions > New > Scalar**. The definition of the TKE field function is: $0.5 * (\{FieldVarianceVelocityiMonitor\} + \{FieldVarianceVelocityjMonitor\} + \{FieldVarianceVelocitykMonitor\})$.
3. Tracking the development of the mean of velocity, pressure and TKE, the time to eliminate initial effects (1st and 2nd order effects) can be determined. From this point on the real sampling of mean and variance values can start. The next mean quantities are of interest: CFL number, pressure, SGS TKE (see next bullet point), skin friction coefficient, TLS, turbulent viscosity, turbulent viscosity ratio, axial velocity, radial velocity, tangential velocity, vorticity, wall shear stress, and wall Y+. Field variances of the next quantities are of interest: axial velocity, radial velocity, tangential velocity, pressure, and wall shear stress.
4. To enable the SGS Turbulent Kinetic Energy field function StevePortal (2019d), the Ffowcs Williams-Hawkings model has to be activated along with the subgrid scale model.

B.7 Other

1. Shorten the name of the reports and monitors created as these end up in the saved file.

B.7.1 How to determine average cell size in bulk region

1. Create a field function defined as in Equation 4.22, with definition: $1.2 * pow(\$Volume, 1/3)$.
2. Create a threshold derived part under **Derived Parts > New Part > Threshold**.
3. As only the cell size of the bulk region is of interest now, it is very important to create a mesh with prism layer cells being larger than the estimated bulk cell base size, so these cells can be excluded when determining the average cell size.
4. Select the region as part in the new derived part. Select the created field function as Scalar Field. Set the range from zero to a little less than the cell size of the prism layer. Only then the prism layer is excluded. To check and ensure, a scene can be created checking the grid size.
5. Run a volume average report for the created field function and new derived part.
6. The result gives a good estimate of the average cell size in the bulk region.

Appendix C

Reynolds-Averaged Navier-Stokes

A way to compute the motion of fluid is using the Reynolds-averaged Navier-Stokes (RANS) equations. The behavior of turbulent flows can be computed in a computational friendly way, averaging the fluctuating quantities of motion in time. RANS simulations give a reasonable insight in the mean behavior of the flow and provides proper input for the non-time-averaged computational methods as LES. RANS is computationally interesting because of removing all scales of motion ($\overline{u'_i} = 0$). In time-averaged form, the governing equations of motion of a stationary and incompressible Newtonian fluid are

$$\rho \bar{u}_j \frac{\partial \bar{u}_i}{\partial x_j} = \frac{\partial}{\partial x_j} \left[-\bar{p} \delta_{ij} + \mu \left(\frac{\partial \bar{u}_i}{\partial x_j} + \frac{\partial \bar{u}_j}{\partial x_i} \right) - \overline{\rho u'_i u'_j} \right] + \rho \bar{f}_i \quad (\text{C.1})$$

Equation C.1 consists of the same terms as in the momentum equations, see Equation 2.2, without time dependent terms and with an additional term $\overline{\rho u'_i u'_j}$. This additional term is called the Reynolds stresses arising from taking the mean from the nonlinear convective term. Time-averaging the conservation equation, Equation 2.1, together with the Reynolds-averaged momentum equations, provides four independent equations to solve the unknowns. Besides the pressure component and three velocity components, however, the additional Reynolds stresses are unknown quantities as well. Having more unknown than equations introduces the closure problem. A determination of the Reynolds stresses is required to close the problem and solve for the unknown quantities \bar{u}_i and \bar{p} .

C.1 Precursor steady-state simulation

A precursor steady-state simulation is intended to provide a good initial averaged solution to the transient simulation. A precursor simulation solution close to the actual converged unsteady solution shortens the time spent in the initial stage of the transient run adjusting the unsteady flow to its mean state. Additionally, running a precursor steady-state simulation on an exploratory mesh provides information for the required grid size and time step for the LES (Tucker (2016)).

C.2 Closure problem

By introducing turbulence models, the closure problem can be tackled. The turbulence model used to do so is the turbulent viscosity hypothesis. This hypothesis, proposed by Boussinesq, determines the Reynolds-stress by the mean velocity gradients. It is given as

$$\overline{u'_i u'_j} = \frac{2}{3} k \delta_{ij} - 2\nu_T \bar{S}_{ij} \quad (\text{C.2})$$

In here, ν_T is the turbulence eddy viscosity, S_{ij} is the mean rate-of-strain tensor

$$\bar{S}_{ij} = \frac{1}{2} \left(\frac{\partial \bar{u}_i}{\partial x_j} + \frac{\partial \bar{u}_j}{\partial x_i} \right) \quad (\text{C.3})$$

, and k is the turbulence kinetic energy defined as $k = \frac{1}{2} \overline{u'_i u'_i}$. The turbulent viscosity can be written as a product of a velocity U^* and length l^* . A widely technique to specify the turbulent viscosity in CFD models, is the k - ϵ model proposed by Launder and Spalding (1983). This two equation model uses a turbulent viscosity $\nu_T = \rho C_\mu k^2 / \epsilon$. In here ϵ is the turbulence dissipation, and C_μ is a flow dependent parameter. Note that in RANS the to be closed term is not a function of length scales and thus numerical grid, as in LES, but only on variables k and ϵ in case of using the k - ϵ method.

C.3 Turbulence models

Often applied turbulence models are the k - ϵ and k - ω model. Both are two equation models to solve the variables of the model to determine the turbulent eddy viscosity. Applying the former is best in the form of the Realizable k - ϵ form being better than the Standard k - ϵ for many applications (STAR-CCM+, 2018, p. 6990). This model is applied in combination with the Two-Layer together with the All y^+ Wall Treatment.

The k - ω model is beneficial over the k - ϵ model in regions with an adverse pressure gradient, existing in the orifice region. However, its disadvantage is its huge dependency on inlet conditions for internal flows (STAR-CCM+, 2018, p. 7019). The k - ω model is combined with the SST blending both the practicalities of k - ω and k - ϵ .

C.3.1 Exploratory meshes

Precursor RANS is performed on exploratory meshes. Flow is modelled using prism layers near the wall and polyhedral cells in the bulk region, see Section 4.4. Three meshes are proposed consisting of either ten, twenty, or thirty prism layers in combination with a cell base size of respectively 0.7mm, 0.4mm, and 0.2mm. The exploratory numerical grids are build up with respectively 207k, 1208k, and 7488k cells. Cross sections of the coarse (207399 cells), finer (1208931 cells) and finest mesh (7488721 cells) are depicted in Figure C.1.

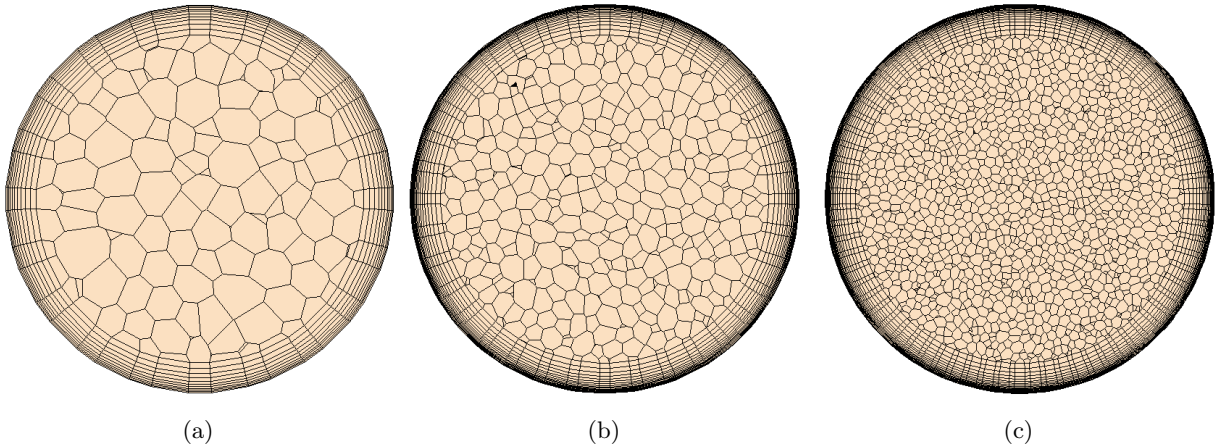


Figure C.1: Computational meshes used for getting the RANS results. a: Coarse mesh; 10 prism layer cells and a cell base size of 0.7 mm. b: Finer mesh; 20 prism layer cells and a cell base size of 0.4 mm. c: Finest mesh; 30 prism layer cells and a cell base size of 0.2 mm.

C.3.2 Boundary conditions

The turbulence intensity and turbulence length scale are used to specify turbulence for initialization and inlet turbulence creation for the RANS simulation. These should be in the right range in order to have reasonable answers far from the inlet. Russo and Basse (2016) provided a turbulence intensity scaling as

$$I \equiv \frac{u'}{U_b} = 0.140 Re^{-0.0790} \quad (\text{C.4})$$

The turbulent length scale is estimated as (STAR-CCM+, 2018, p. 3682):

$$l = 0.05D \quad (\text{C.5})$$

A plug velocity of $U = U_b = 1.06\text{m/s}$ is used based on the mass flow rate. After convergence, cross sectional data far from the inlet is captured and applied for inlet conditions. With that fully developed turbulence is obtained in the whole region. These fields are assumed suitable for initializing LES. It is important to note that a field function has to be created specifying the turbulence length scale, using e.g. the Realizable k - ϵ turbulence model, as:

$$l = C_\mu \frac{k^{\frac{3}{2}}}{\epsilon}. \quad (\text{C.6})$$

C.4 Precursor RANS results

Modeling turbulence using the k - ϵ and k - ω model, a fully developed velocity and TKE profile are simulated, as illustrated in Figure C.2, for all exploratory meshes. Comparing to DNS data, obviously both turbulence models give better solutions of turbulent profiles for finer meshes. In Figure C.2a namely, the viscous sublayer is more accurately simulated as well as velocity values starting at the log-law region ($y^+ > 30$). Also in Figure C.2b this also the case showing values closer to the well resolved solution. TKE peak values are located at the right location, showing significantly lower values, especially using the k - ω model. Note that because of understanding reasons, the TKE is intentionally plotted with normal x-scale. Subsequently, on the x-axis the distance from the wall is normalized with diameter because the distance to the wall y^+ shows large deviations for different Reynolds numbers when not on a log-scale. RANS simulations are known to show this behavior, indicating that resolving on an even finer grid is not required. For this particular case the k - ϵ model is found to give most accurate results.

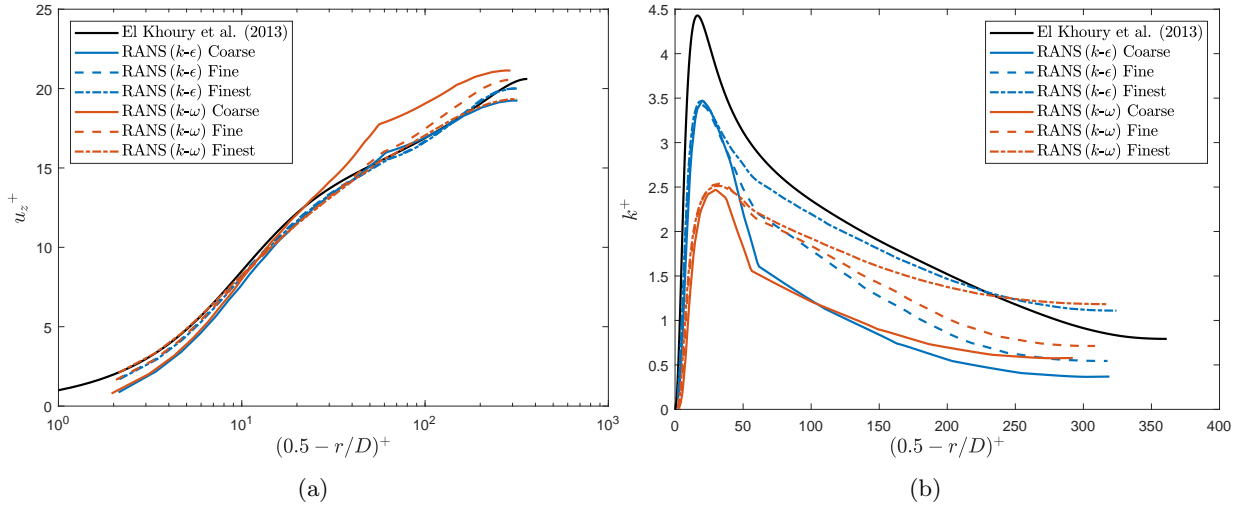


Figure C.2: Fully developed turbulent profiles obtained with RANS using the k - ϵ and k - ω model for two exploratory meshes. a: Normalized axial velocity component. b: Normalized TKE.

Important length scales obtained with the k - ϵ on the finest grid are illustrated in Figure C.3. These length scales are elaborated on in Section 2.3. For LES of orifice flow, two regions are of interest for scale resolving; the region upstream and downstream of the orifice. The with that associated Taylor-micro scales are found relatively independent on the RANS model and mesh used adopting values from 0.5mm to 0.8mm upstream of the orifice. Lower values of the scale at which energy dissipation starts are found in the jet region, indicating that smaller cell sizes are required to resolve scales in that region. For reasonable LES therefore the cell sizes should be in the nearby of 0.1mm in that region, see Figure C.3b.

The turbulent length scale, which is more sensitive to changes in the modeled turbulent kinetic energy and turbulent dissipation rate, is more mesh and model dependent, see Figure C.3. As in the very center of the pipe the TKE is not well modeled, the obtained TLS is likely to be off. This important scale is to be tested in LES.

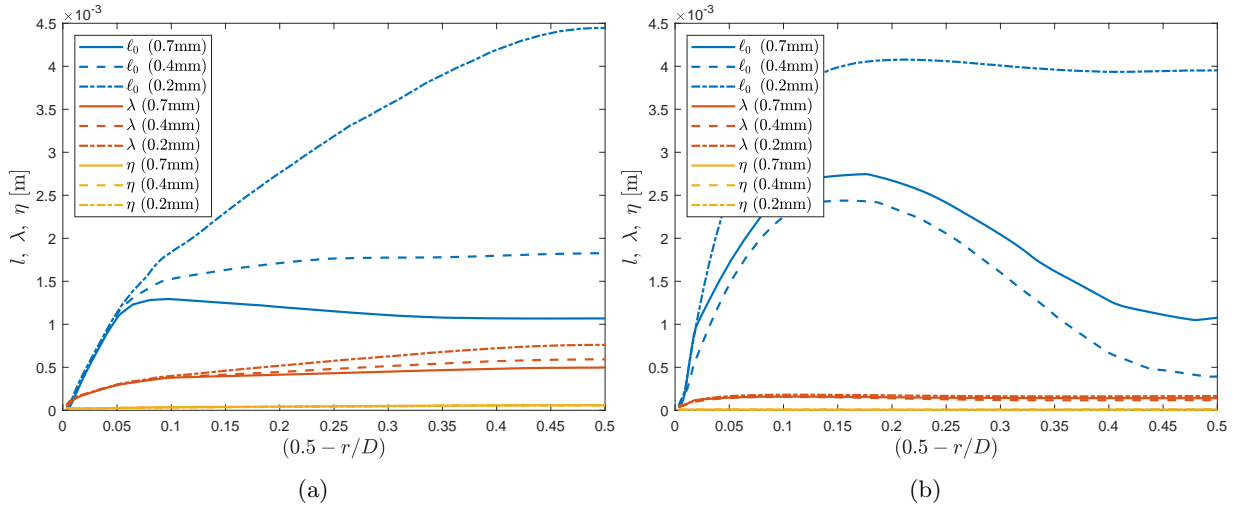


Figure C.3: Fully developed turbulent scales obtained with RANS using the $k-\epsilon$ and $k-\omega$ model for different meshes. a: TLS, TMS, and KLS at $z/D = -2$ (fully developed pipe flow) and $z/D = 2$ (recirculation zone) from orifice. b: Turbulent length scale at $z/D = -2$ (fully developed pipe flow) and $z/D = 2$ (recirculation zone) from orifice.

Besides resolving length scales, representing time scales is important. In LES the eddy-turnover time of large t is namely proportional to the time step chosen. If a time step larger than t is chosen, flow mixing of larger scales is limited. Therefore, the time step chosen imposes a limit to the development of smaller scales. Choosing a time step, the turbulent time scale can be considered in LES (STAR-CCM+, 2018, p. 2896). In the RANS simulation on the finest mesh the smallest turbulent time scale of the dissipative eddies, t_η , is found in the jet region being 5×10^{-6} s. For the turbulent time scale this is roughly 1×10^{-4} s.

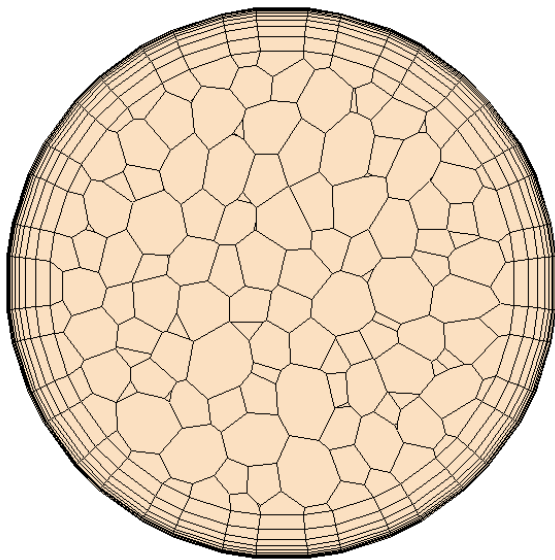
In simple pipe flow the pressure drop can be related to the average wall shear stress by

$$\Delta p A_p = \tau_w A_w \quad (\text{C.7})$$

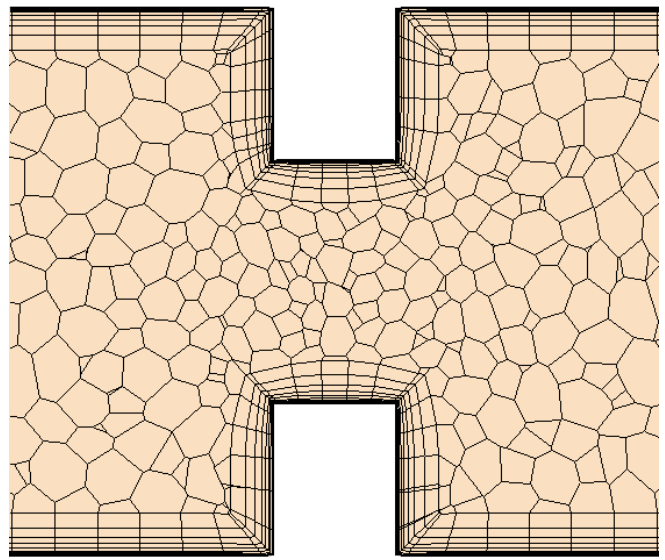
Wall shear stress values are typically around 4.44 Pa which is in accordance with the measurements of den Toonder and Nieuwstadt Den Toonder and Nieuwstadt (1997). A pressure drop of 0.209 bar is found for the $k-\epsilon$ on finest grid.

Appendix D

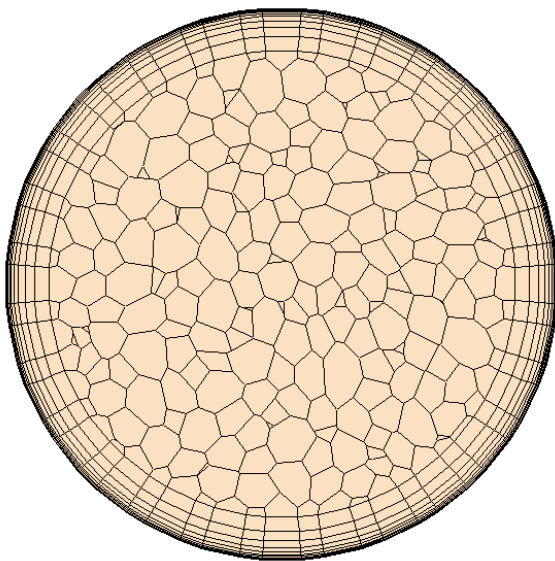
Computational Grids for LES



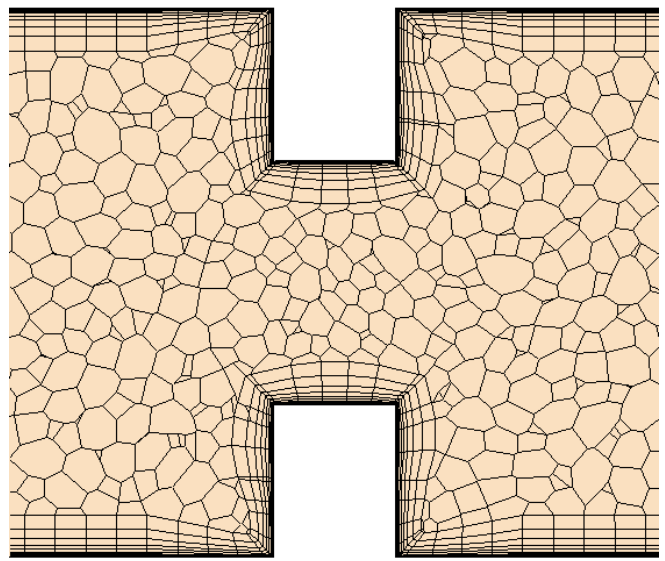
(a) Grid 1.



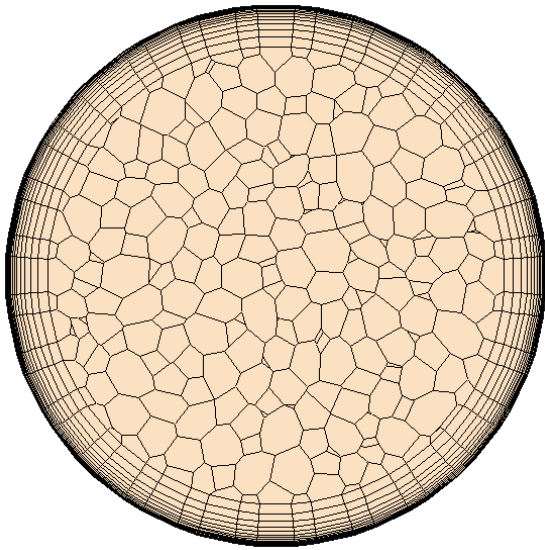
(b) Grid 1.



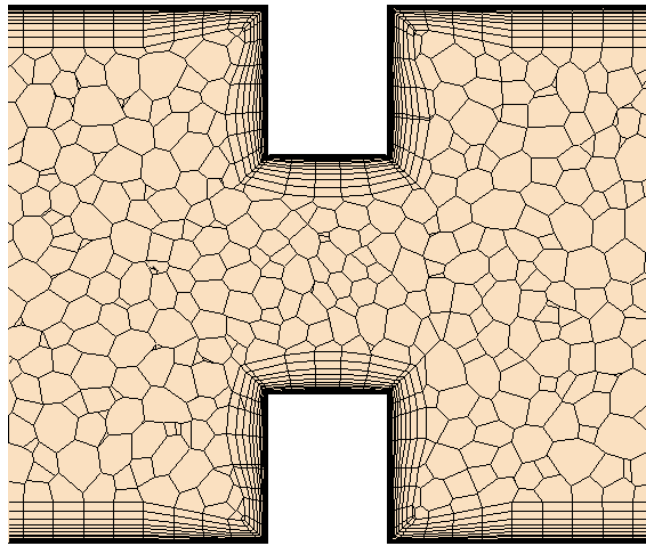
(c) Grid 2.



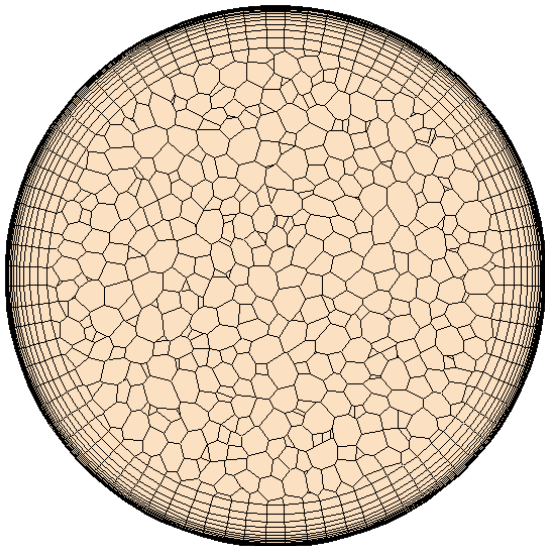
(d) Grid 2.



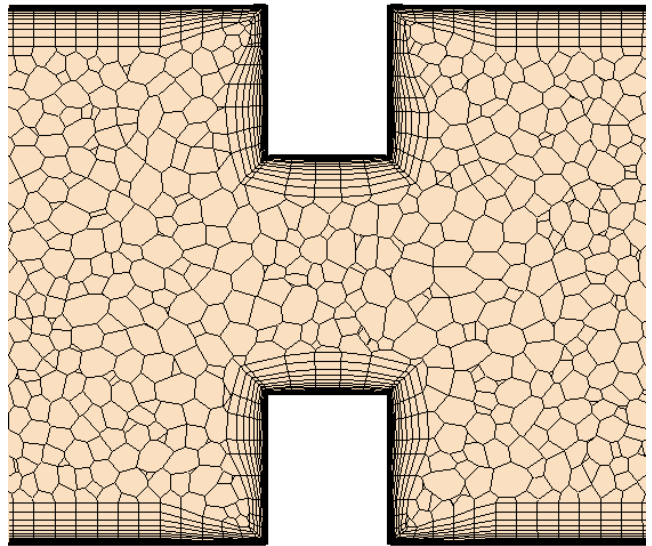
(e) Grid 3.



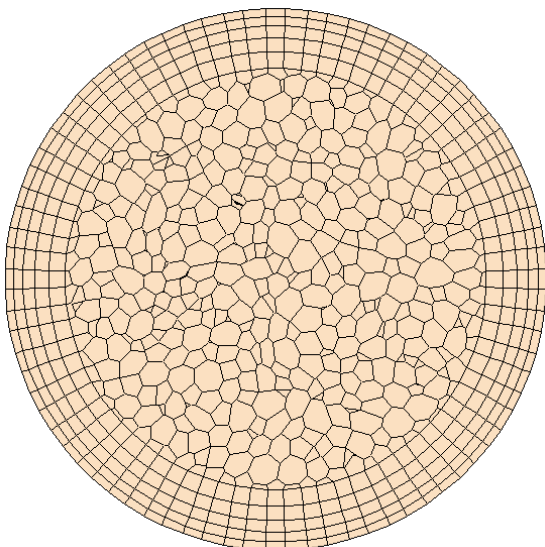
(f) Grid 3.



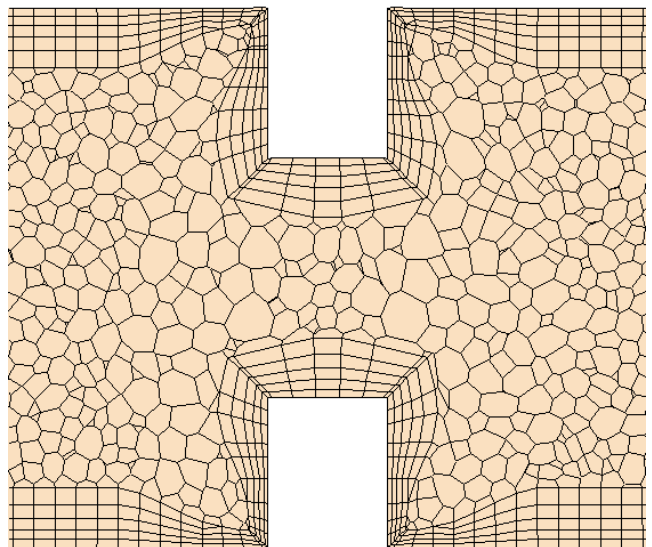
(g) Grid 4.



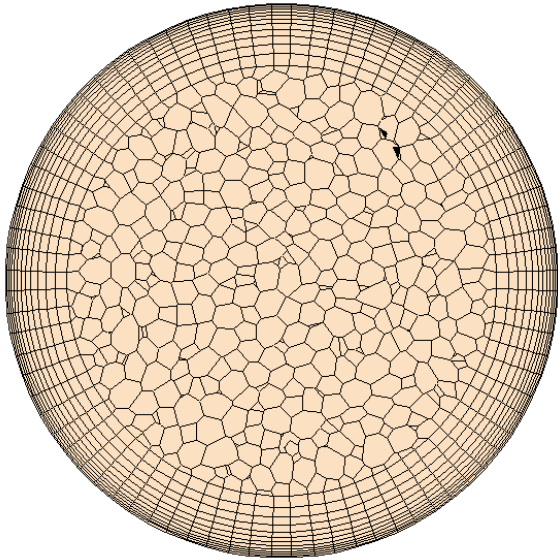
(h) Grid 4.



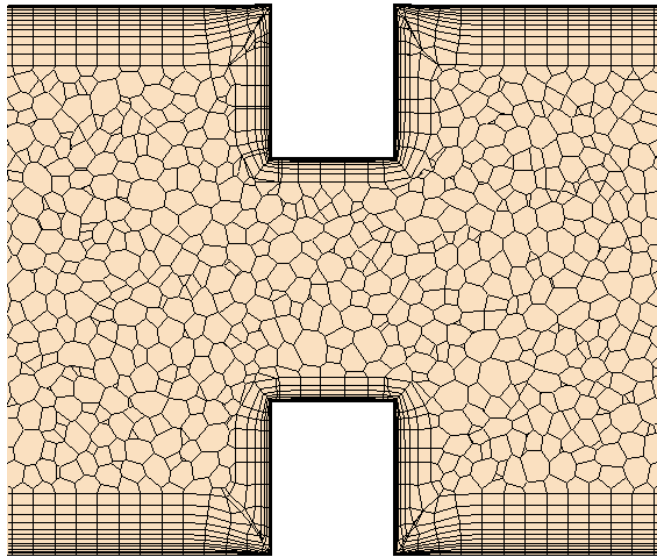
(i) Grid 5.



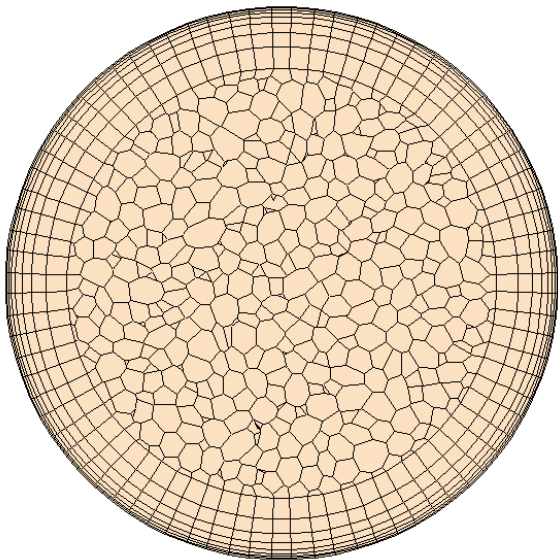
(j) Grid 5.



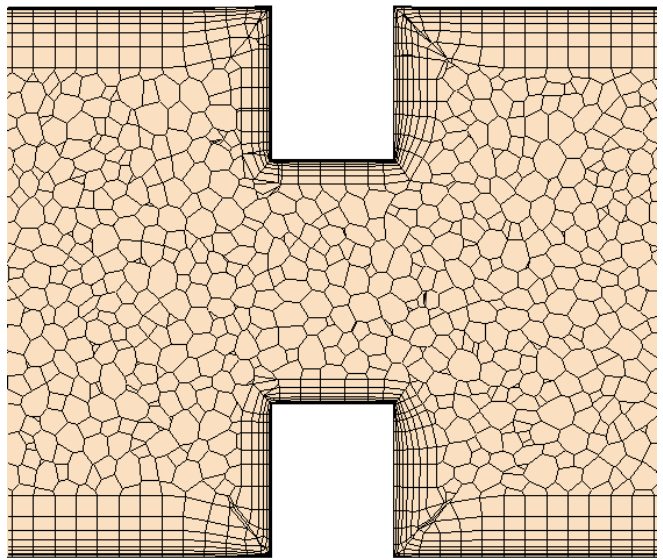
(k) Grid 6.



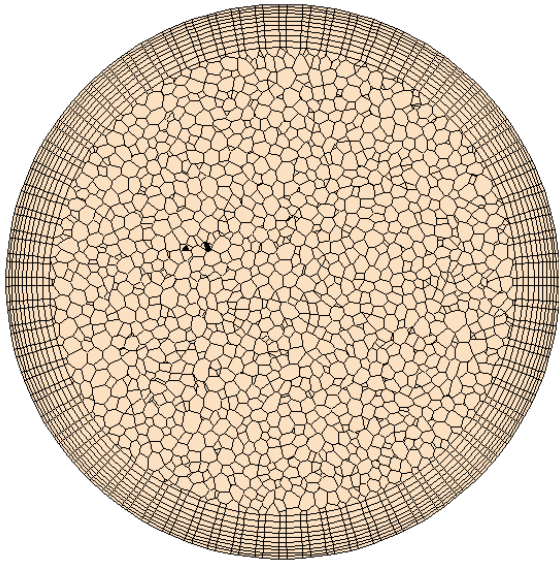
(l) Grid 6.



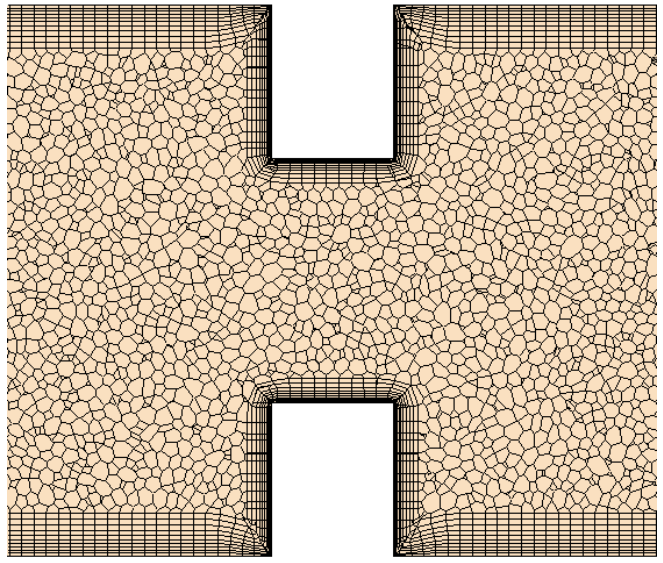
(m) Grid 7.



(n) Grid 7.



(o) Grid 8.



(p) Grid 8.

Figure D.1: Used computational meshes with settings tabulated in Table 4.1. a: Cross section of Grid 1 (cell base size is 0.7mm, 10 prism layer cells). b: Orifice region of Grid 1 (cell base size is 0.7mm, 10 prism layer cells). c: Cross section of Grid 2 (cell base size is 0.5mm, 12 prism layer cells). d: Orifice region of Grid 2 (cell base size is 0.5mm, 12 prism layer cells). e: Cross section of Grid 3 (cell base size is 0.5mm, 25 prism layer cells). f: Orifice region of Grid 3 (cell base size is 0.5mm, 25 prism layer cells). g: Cross section of Grid 4 (cell base size is 0.35mm, 25 prism layer cells). h: Orifice region of Grid 4 (cell base size is 0.35mm, 25 prism layer cells). i: Cross section of Grid 5 (cell base size is 0.35mm, 5 prism layer cells). j: Orifice region of Grid 5 (cell base size is 0.35mm, 5 prism layer cells). k: Cross section of Grid 6 (cell base size is 0.35mm, 12 prism layer cells). l: Orifice region of Grid 6 (cell base size is 0.35mm, 12 prism layer cells). m: Cross section of Grid 7 (cell base size is 0.35mm, 8 prism layer cells). n: Orifice region of Grid 7 (cell base size is 0.35mm, 8 prism layer cells). o: Cross section of Grid 8 (cell base size is 0.2mm, 10 prism layer cells). p: Orifice region of Grid 8 (cell base size is 0.2mm, 10 prism layer cells).

Appendix E

Results of Straight Pipe

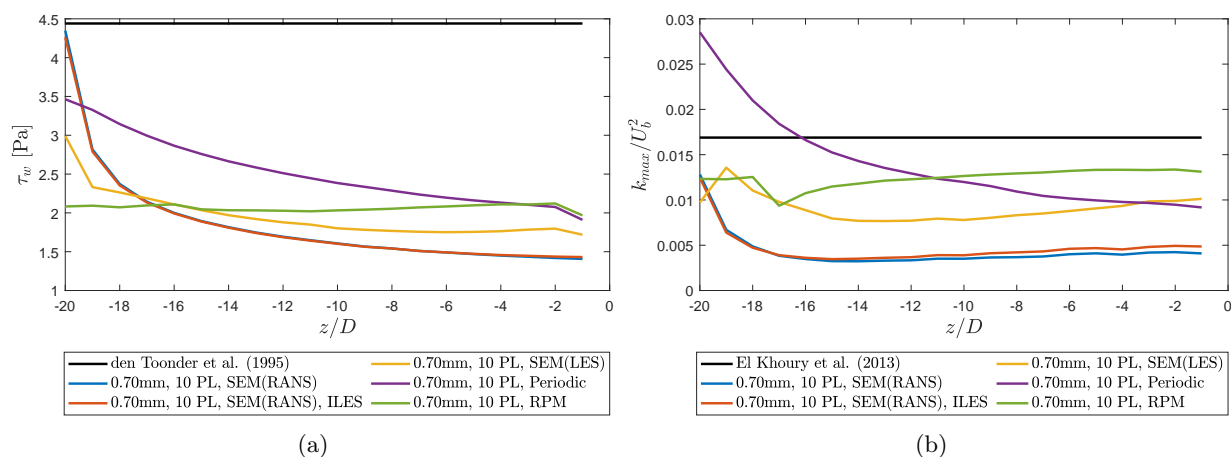


Figure E.1: The development of quantities as a function of the upstream distance to the inlet. a: The wall shear stress. b: The bulk TKE normalized with the bulk velocity squared.

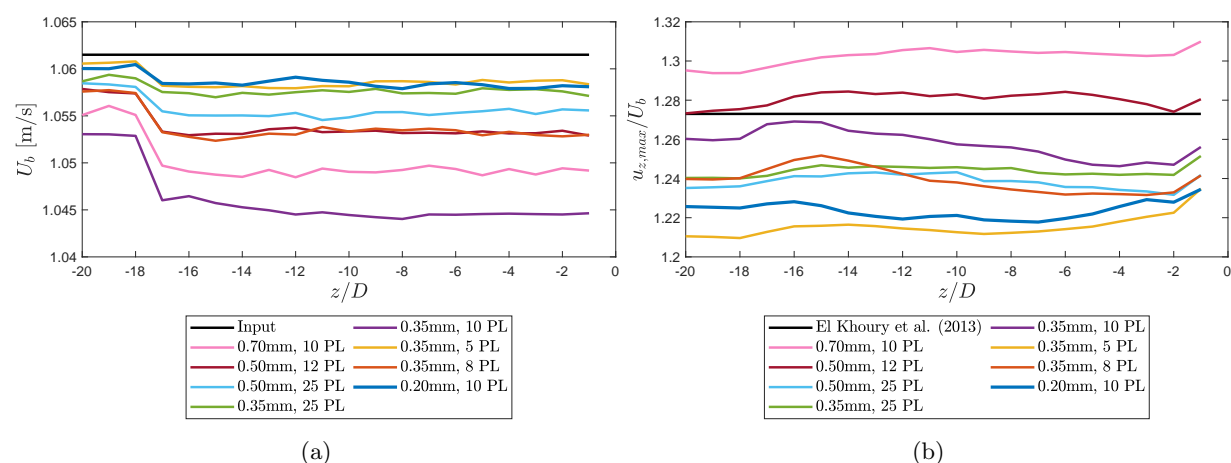


Figure E.2: Development of quantities as a function of the upstream distance to the inlet. a: Bulk velocity. b: Centerline axial velocity component normalized with the bulk velocity.

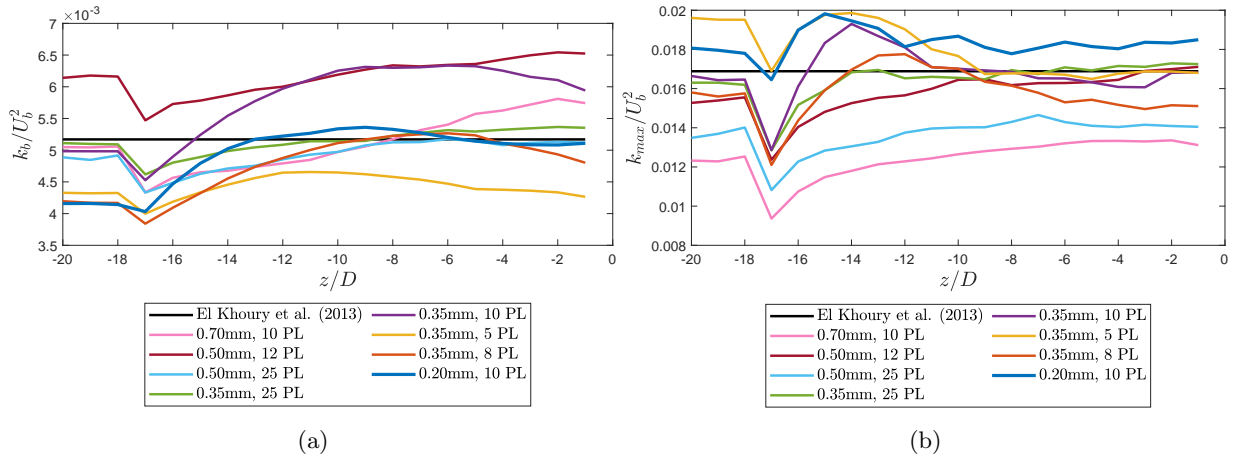


Figure E.3: Development of the TKE as a function of the upstream distance to the inlet. a: Bulk TKE normalized with the bulk velocity squared. b: Maximal TKE normalized with the bulk velocity squared.

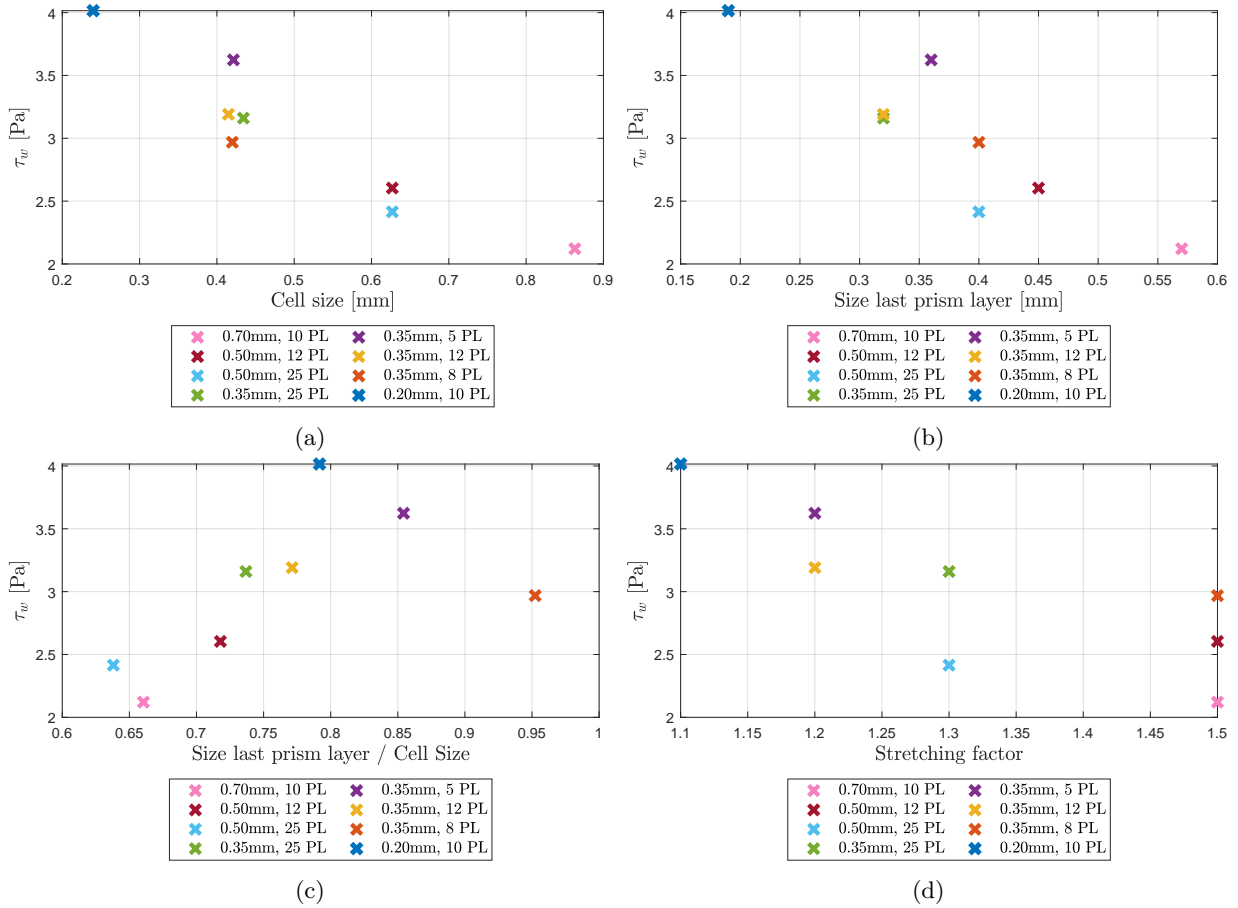


Figure E.4: Wall shear stress as a function of the computational grid properties. a: As a function of the cell size in bulk region. b: As a function of the cell size of last prism layer. c: As a function of fraction of the cell size of the layer prism layer and the cell size in bulk region. d: As a function of the stretching factor.